TECHNICKÁ UNIVERZITA V LIBERCI
Fakulta strojní

Energy Harvesting Using Cylindrical Piezoelectric Transducers

Dissertation Thesis

Study programme: P0715D270002 Machines and Equipment Design
Author: **Ing. Shehab Salem**
Thesis Supervisor: prof. Ing. Karel Fraňa, Ph.D.
Department of Power Engineering Equipment

Liberec 2022

Prohlášení

Prohlašuji, že svou disertační práci jsem vypracoval samostatně jako původní dílo s použitím uvedené literatury a na základě konzultací s vedoucím mé disertační práce a konzultantem.

Jsem si vědom toho, že na mou disertační práci se plně vztahuje zákon č. 121/2000 Sb., o právu autorském, zejména § 60 – školní dílo.

Beru na vědomí, že Technická univerzita v Liberci nezasahuje do mých autorských práv užitím mé disertační práce pro vnitřní potřebu Technické univerzity v Liberci.

Užiji-li disertační práci nebo poskytnu-li licenci k jejímu využití, jsem si vědom povinnosti informovat o této skutečnosti Technickou univerzitu v Liberci; v tomto případě má Technická univerzita v Liberci právo ode mne požadovat úhradu nákladů, které vynaložila na vytvoření díla, až do jejich skutečné výše.

Současně čestně prohlašuji, že text elektronické podoby práce vložený do IS/STAG se shoduje s textem tištěné podoby práce.

Beru na vědomí, že má disertační práce bude zveřejněna Technickou univerzitou v Liberci v souladu s § 47b zákona č. 111/1998 Sb., o vysokých školách a o změně a doplnění dalších zákonů (zákon o vysokých školách), ve znění pozdějších předpisů.

Jsem si vědom následků, které podle zákona o vysokých školách mohou vyplývat z porušení tohoto prohlášení.

August 15, 2022 Ing. Shehab Salem

ACKNOWLEDGMENT

I would like to thank my supervisor, prof. Ing. Karel Fraňa, Ph.D., for his continuous support during the research. Also, i would like to thank Brandenburgische Technische Universität Cottbus-Senftenberg for giving me access to its wind tunnel. Finally, i would like to thank without naming everybody who has guided me throughout my life course.

Annotation

The research in this dissertation addresses the use of cylindrical piezoelectric transducers to harvest acoustic energy as well as flow-induced vibrations. Four cylindrical transducers made from Lead Zirconate Titanate and of different dimensions were used in the study. The research has addressed acoustic energy harvesting using open-circuit measurements performed on cylinders of two different sizes in order to find a relation between the cylinder size and the cylinder interaction with acoustic waves. After open-circuit measurements, a series of closed-circuit experiments were performed in order to optimise the load circuit for harvesting sound waves of frequency 20 kHz.

The research has also addressed the harvesting of flow-induced vibrations inside a wind tunnel. Open-circuit measurements were performed on the four piezoelectric cylinder sizes in order to compare their response to the known features of flow instabilities. Finally, closed-circuit measurements were performed to measure the amount of harvested power at different wind speeds and different loads to study the effect of the windspeed and the circuit impedance on the process.

Keywords: Piezoelectric / Energy Harvesting / Flow-Induced Vibration / Vortex-shedding / Acoustic Energy Harvesting / PZT

Výzkum v této disertační práci se zabývá využitím válcových piezoelektrických měničů ke sběru akustické energie a také prouděním indukovaných vibrací. Ve studii byly použity čtyři válcové měniče vyrobené z olovnatého zirkoničitanu titanátu a různých rozměrů. Výzkum se zabýval sběrem akustické energie pomocí měření na otevřeném okruhu prováděných na válcích dvou různých velikostí za účelem nalezení vztahu mezi velikostí válce a interakcí válce s akustickými vlnami. Po měření naprázdno byla provedena řada experimentů s uzavřeným okruhem za účelem optimalizace zatěžovacího obvodu pro sběr zvukových vln o frekvenci 20 kHz.

Výzkum se také zabýval sběrem vibrací vyvolaných prouděním uvnitř aerodynamického tunelu. Měření naprázdno byla provedena na piezoelektrických válcích čtyř různých velikostí, aby bylo možné porovnat jejich odezvu se známými vlastnostmi nestability proudění. Nakonec byla provedena měření v uzavřeném okruhu, aby se změřilo množství získané energie při různých rychlostech větru a různém zatížení, aby se studoval vliv rychlosti větru a impedance okruhu na proces.

Klíčová slova: Piezoelektrika / Získávání energie/ Vibrace indukované průtokem / vytváření vírů / Získávání akustické energie / PZT

Table of Contents

List of the Used Abbreviations and Symbols

List of the Used Abbreviations:

AEH	Acoustic Energy Harvesting
AET	Acoustic Energy Transfer
EIMN	Electric Impedance-Matching Network
FFT	Fast Fourier Transform
FIV	Flow-Induced Vibrations
LDV	Laser Doppler Velocimetry
MEMS	Micro-Electro-Mechanical Systems
PEH	Piezoelectric Energy Harvester
PFEH	Piezoelectric Flow Energy Harvesters
PIV	Particle Image Velocimetry
PVIVH	Vortex-Induced Vibration Harvesters,
PZT	Lead Zirconate Titanate
RF	Radio Frequency
SPL	Sound Pressure Level
VIV	Vortex-Induced Vibration

List of the Used Symbols

A_{cyl}	Cylinder surface area
a	Speed of sound in air
C	Electric capacitance
D	Electrical displacement

D_{cyl}	Cylinder diameter
d_{ij}	Direct piezoelectric charge constant matrix
d^t	Converse piezoelectric charge constant matrix
E	Applied electric field
E_k	Turbulence spectral energy for a wave number k
E_p	Modulus of elasticity of the material
F_{r_p}	Resonance frequency in the radial direction
F_{r_t}	Resonance frequency in the thickness direction
f	Signal frequency
f^o	Dimensionless frequency referenced to object size
f_s	Frequency of vortex shedding in the flow
g_{ij}	Piezoelectric Voltage Constant matrix
I	Sound intensity
I_{ref}	Sound intensity threshold of hearing by humans
k	Turbulence spectral energy wave number
K_{oc}	Open-circuit stiffness
K_{Sc}	Closed-circuit stiffness
L	Inductance
L_{cyl}	Cylinder length
L_W	Sound Power level
L_i	Sound Intensity level
L_V	Sound velocity level

Metric	A metric to evaluate energy harvesters
N_P	Radial mode frequency constant
N_t	Thickness mode frequency constant
P	Electric power
$P_{acoustic}$	Acoustic power
Q_m	Mechanical quality factor
Q_{mean}	Mean of the total generated electric charge.
q	Specific charge generated per unit surface area of the cylinder
Re	Reynolds Number
R	Resistance
S_{ij}	Elastic compliance constant matrix
S^E	Mechanical compliance tensor at a constant electric field.
s	Mechanical strain
St	Strouhal number
T	Applied mechanical stress
t	Cylinder thickness
U	Mainstream airspeed in the wind tunnel.
V	Voltage
V_f	Diode forward voltage
V_{loss}	The measured voltage drop across the full-wave rectifier bridge
V_m	The mean of voltage signal due to vortex-induced vibrations.
Vol	harvester volume

X	Reactive impedance
Z	Electric impedance magnitude
$Z_{acoustic}$	Acoustic impedance
Z_c	Electric impedance of a capacitor
Z_L	Electric impedance of an inductor
Z_t	Electric impedance in complex notation

The Greek Symbols

α	Proportionality constant in kolomogorov's model for turbulence
β	Proposed proportionality constant between voltage generated from vortex-induced vibrations and its frequency
ε	Electrical permittivity
ε_k	Turbulence energy dissipation rate
ε^T	the relative permittivity at a constant mechanical stress
ζ	Dielectric Coefficient
η	Efficiency of energy harvesting
η_v	Voltage rectification efficiency
κ	Piezoelectric coupling coefficient
λ	Sound wavelength
v	Kinematic viscosity of air
Π	Sound pressure
ρ	Energy harvesting density
Φ	Phase difference

List of Figures

The Goal of the Research

The goal of this thesis is to perform a feasibility study for energy harvesting using cylindrical piezoelectric transducers in order to enhance energy effectiveness in Micro-Electro-Mechanical-Systems. The thesis shall consider two types of energy harvesting: Harvesting of acoustic energy and Harvesting of Flow-Induced Vibrations. Hence, the thesis is divided into two parts whose goals are as follows:

Acoustic Energy Harvesting:

- To construct an energy harvester that uses the proposed transducers.
- To optimize the harvester for acoustic energy harvesting.
- To evaluate the performance of the proposed harvester.

Flow-Induced Vibrations Harvesting:

- To study the output of the piezoelectric cylinders and compare it to the pressure characteristics of the flow.
- To find a relation between the quality of energy harvesting and Reynolds number of the flow.
- To construct a vibrational energy harvester that uses the proposed transducers.

1 Introduction

1.1 Energy Harvesting:

Since the beginning of time, securing energy sources has been a vital prerequisite to establishing a working community. At first, man relied on manual power—either from labour or domestic animals—to perform physical tasks. Along with the manual power, the use of the forces of nature was involved as much as the technology of that time allowed. Perhaps the earliest example is the drawings of simple wind-powered sailboats found in ancient Egypt dating back as old as 3000 B.C. [1]. Windmills are believed to be first depicted by Heron the Greek around 200 B.C. in his book *Pneumatica*, though there are other sources that date its use in irrigation back to 1700 B.C. in Mesopotamia, Iraq [2]. In addition to windmills, watermills have been developed to exploit the energy of flowing rivers. The Romans have used watermills since as early as the first century B.C. to cut wood and stone as well as to produce flour [3].

During the middle ages, mankind relied mainly on muscles, wind, and water energy to provide kinetic energy. For thermal energy, the burning of coal and wood—where they were available—was the main source of heat energy. The lean toward renewable sources of kinetic energy, wind, and water, lasted till the industrial revolution and the invention of the steam engine. At that point in time, fossil fuel started to become a source of both thermal and kinetic energy. Since then, mankind has leaned more and more toward fossil fuels on account of, what was still primitive back then, renewable energy technologies. Moreover, the discovery of electricity in the nineteenth century has also encouraged the dependency on fossil fuel since it could be used to drive electric generators to generate electricity on a large scale that the rudimentary renewable energy sources could not meet at that time.

With the advantage—mainly the large-scale energy production—it can provide, fossil fuels started to accumulate several problems during the twentieth century. On one level, the scarcity of fossil fuels has started to be foreseen in the near future. Moreover, more and more evidence was collected that they cause the green-house gas effect on the planet, which results in climate change—Nowadays, historical records of high temperatures are being recorded all over Europe because of the ongoing climate change—Due to these reasons, renewable energies have started to become an unavoidable choice. In recent years, a huge body of work has been carried out to develop technologies for exploiting the various sources of renewable energies in nature. Therefore, several energy harvesting techniques have been developed, including photovoltaic panels, solar collectors, modern wind turbines, hydroelectric generators, and geothermal energy harvesters.

The aforementioned renewable energies are characterized by their large-scale energy generation, not as large as fossil fuel, though. However, they are limited by two main

disadvantages. The first disadvantage is their intermittency over the day/time. Such a disadvantage necessitates the availability of a reliable energy storage system. The second disadvantage is their limited availability, where the sources of these energy types are not available everywhere. Moreover, the only way to transport their energy is by transporting the generated electric energy rather than the source itself, contrary to fossil fuels.

Apart from large-scale energy harvesting, other energy harvesting technologies have been developed at the micro-scale energy level. These technologies rely on harvesting the energy already available in the surrounding of the end target and employing it to generate electric energy, rather than this energy being wasted. These technologies have mainly focused on harvesting the energy of mechanical vibrations. Apart from mechanical vibrations, Radio Frequency—RF—energy harvesting was developed to harvest the energy of the excess electromagnetic waves using an antenna connected to suitable power circuits [4]. Since vibrational energy harvesting is the scope of this thesis, it shall be discussed in more detail.

Vibrations exist abundantly in the environment. It is either naturally induced, e.g. earthquakes in the ground and the wave motion of oceans and seas, or induced by the operation of almost every mechanical machine. Its abundance makes it a great alternative as an energy source as it most probably surrounds any end target that might require energy, compared to other renewable energy sources discussed above. Therefore, vibration energy harvesting is extensively integrated into the Micro-Electro-Mechanical Systems, MEMS, as it helps make the MEMS energy-independent. Energy independency is quite important in the operation of certain MEMS as they may be intended to operate in inaccessible places, making the process of battery replacement impractical [5].

However, securing energy needs from mechanical vibration is quite challenging due to the complicated nature of this specific energy type compared to other types like solar or wind energy. The design of the vibration energy harvester must meet several criteria, as will be discussed later in Section 1.3.6 in more detail, regarding the frequency-response of the energy transducer, the frequency characteristics of the vibration itself, optimization of the power electronics for energy storage let alone the low energy content available in vibrations, compared to other traditional energy sources.

Various technologies have been developed to harvest the energy of vibrations. These technologies rely on various transduction technologies[1] such as Electrostatic, Electromagnetic, and Piezoelectric transduction [6] and [7]. However, the authors in [6] have compared different transduction technologies based on energy density—as energy converted per unit volume of the transducer—showing that piezoelectric transduction is

[1] As will be explained later, the transduction stage is the heart of energy conversion process, where vibrational energy is converted into useful electric energy

the technology with the highest efficiency and the smallest size. Such facts make piezoelectric materials a favourable option during the process of designing energy harvesters, where they have been used in several applications for energy harvesting. Since the piezoelectric materials belong to the material group Smart Materials, Smart Materials shall be discussed in the next section in detail.

1.2 Smart Materials

Smart Materials are materials whose one or more of their properties can be significantly changed in a controlled manner in response to external physical stimuli. These stimuli may be of various forms, e.g. mechanical stress, temperature gradient, electric, or magnetic fields [8]. Smart materials can hence be grouped according to the type of stimulus it responds to, together with the physical property that would respond to the applied stimulus. Examples of these groups include and are not limited to Piezoelectric Materials, Pyroelectric Materials, Electrostrictive Materials, and Magnetostrictive Materials. Moreover, Smart Materials also include other well-known groups of materials, e.g. Photovoltaic, Chromic Materials, and Phase-Change Materials. According to the mechanism of the material response to the acting stimulus, Smart Materials have been classified by Addington et al. [9] into two classes: Property Change and Energy Exchange materials.

Property Change materials are the materials that absorb the energy of the incident stimulus and use it to change their properties. Hence, the mechanism of the material response involves a change in the internal energy of the molecules altering either the molecular or the microstructure of the material. This change is later manifested in a change in one of the properties of the material. This class, Property Change Materials, includes all the colour-changing materials such as Thermochromic Materials[2], Electrochromic Materials[3], and Photochromic Materials[4]. Moreover, it includes stiffness-change materials such as Magnetorheological and Electrorheological materials [9]. As the names imply, these are materials that can develop a change in their rheological properties, i.e. viscosity and stiffness, in response to magnetic and electric fields, respectively.

On the other hand, the class of Energy Exchange Materials includes the materials whose response mechanism involves a change in the energy state of the material without altering its molecular structure. During this process, the material absorbs the input energy and changes it into a different form, according to the first law of Thermodynamics, without the material itself being changed. The most common material groups in this class are

[2] Materials that alter their colour in response to a change in its temperature [10].
[3] Materials that demonstrate a change in their colour as well as optical properties, e.g., absorbance, transmittance, and reflectance in response to the application of a voltage [11].
[4] Materials that can change between two isomeric states resulting in a colour change in response to absorption of electromagnetic radiation [12].

Photovoltaic Materials, Piezoelectric Materials, Pyroelectric Materials, Thermoelectric Materials, Electrorestrictive Materials, and Magnetorestrictive Materials [9]. Table 1-I summarizes these groups together with their acting stimuli and resulting effects. The work discussed in this thesis is based on piezoelectric materials. Therefore, the following section discusses the piezoelectric phenomenon in more detail.

Table 1-I Different groups of Energy Exchange smart materials and their interaction pairs.

Material Group	Stimulus-Effect
Photovoltaic	Electromagnetic Radiation – Electric Potential
Piezoelectric	Mechanical pressure – Electric field
Pyroelectric	Temperature gradient across time – Electric potential
Thermoelectric	Temperature gradient across space – Electric potential
Electrorestrictive	Electric field – Mechanical deformation
Magentorestrictive	Magnetic field – Mechanical deformation

1.3 Piezoelectricity

1.3.1 The piezoelectric phenomenon:

Piezoelectric Materials are materials that have the ability to develop electric charge on their surface in response to applied mechanical pressure [13], [14]. The name “Piezoelectric” is, in fact, derived from the Greek language, where the word “Piezein” means to squeeze [15]. Hence, Piezoelectricity is the electricity generated due to the application of pressure. The field of Piezoelectricity was constructed in 1880 A.D. by the brothers Curie during their experiments on the pyroelectricity of natural crystalline materials such as Rochelle Salt, topaz, quartz, and cane sugar [16]. They were the first to observe that mechanical stresses are also accompanied by a macroscopic polarization, and hence the production of electric surface charges [17].

In addition to naturally-existing materials, piezoelectricity can be found in synthesized materials as well. Synthesized piezoelectric materials can be categorized into three main

classes: ceramics[5], polymers, and composites, as shown in Figure 1.1 [19]. Piezoelectric ceramics, such as Barium Titanate, $BaTiO_3$, and lead Zirconium Titanate, PZT, are generally characterized by their high-quality piezoelectric parameters [20]. On the other hand, polymeric piezoelectric materials are carbon-based materials with long polymer chains. Such a structure gives them extreme flexibility, which allows for high strain levels. However, such an advantage comes at the expense of a piezoelectric quality less than that of ceramic materials. The most common piezoelectric polymer is Polyvinylidene fluoride, PVDF [21].

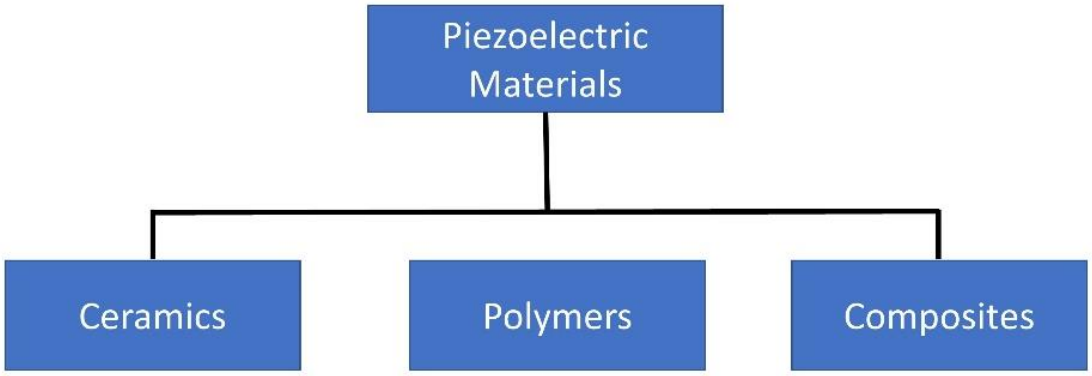

Figure 1.1 Classes of piezoelectric materials

Finally, composite piezoelectric materials are materials that have been engineered to combine the advantages of the prior classes together in one new class. This is achieved by developing a multi-phase composite between a ceramic-material phase matrix and a polymer-phase filler. The ceramic phase shall provide the high-quality piezoelectric properties, while the polymer phase shall lower the density and electric permittivity as well as increase the elastic compliance of the overall composite [22]. Since the piezoelectric material used in this research belongs to the Ceramics class, the piezoelectric ceramics shall be discussed in the next section in more detail.

[5] The most simple definition of Ceramics is that given by Kingery et al. in 1976 as the solids that are neither metallic nor organic. They tend, mostly, to be hard and brittle [18].

A piezoelectric ceramic is a mass of perovskite-structured[6] crystals. Each crystal is composed of a small tetravalent metal ion placed inside a lattice of larger divalent metal ions and Oxygen. However, these ions are packed in such a way that each crystal has tetragonal symmetry. The symmetry in each crystal generates an electric dipole moment. A group of adjacent dipoles forms together a region of local alignment known as ***domain*** [24].

Normally, the di-poles of different domains are randomly aligned, as shown in Figure 1.2a, however; during the manufacturing of a piezoelectric material, the material is subjected to a strong DC field that would cause the alignment of these domains together in a direction parallel to the electric field polarization direction. Therefore, the aligned dipoles collectively generate a net dipole of the whole piece of the material, as shown in Figure 1.2b, in a process called ***Polarization***. When the electric field is removed, most of the dipoles are locked into a configuration of near alignment leaving the material in a state of permanent polarization, as shown in Figure 1.2c. Only by heating the material to a temperature above the Curie temperature is the crystallization lost, and hence, the collective polarization of the dipoles. In other words, the material becomes non-piezoelectric. Therefore, Curie temperature can be defined as the maximum temperature limit below which a certain piezoelectric material can operate. Being a property of the material structure, it has to be defined as a property of each specific material.

When a polarized piezoelectric material is mechanically stressed, the dipoles are displaced, forming a net voltage to form. If the stress was in the form of compression along the direction of polarization or tension perpendicular to the polarization direction, a net voltage would be generated with the same polarization direction of the material. When the direction of the stress is reversed, voltage opposite to the polarization direction is formed.

[6] A structure named after that of the Perovskite material, $CaTiO_3$. The structure is common for materials of a general chemical formula as ABX_3, where A and B are cations with A larger than B and X is the anion usually oxides or halogens [23].

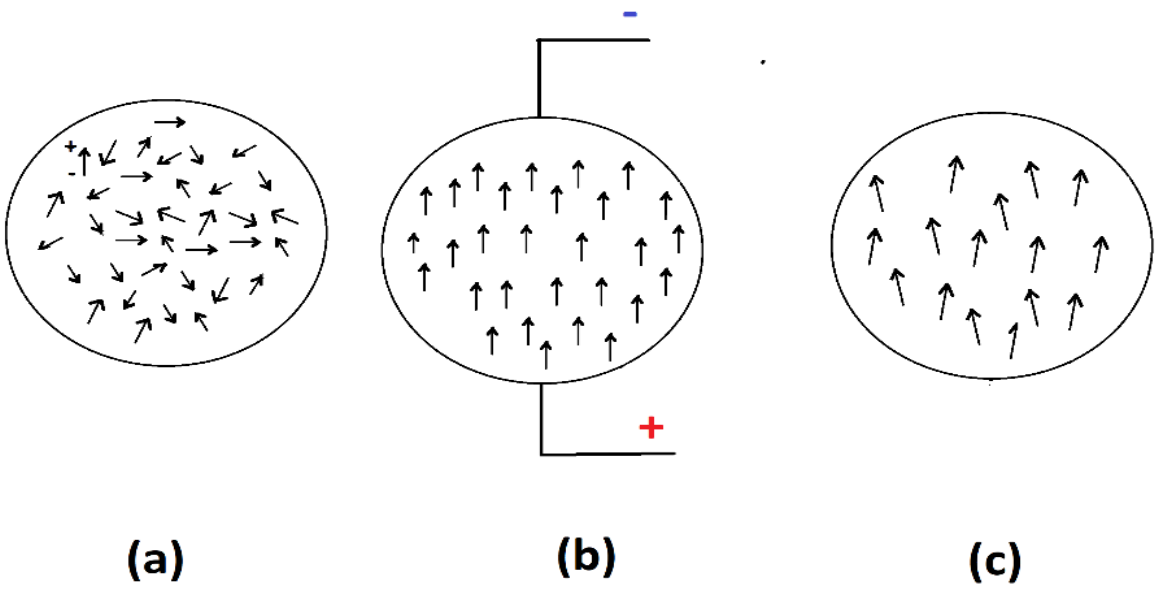

Figure 1.2 Dipoles in a piezoelectric material

1.3.2 Reversibility of piezoelectric transduction:

The piezoelectric transduction is reversible. This means that a piezoelectric transducer can operate according to the "*Direct Piezo effect*" or the "*Converse Piezo effect*". In the Direct Piezo effect, the transducer shall generate electric charges in response to applied mechanical pressure. This mode is mainly used in applications concerning sensing of pressure and accelerometers, as the material produces an electric signal that corresponds to the applied mechanical pressure. Moreover, this mode is used when piezoelectric materials are used as voltage generators [25].

On the other hand, in the Converse Piezo effect, the transducer shall generate mechanical pressure, i.e. mechanical strain, in response to applied electric charges, i.e. applied electric field. This mode is mainly used in applications concerning actuation, where the transducer is used to generate motion that corresponds to a specific electric signal. Moreover, piezoelectric materials adjusted to resonance conditions can be employed in applications concerning high-energy ultrasonic generators as well as Radio Engineering applications such as wave filters [25]. Moreover, it is used to manufacture the vibrating devices used in gaming consoles.

Moreover, the Converse Piezo effect has been much used in the speakers' industry. It was used to develop speaker-less speakers. This technology would be able to make one capable of hearing a recorded sound of their own exactly the same way they perceive it inside their head. Also, it has been used to develop miniature speakers that can produce sound loud enough to be heard during outdoor activities, yet the speakers would still have a small volume that may allow it to be built-in in smartphones, contrary to normal speakers that

rely on magnetic fields [26]. In addition to speakers, the Converse Piezoelectric effect has also been used to develop piezoelectric fans that can be used as both an energy- and space-efficient cooling solution. Thanks to its small space and energy requirements compared to rotary fans, it has a promising future in the field of cooling of electronic circuits [27]. Figure 1.3 summarizes the applications of the two modes.

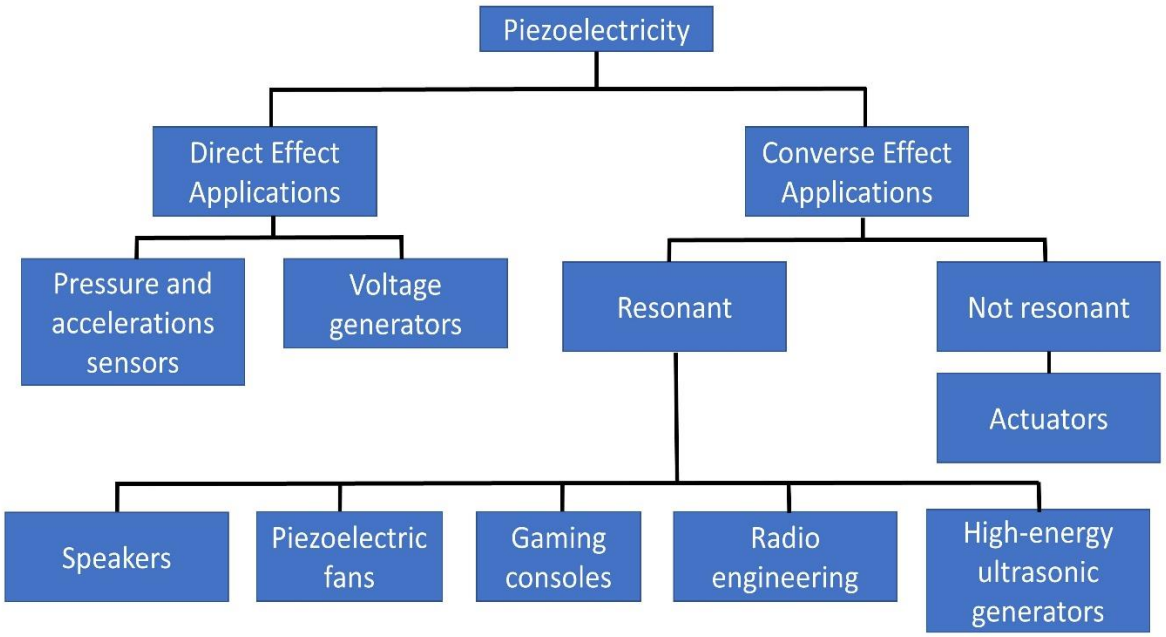

Figure 1.3 Applications of piezoelectricity.

There are many applications that rely on both the direct and Converse Piezo effects together. An example of these applications is the field of Structure Health Monitoring, SHM, where piezoelectric materials are used to remotely detect and predict a mechanical failure. This can be achieved by monitoring how the mechanical impedance of the piezoelectric sensor changes in response to the change in mechanical impedance of the structure [28]. Another example of applications where both of the two effects are used is the Acoustic Energy Transfer, AET, where piezoelectric materials can be used as an actuator to generate acoustic waves that would travel through a solid structure. The acoustic waves would then be received by another piezoelectric material that is operating as a sensor and hereby generates electric energy. Using this technology, it would be possible to power devices that are located in non-accessible locations. An example of these devices is the biomedical devices that are planted under live tissues [29].

Back to the Direct piezoelectric effect, the Direct effect is used, together with its other applications, in energy harvesting, which is the topic of this thesis. Thanks to the ability of piezoelectric materials to induce electric charges as a result of mechanical pressure, it has

a promising future to be used to harvest the energy of ambient vibrations that are exist in numerous life applications.

1.3.3 The piezoelectric parameters

1.3.3.1 Piezoelectric charge constant d_{ij} :

The piezoelectric charge constant was set to relate between the electrical displacement[7], *D*, and the applied mechanical stress, *T*, as shown by the left side of equation (1.1), for a Direct Piezo effect. In the case of the converse effect, it would relate the developed mechanical strain, *s*, to the applied electric field, *E*, as shown by the right side of the same equation. In the first case, its unit is C/N, while in the latter case, the unit m/V would be more convenient to use. The subscripts E and T refer to values measured at a constant electric field and mechanical stress, respectively [30, 31].

$$d_{ij} = \left(\frac{\partial D_i}{\partial T_j}\right)_E = \left(\frac{\partial s_j}{\partial E_i}\right)_T \tag{1.1}$$

1.3.3.2 Piezoelectric voltage constant g_{ij} :

The piezoelectric voltage constant relates the electric field developed along the i-axis to the stress when the material is stressed along the j-axis in the case of a Direct Piezo effect as described by the left side of equation (1.2). Also, it can relate between the developed mechanical strain and the applied electric charge displacement in the case of a Converse Piezo effect as described by the right side of equation (1.2). The subscripts in equation (1.2) follow the same notation scheme defined for equation (1.1) [30, 31].

$$g_{ij} = -\left(\frac{\partial E_i}{\partial T_j}\right)_E = \left(\frac{\partial s_j}{\partial D_i}\right)_T \tag{1.2}$$

1.3.3.3 Piezoelectric coupling coefficient κ_{ij} :

The piezoelectric coupling coefficient, also known as the Electromechanical Coupling Coefficient, indicates the ratio of the generated electric energy to the input mechanical energy in the Direct piezoelectric effect. Also, it indicates to the ratio of the accumulated mechanical energy to an input electric energy [31]. It is defined to be the square root of the ratio of electrical energy to mechanical energy, as shown in equation (1.3) [32]. It also can be expressed as a function of other piezoelectric constants, as shown in equation (1.4), where E_p is the modulus of elasticity of the material.

[7] Charge displaced per unit area of a conductor due to the action of an electric field.

$$\kappa_{ij} = \sqrt{\frac{W_E}{W_M}} \tag{1.3}$$

$$\kappa_{ij} = g_{ij} d_{ij} E_p \tag{1.4}$$

According to whether the material is connected in an open-circuit or a short-circuit, the material would have a different value of stiffness. In case of application of a force in a short-circuit configuration, the electric charges deposited with opposite polarities on the electrodes will cancel each other, reducing the electric energy stored in the material. This reduction shall render the material to be of less stiffness than that of the open-circuit configuration. Therefore, two values of stiffness can be defined for the open- and the closed-circuit configurations, respectively, as K_{oc} and K_{SC}, where $K_{oc} > K_{SC}$. Among the interpretations of the Electromechanical Coupling Coefficient is that it relates the two stiffness values as described by equation (1.5).

$$\frac{K_{oc}}{K_{SC}} = \frac{1}{1 - \kappa^2} \tag{1.5}$$

1.3.3.4 Mechanical quality factor $\boldsymbol{Q_m}$*:*

The Mechanical Quality Factor indicates the degree of loss of the mechanical energy during resonance [20]. In other words, it indicates the sharpness of the resonance peak of the transducer [31]. It can be calculated using equation (1.6), which is eventually a function of the impedance characteristics and the frequency-response of the transducer.

$$Q_m = 2\pi \frac{stored\ mechanical\ energy\ at\ resonance}{mechanical\ dissipated\ energy\ per\ resonant\ cycle} \tag{1.6}$$

1.3.4 Other relevant parameters

The significance of the dielectric coefficient is that it characterizes the ability of a material, even a non-piezoelectric one, to store electrical energy. It is defined as the ratio of the charge stored in a dielectric material placed between two metallic poles to the charge that can be stored when the material is replaced by a vacuum. Hence, it is also called the relative electric permittivity. It can be calculated for each material as the ratio between its permittivity and the permittivity of the vacuum as indicated in equation (1.7). It is represented by a tensor of the second rank.

$$\zeta = \frac{\varepsilon_{material}}{\varepsilon_{vaccum}} \tag{1.7}$$

1.3.4.1 *The Elastic compliance constant S_{ij} :*

The elastic compliance constant is the ratio between the developed strain in the *i* direction and the stress applied in the j direction, given that the stress along the other two directions remains constant. It is modelled by a tensor of the fourth rank; however, it can be simplified as a 6 × 6 matrix due to the symmetry. Due to the discrepancy in the stiffness of the open and closed-circuit configurations, it is necessary to define a short-circuit Compliance, denoted as S_{ij}^{E}, and an open-circuit Compliance denoted as S_{ij}^{D}. Naturally, the short-compliance is greater than the open-circuited one, as compliance is inversely proportional to the stiffness.

It is worth mentioning that piezoelectricity is anisotropic, where the direction of pressure application relative to the direction of material poling has an effect on the generation of electric charges. Therefore, two coupling modes have been defined for the operation of piezoelectric materials: mode 31 and mode 33. As shown in Figure 1.4, mode 31 is the mode when the applied pressure is perpendicular to the material poling direction, while mode 33 is the mode when pressure is applied along to the poling direction [33].

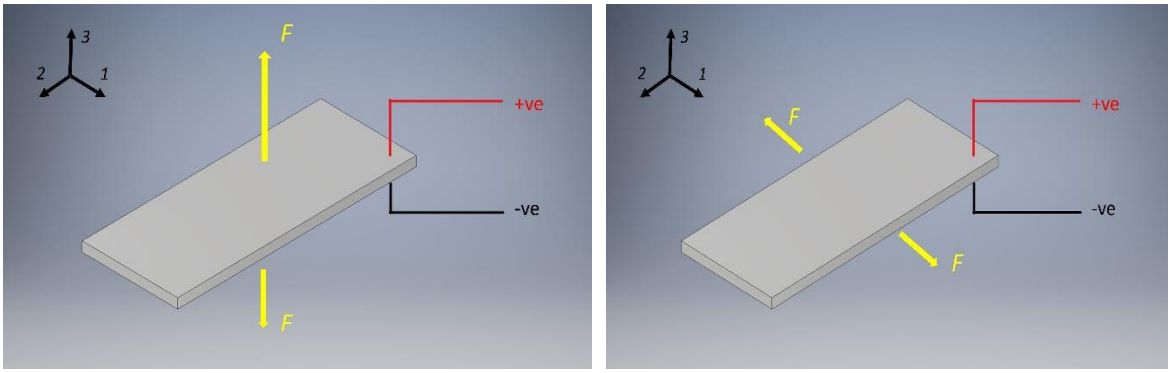

Figure 1.4 A piezoelectric material may operate in two different modes depending on the direction of the mechanical force in relative to the direction of material poling. (a) mode 33 (b) mode 31.

1.3.5 The piezoelectric constitutive equations

Any arbitrary material subjected to mechanical stress, *T*, shall develop a corresponding mechanical strain, *s*. The elastic strain can be related to the applied stress by Hook's law, equation (1.8), where T is the applied mechanical stress and *S* is the compliance tensor. It is a function of the Poisson's ratio and Young's modulus of the material [34].

$$s_j = S_{ij}\, T_j \tag{1.8}$$

For a piezoelectric material subjected to a general mechanical stress *T* and placed in a general electric field E, the electric field would induce in the material an additional strain to the mechanical strain described in equation (1.8). This additional strain is related to the

electric field *E* by the piezoelectric constant *d.* Hence, equations (1.9) and (1.10) were devised to calculate each of the overall generated electric displacement and the overall developed strain, respectively. In this system of equations, *D* and *s* are the electrical displacements and mechanical strain, respectively. ε^T is the relative permittivity at a constant mechanical stress, while S^E is the mechanical compliance tensor at a constant electric field. [*d*] and $[d^t]$ are the matrices of forward and Converse Piezo effects respectively [35]. Equations (1.9) and (1.10) are sometimes combined in a generalized matrix form as described in equation (1.11) [36]. However, this is a generalized representation, where the crystal symmetry in the piezoelectric material shall render many of the equation terms dependent or even zero. Such a fact considerably reduces the number of independent terms in the equation. For example, the poled ferroelectric ceramic PZT of a C_{6v} crystal class would have only two independent dielectric permittivity coefficients ($\varepsilon_{33}^T, \varepsilon_{11}^T = \varepsilon_{22}^T$), three independent piezoelectric constants (d_{33}, d_{31}, d_{15}) and five independent elastic constants under short circuit boundary conditions—$S_{11}^E = S_{22}^E$, S_{11}^E, $S_{44}^E = S_{55}^E$, $S_{12}^E = S_{21}^E$, $S_{13}^E = S_{23}^E$, and $S_{66}^E = 2(S_{11}^E - S_{12}^E)$.

$$[D] = [d]\{T\} + [\varepsilon^T]\{E\} \tag{1.9}$$

$$[s] = [S^E]\{T\} + [d^t]\{E\} \tag{1.10}$$

$$\begin{bmatrix} D_1 \\ D_2 \\ D_3 \\ s_1 \\ s_2 \\ s_3 \\ s_4 \\ s_5 \\ s_6 \end{bmatrix} = \begin{bmatrix} d_{11} & d_{12} & d_{13} & d_{14} & d_{15} & d_{16} & \varepsilon_{11}^T & \varepsilon_{12}^T & \varepsilon_{13}^T \\ d_{21} & d_{22} & d_{23} & d_{24} & d_{25} & d_{26} & \varepsilon_{21}^T & \varepsilon_{22}^T & \varepsilon_{23}^T \\ d_{31} & d_{32} & d_{33} & d_{34} & d_{36} & d_{36} & \varepsilon_{31}^T & \varepsilon_{32}^T & \varepsilon_{33}^T \\ S_{11}^E & S_{12}^E & S_{13}^E & S_{14}^E & S_{15}^E & S_{16}^E & d_{11} & d_{21} & d_{31} \\ S_{21}^E & S_{22}^E & S_{23}^E & S_{24}^E & S_{25}^E & S_{26}^E & d_{12} & d_{22} & d_{31} \\ S_{31}^E & S_{32}^E & S_{33}^E & S_{34}^E & S_{35}^E & S_{36}^E & d_{13} & d_{23} & d_{32} \\ S_{41}^E & S_{42}^E & S_{43}^E & S_{44}^E & S_{45}^E & S_{46}^E & d_{14} & d_{24} & d_{33} \\ S_{51}^E & S_{52}^E & S_{53}^E & S_{54}^E & S_{55}^E & S_{56}^E & d_{15} & d_{25} & d_{34} \\ S_{61}^E & S_{62}^E & S_{63}^E & S_{64}^E & S_{65}^E & S_{66}^E & d_{16} & d_{26} & d_{36} \end{bmatrix} \begin{bmatrix} T_1 \\ T_2 \\ T_3 \\ T_4 \\ T_5 \\ T_6 \\ E_1 \\ E_2 \\ E_3 \end{bmatrix} \tag{1.11}$$

1.3.6 The role of impedance

For an efficient electric power transfer from an arbitrary source to an arbitrary load, it is necessary that the load circuit and the source are of a matched impedance. This is realized by designing the load circuit to have an impedance conjugate to the source's. In such a case, the equivalent series impedance of the load and the source together will be minimized since the complex components of the two impedances cancel each other out [37].

Due to the inherent nature of piezoelectric materials structure, piezoelectric transducers possess an impedance of a resistive-capacitive nature. Hence, its equivalent circuit is composed of a frequency-dependant AC voltage source, a capacitor, and a resistor, as represented by the schematic diagram shown in Figure 1.5 [38]. This requires them to have an Electric Impedance Matching Network, EIMN, composed of inductors and resistors to realize an impedance-matched state [37].

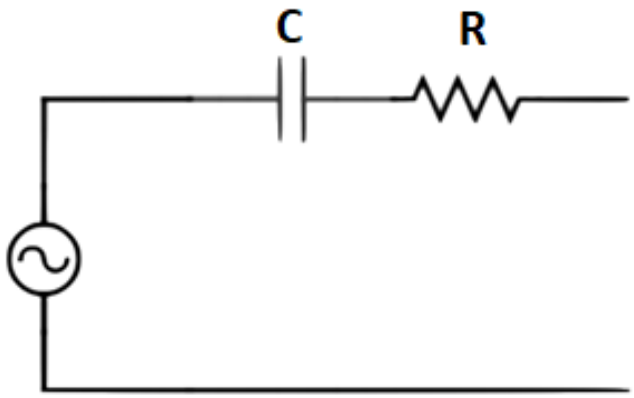

Figure 1.5 Equivalent circuit of a piezoelectric transducer

The problem with designing the impedance of piezoelectric materials, and generally of AC components, is that they are frequency dependent. As an example, the impedance of a capacitor of capacitance C across which flows a signal of frequency f is calculated using equation (4.4). Hence, the capacitor would have a different impedance value at each frequency. In the case of a harvester subjected to broadband energy, it would be challenging to optimize the harvester to the whole frequency band using this method.

1.4 Vibrations in the Environment:

The environment possesses various sources of vibrations. To name a few, the vibration of car parts, vibrations of railways, and vibrations of buildings. These vibrations are defined as mechanical vibrations. Apart from mechanical vibrations, a body may undergo Flow-Induced Vibrations, FIV, upon being subjected to a fluid flow.

FIV is a broad branch of vibrations that includes: Vortex-Induced Vibration—VIV—, Flutter, and Galloping [39]. VIV is a form of a limited-amplitude vibration created by the loads induced during the vortex shedding off a bluff body, a cylinder specifically. On the other hand, Galloping is a kind of vibration that depends on the variation of the flow angle of attack over time. Therefore, it requires a non-symmetric bluff body—not a circular cylinder—to form. Finally, Flutter is a form of vibration similar to VIV with the difference that it involves the interaction of the elastic deformation of the bluff body with the aerodynamic loads. Hence, it is a self-feeding vibration and can be mainly found in plate-like bodies [40] [41]. In the next section, VIV shall be discussed in more detail.

When a flow of a low Reynolds Number, *Re*, flows past a bluff body, a regime of vortices is formed in the body wake region. This regime induces periodic loads on the body, causing its vibration. As the Reynolds number increases, the nature of the vortex regime will change, causing the increase of the vortex shedding frequency $f_{s.}$ until the vortex train becomes fully turbulent and chaotic. If the vortices—hence, the loads—are formed with a frequency equal to the natural frequency of the transducer, the transducer goes through resonance in a state known as *Lock-in* [42]. The reader may refer to [43] as a review on the different vortex shedding regimes.

The frequency of vortex shedding is defined by the Strouhal number, *St*, which is the ratio between the inertial force of the vortices to the inertial force of the flow main stream [44]. Extensive work has been done to determine the value of the Strouhal number. This work has resulted in several empirical models that relate the Strouhal number to Reynolds number [45].

1.5 Piezoelectric Energy Harvesting:

1.5.1 How is the energy harvested?

Since vibrations create a pressure effect, the piezoelectric effect can be used to harvest the energy of vibrations to convert it into useful electricity. When a pressure wave is induced in the piezoelectric transducer, a corresponding amount of electric charge shall be generated on the material surface, developing an electric potential. Moreover, if the direction of the stress is reversed in succession, this would lead to an AC voltage developing across the two poles of the material. Hence, piezoelectric materials are used to harvest the energy of mechanical vibrations using a Piezoelectric Energy Harvester, PEH.

A PEH is constructed such that it consists of several main blocks, as shown in Figure 1.6. First, it starts with the excitation source, which is the incident energy. In some cases, there is a special mechanism of energy transfer and amplification that ensures an efficient energy pick-up by the transducer. Such a stage is more common in the harvesters dedicated to harvesting acoustic vibrations. Then in the third stage, the transducer converts the

transferred mechanical energy into electric energy. Finally, there is the electric energy handling module in the form of power electronics and energy storage units[46] [47].

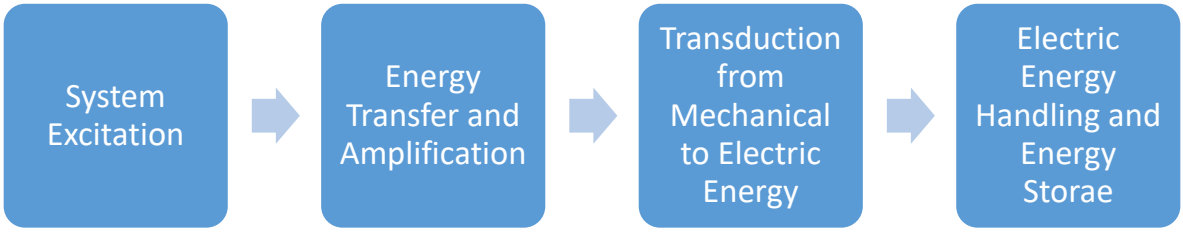

Figure 1.6 A schematic diagram of a Piezoelectric Energy Harvester, PEH.

As simple as the basic idea is, the design of a PEH is quite complicated due to the widely variable nature of the vibrations' pressure wave. A pressure wave can be harmonic, e.g. acoustic waves and vibration due to rotary parts, or it can be totally random. Even a harmonic wave could be a simple harmonic wave, e.g. a tonal sound, or it can be a complex harmonic wave formed of several harmonic waves that are superimposed together. Unfortunately, most of the vibrations present in the environment are rather random or complex harmonics, thus complicating the process of accommodating a harvester to its optimum operating conditions.

1.5.2 Types of PEH

PEHs have been developed in different designs. The most common types are Cantilever-type, Cymbal-type, Stacked-type, and shell-type—as summarized in Figure 1.7. A Cantilever-type PEH is composed of a piezoelectric beam that is fixed from one end while subjected to the bending force from the other, as shown in Figure 1.8. The beam may be composed of either a uni-morph[8] or a bimorph[9] piezoelectric transducer. A Cymbal-type PEH is composed of a piezoelectric disk, mostly a ceramic, placed between two steel endcaps, as shown in Figure 1.9. The load acts vertically on the endcaps causing the disk to develop radial strain and hence, generating electric charge [48]. This structure allows for the generation of a large in-plane strain, and hence electric charge, from transverse loads [13]. A Stack-type transducer is composed of several layers of piezoelectric layers stacked together in a parallel electrical connection. Such a connection allows for a large generated electric energy since the overall transducer will have large capacitance and will be operating on the d_{33} mode [13]. Finally, the Shell-type transducer is composed of a slightly-curved piezoelectric plate. The curvature of shell structure shall make it generate more strain than a flat one,

[8] A piezoelectric transducer formed of one piezoelectric layer.
[9] A piezoelectric transducer formed of two piezoelectric layers mounted parallel to each other.

which means that shell structure can generate more electric charge than its flat counterparts [13].

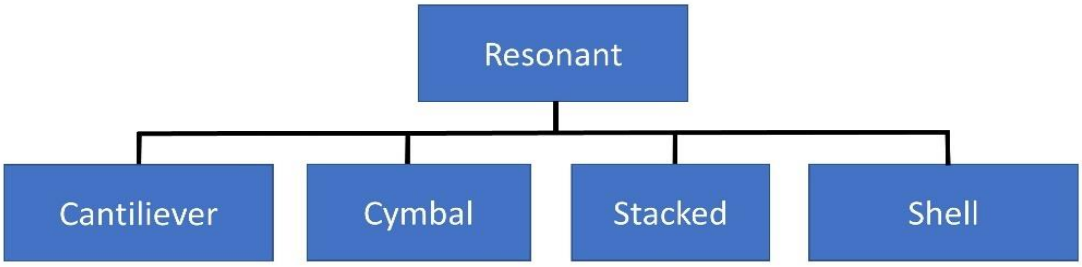

Figure 1.7 Types of piezoelectric energy harvesters

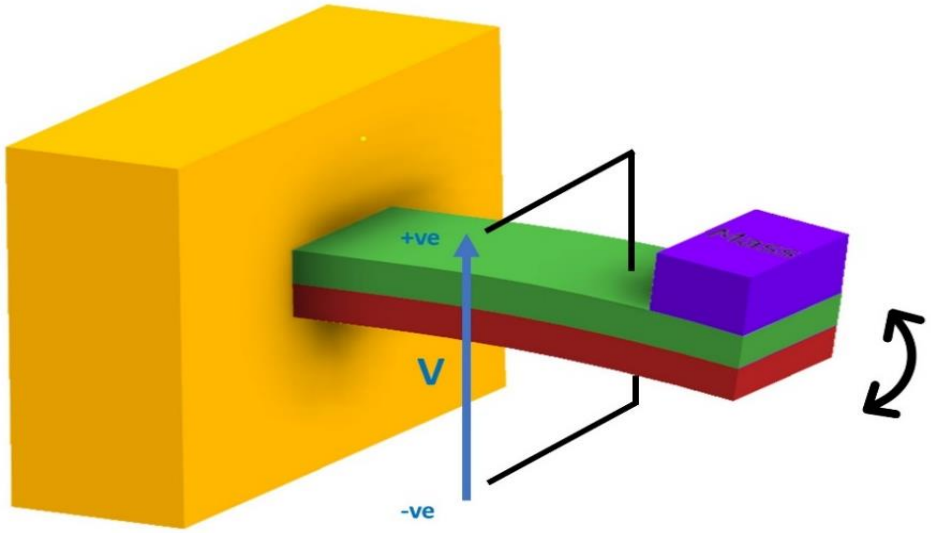

Figure 1.8 A bi-morph cantilever-type Piezoelectric Energy Harvester, PEH.

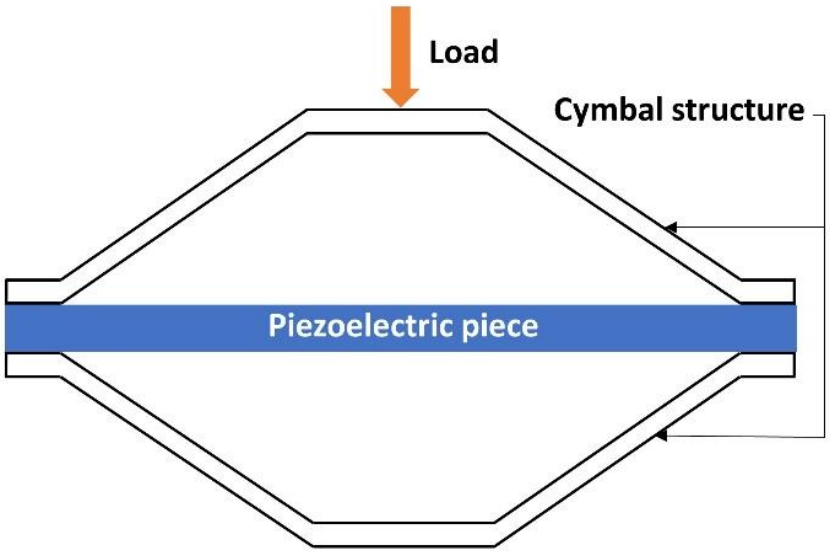

Figure 1.9 A cymbal-type Piezoelectric Energy Harvester, PEH.

1.6 Acoustic Energy Harvesting, AEH

Various energy harvesters have been developed to harvest the energy of mechanical vibrations in different configurations. Examples of such harvesters can be found in the reviews presented in [13] and [47]. Since the work in this thesis has focused on Acoustic Energy Harvesting—AEH— and FIV, respective examples shall be discussed in more detail.

Several practical designs for AEH units have been implemented. Hassan et al. [6] investigated the possibility of sound energy harvesting using a PZT-5A cantilever type and sound produced from speakers. They operated the transducer in two different modes: 31 and 33. They managed to harvest 0.0267 V_{rms} at a Sound Pressure Level, SPL, of 78.6 dB at the resonance frequency of 62 Hz in the first mode and 0.090 V_{rms} at SPL of 102.6 dB and a resonance frequency of 374 Hz in the second mode.

Hee-Min Noh [49] designed an AEH unit that can harvest noise from high-speed trains. His device used a Helmholtz resonator designed for a frequency of 174 Hz based on a theoretical model. He managed to harvest 0.7 volts of electricity from an incident sound pressure level of 100 dB using a rectangular plate.

Monroe [50] has designed a large-scale AEH unit that targets wide broadband of incident sound frequency. The unit is based on a PVDF film that is 100 cm^2 in size. It can operate on frequency broadband by matching the electric load to be conjugate to the total electric impedance of the AEH unit itself. This matched load is executed by means of an operational

amplifier circuitry. It was reported that it was possible to harvest 1.6 μJ per take-off of a 747 aircraft, with most energy losses occurring at low sound frequencies.

Salem et al. have studied AEH using piezoelectric materials. They first studied harvesting using a piezoelectric buzzer in [46]. They performed open- and closed-circuit tests. The open-circuit test was performed considering full-wave rectification. The test extended over frequency up to 20 kHz. The authors were able to find a very significant voltage spike at a frequency of 523 Hz. The double of this frequency, owing to the frequency doubling due to rectification, was found to represent 87.1% of the buzzer's natural frequency. The closed-circuit test was performed using resistances up to 2700 kΩ. The harvested power was found to change abruptly with the change in the load resistor, and they were able to harvest a maximum power of 43 nW at a resistance of 10.2 kΩ. This work has shown how sensitive a PEH can be to the frequency of acoustic waves as well as the configuration of the load circuit.

Yuan et al. proposed a low-frequency broadband acoustic energy harvesting unit that can harvest 2.4 μW at 100 *dB* of incident sound SPL. It has an extended bandwidth around the acoustic resonant frequency. The design uses a Helm-Holtz resonator in the form of slits [51]. Chen et al. designed another AEH unit that can harvest 0.9 V/(m/s^2) and 1.79 2.4 μW/(m/s^2)^2 by bandwidth tuning. They followed a mathematical model as well as an experimental approach and differences were found to be ranging from 1 to 6 % [52]. Khan et al. designed a bi-morph composite AEH that is improved with a tapered Helm-Holtz resonator cavity. It was found that the tapered cavity improves the generated power by 76.26% over a cylindrical cavity [53].

To assess the quality by which an energy harvester can harvest vibration energy, it is necessary to define a qualitative measure that would describe such a process. Mostly, researchers tend to use efficiency, η, which is the ratio of the output of useful electric energy to the input of mechanical vibration energy. This number stands as the resultant final efficiency of the overall harvester taking into account all the factors governing its performance, such as the electromechanical coupling factor of the material, the geometry of the transducer, the inhibited mechanical damping in the system, and the electrical damping characteristics of the load as well as of the whole circuit. Despite how simple the definition of efficiency is, it is quite challenging to agree on a strict way to evaluate efficiency because of the practical constraints on measuring the input energy. Therefore, large discrepancies can be found in the value of efficiency reported in the literature, where it can be estimated to be as high as 80% by some researchers, while others claim that it can never be more than 50%.

Yang et al. [54] presented an overview of work conducted studying the efficiency by which piezoelectric energy harvesters convert energy. They reported that PZT (lead zirconate titanate)-based energy harvesters harvesting vibrational energy had the highest theoretical

efficiency in the range of 50–90%. Richards et al. [55] derived a formula to calculate the efficiency in the case of a system operating at the resonance frequency and a matched impedance with the load. They considered systems of low damping and high mechanical coupling. Their theoretical study predicted that efficiency can be higher than 90%. However, high values of coupling are rarely achieved experimentally to justify this result. Shu et al. [56] also devised a formula for the calculation of efficiency that was based on the material coupling coefficient, mechanical damping, and normalized values of each of the harvested sound frequencies as well as the electric resistance. Maximum efficiency of 46% was reported for harvesters of weak coupling, while a maximum efficiency of more than 80% was reported for harvesters of strong coupling.

Liao et al. [57] have proposed a different way to assess the performance of piezoelectric energy harvesters, where they derived a new efficiency that is analogous to the material loss factor. This efficiency is calculated as the ratio between the strain energy over each cycle and the power output. They validated this new quantity by numerical simulations, and it was estimated that harvesters would have a maximum efficiency of 2.5% around the resonance frequency.

Yuan et al. [58] also compared various designs of acoustic energy harvesters reported in the literature. They did not base their comparison on the efficiency of energy conversion of these harvesters; however, they derived their own parameter and called it "Metric". Their parameter is set to give a higher score for a smaller harvester that is able to harvest more power at a lower input sound power. Therefore, they devised their Metric according to equation (1.12), where it is set to be the ratio between the harvested power and the product of the harvester volume and the square of the involved sound pressure, where *P*, *Vol* and *Π* are the harvested power in μW, the harvester volume in cm^3 and the involved sound pressure in Pascals, respectively. Their motivation behind using a squared value of sound pressure is that sound intensity is proportional to the square of sound pressure, as shown in equation (1.13) which relates sound intensity I to the sound pressure *Π* via the acoustic impedance $Z_{acoustic}$.

$$Metric = \frac{P}{Vol \times \Pi^2} \tag{1.12}$$

$$I = \frac{\Pi^2}{Z_{acoustic}} \tag{1.13}$$

Using their parameter (i.e., *Metric*), the authors rated seventeen different designs of acoustic energy harvesters from the literature. The harvesters' operating conditions—sound frequency and pressure—spanned over a wide range. The list included harvesters

operating at a sound frequency in the range of 146–13570 Hz, with most of the list targeting frequencies under 1 kHz. On the other hand, the operating sound pressure ranged over 1–563.7 Pa, which corresponds to an SPL of 94–149 dB. Sixteen designs out of the presented seventeen achieved a value of *Metric* in the range of 7.7228×10^{-12} – 0.1885 $\mu W/(cm^3.Pa^2)$, while one last design achieved 14.536 $\mu W/(cm^3.Pa^2)$.

1.7 Forced-Induced Vibrations Harvesting

In addition to harvesting acoustic energy, various Piezoelectric Flow Energy Harvesters, PFEH, have been developed to harvest the energy of a flowing stream. In fact, they have proved to be advantageous over classical rotary wind turbines that use electromagnetic electric generators for energy conversion. The absence of such elements in a PFEH allows it to have a less complex system that can operate at a less wind cut-in speed compared to rotary turbines [59]. Such a fact nominates PEHs as a better alternative for cases of harvesting energy of wind that is not strong enough to start classical wind turbines. These harvesters rely on a turbine to extract the flow's kinetic energy and transfer it into a piezoelectric transducer, where it is converted into electrical energy. Examples of such harvesters can be found in [60], [61], and [62].

Moreover, Piezoelectric Vortex-Induced Vibration Harvesters, PVIVH, have been developed to harvest the energy of VIVs, where a bluff body is inserted into a flow to create vortices. The vortices' energy is then harvested by adding a PVIVH that makes use of the variation in fluid pressure due to the turbulence.

The process of vortex shedding and its resultant VIV has long been used in energy harvesting devices. Harvesting the energy of VIV has in fact, started with harvesting the VIV from water flow [63]. Examples of such work could be found in [64, 65], while work focused on harvesting VIV from airflow is presented in the next section.

Pobering et al. [66] have developed a harvester composed of three piezoelectric bimorph cantilevers mounted behind a bluff body. The harvester was tested inside a wind tunnel at a wind speed of 4.5–45 m/s. The harvester generated a maximum voltage of 0.83 Volts at an airflow velocity of 35 m/s and generated power up to 108 µW at a velocity of 45 m/s. Gao et al. [67] presented a PVIVH based on a piezoelectric cantilever coupled with a cylindrical extension. The cylinder in the cross-flow was free to vibrate and was attached directly to a piezoelectric device. The harvesters' power output was found to increase with the wind velocity and cylinder diameter. Lee et al. [68] have developed a PEH composed of a cylindrical oscillator suspended on a silicon cantilever covered with a piezoelectric

aluminium-nitride layer. The harvester was tested inside a wind tunnel alone as well as with other dummy cylinders in various configurations. It was found that increasing the number of turbulence shedding bodies—the dummy cylinders—from one to twenty-five has increased the harvested power from 0.8 to 1.6 nW at a flow speed of 6 m/s.

Akayidin et al. [69] designed a PEH composed of a short piezoelectric PVDF cantilever placed in the wake of a vortex-shedding cylinder. The harvester was tested inside a wind tunnel at an airflow speed of 7.23 m/s. Such a speed was chosen such that the shedding frequency is matched to the harvester's resonance frequency of 48.5 Hz. The harvester was able to generate 4 µW of power. Moreover, they tested the harvester with the cantilever placed at different distances from the cylinder, both span- and downstream-wise. They found that the harvester generated maximum power at an intermediate stream-wise distance from the cylinder. Either increasing or decreasing this distance would reduce the harvester output.

The only mention of a VIV energy harvester that was not based on a cantilever transducer was by Xie et al. [70]. They have numerically studied harvesting the energy of VIV via a cylindrical piezoelectric transducer immersed across an airflow of a speed of 5 m/s. The cylinder material was assumed to be PZT-5H and to have a resonance frequency of 98.5 Hz. The study was based on mathematical modelling of the energy harvesting process considering a model based on the piezoelectric constitutive equations, the flexural bending moment of a beam of a general profile, the equation of aerodynamic loads acting on a cylinder in a flow, and the equation of motion of the cylinder flexural vibration. They simulated cases of different load impedances as well as cases of different load frequencies. Their results showed that maximum power was produced at a frequency slightly higher than the resonance frequency and at a load impedance that is five times larger than that of the cylinder. However, the maximum efficiency was produced at a load impedance equal to that of the cylinder.

1.8 Contribution of this Research to the Current State-of-the-art

Piezoelectric transducers may be used in different shapes. Most of the current research has been done on piezoelectric transducers in the shape of cantilevers. Other work has tackled circular desks, plates, annular desks, and cymbal-shaped transducers. Despite the fact that there are some applications that may benefit from the cylindrical geometry, there has not been much work done that was based on cylindrical piezoelectric transducers.

Despite the complications that a cylindrical geometry might impose on studying the vibration of the piezoelectric body, the geometry may yet have its advantages. In the case of AEH, the relatively bigger size of the transducer—the diameter compared to the thickness in other transducers—could make the transducer interact better with the large wavelength of the acoustic wave, enhancing the process excitation and hence the process efficiency. Therefore, the first part of this thesis studies the harvesting of acoustic energy using cylindrical piezoelectric transducers and looks at the relation between the transducer size and the quality of harvesting.

The cylindrical shape may have interesting applications in the harvesting of flow energy as well. According to the presented review on FIV harvesting, the current PVIVHs are based on putting a cylinder, a non-piezoelectric one, across the flow of a fluid. Being interrupted by the cylinder, the flow would flow across the cylinder, inducing a wake region in the flow from which a vortex train is shed before it interacts with a cantilever-based PVIVH [71]. The thesis shall investigate if the introduction of piezoelectric cylinders to this system would help make it more compact.

Therefore, the second part of this thesis studies the applications of cylindrical piezoelectric transducers in the field of VIV energy harvesting. The study investigates experimentally the reaction of cylindrically-shaped transducers of different sizes to the energy existing in the airflow, taking into consideration the models found in the literature on vortex shedding off circular cylinders. Moreover, it shall look at the effect of windspeed and the load circuit on the quality of the harvesting process.

The thesis starts with Chapter 1, which presents an introduction to energy harvesting, piezoelectricity, and forced-induced vibrations. Then, Chapter 2 presents the used piezoelectric materials. Then, Chapter 3 presents the measurement of the impedance of the used transducers. Then, Chapter 4 presents the work done on the harvesting of narrow-banded vibrational energy. Then, Chapter 5 presents the work done on the harvesting of broadband vibrational energy. As will be discussed later, the narrowband energy harvesting was realized using mono-frequency acoustic waves, while the broadband energy harvesting was realized using vibrations induced in the flow. Finally, Chapter 6 concludes the results presented in the thesis, while Chapter 7 makes recommendations for future efforts on the topic.

2 Material Specification

The four cylinders understudy are made from PIC 151, which is a modified lead Zirconate - Titanate (PZT-5A). The cylinders are poled radially, where the positive electrode is fired on the inner surface and the negative electrode on the outer surface. A wire was soldered on each pole for electric connections. The piezoelectric material has piezoelectric parameters, as shown in Table 2-I. It has a piezoelectric voltage constant of 0.022 $Vm.N^{-1}$ in the 33 direction and -0.115 $Vm.N^{-1}$ in the 31 direction. The material has frequency constants in the radial mode N_p and in the thickness modes N_t, both of 1950 Hz.m. It has a mechanical quality factor Q_m of 100%. Finally, it has elastic compliance coefficients S of 15×10^{-12} and 19×10^{-12} N/m^2 in the 11 and 33 directions, respectively.

Table 2-I Piezoelectric characteristics of the piezoelectric material

Quantity	Value
Piezoelectric voltage Constants $[10^{-3}\frac{Vm}{N}]$	$g_{33} = 22$
	$g_{31} = -11.5$
Frequency constants [Hz.m]	$N_p = 1950$
	$N_t = 1950$
Mechanical quality factor Q_m [-]	100%
Compliance $[\times 10^{-12}\ N/m^2]$	$S_{11}^E = 15$
	$S_{33}^E = 19$

The four cylinders were provided by the supplier with specific characteristics as summarized by Table 2-II. The four cylinders—A, B, C, and D—have diameters D_{cyl} of 40, 20, 10, and 6.3 mm, respectively. The 40 mm cylinder has a length L_{cyl} of 40 mm, while the other cylinders have a length of 30 mm. These dimensions form an Aspect Ratio, as described in Table 2-II, ranging from 1–4.76.—Unfortunately, it was not possible to control the cylinder aspect ratio since it depends on the dimensions combinations provided by the supplier—.The four cylinders—A, B, C, and D—have electric capacitance C of 70, 35, 36 and 18 nF, respectively. Finally, the cylinders have resonance frequencies as described in Table 2-II.

It was possible to calculate the resonance frequency of the cylinder in the thickness direction F_{r_t} and in the radial direction F_{r_p} from the respective frequency constants N_t and

N_P, using equations (2.1) and (2.2), respectively. From the values of $\mathrm{F_{rp}}$, it can be seen that Cylinder (A) of diameter 40 mm had the least resonant frequency, yet still outside of the acoustic range.

$$F_{r_t} = N_t/t \tag{2.1}$$

$$F_{r_p} = N_p/D_{cyl} \tag{2.2}$$

Table 2-II Individual characteristics of the piezoelectric cylinders.

Item	**Cylinder (A)**	**Cylinder (B)**	**Cylinder (C)**	**Cylinder (D)**
Diameter D_{cyl} [mm]	40	20	10	6.3
Length L_{cyl} [mm]	40	30	30	30
Thickness t [mm]	1	1	0.5	0.5
Aspect Ratio L_{cyl}/D_{cyl} [-]	1	1.5	3	4.76
Electric Capacitance C [nF]	70	35	36	18
Radial-mode Resonance frequency $\mathrm{F_{rp}}$ [kHz]	48.75	97.5	195	309.524
Thickness-mode Resonance frequency F_{r_t} [kHz]	1950	1950	3900	3900

3 Measuring the Cylinder Impedance:

During the work on AEH presented later in Chapter four, it will be necessary to have information on the cylinder's electrical impedance and how it changes with the change in frequency. Therefore, the measurement described in this chapter was designed and performed in order to completely map the electric impedance with its two components, resistive and reactive, over a wide frequency spectrum. The goal of such mapping would be:-

- To identify the frequencies at which the cylinder would have minimum total impedance, which means the least opposition to the generated current.
- To quantify the resistive and reactive impedance components to be able to define the needed physical components of the load circuit that would achieve matched impedance between the source, the cylinder, and the load circuit. This would be necessary due to the effect of impedance matching on the efficiency of the process of energy harvesting [72].

According to need, this measurement was performed only on Cylinder (A), of a diameter of 40 mm. The impedance information of other cylinders was not required, as they were not considered for the closed circuit experiments of AEH for reasons that will be described later in Section 4.3.2.

3.1 Experiment Set-up

The set-up is composed of the piezoelectric cylinder connected to the measuring device, which is an Impedance Precision Analyzer 4294A equipped with a 16047E test fixture. However, there were two main challenges in the design of the set-up. First was how to electrically connect the cylinder to the analyser probes, the test fixture. Secondly was how to provide damp-free mechanical support to the cylinder. It was necessary to ensure that the cylinder is mechanically damp-free; otherwise, any damping effect from the supports may alter the way the cylinder vibrates, which would in return alter the measured electric impedance.

These two challenges were overcome by means of two pieces of metal wire. These two wires, being electrically conductive, act as connection points to the test fixture where one of them touches the cylinder at one pole, the inner surface, while the other one touches the cylinder at the other pole, the outer surface. Each wire is clamped by the respective probe of the test fixture, as shown in Figure 3.1, making the analyser probes act as the ground on which the cylinder is supported. Thanks to the fact that the wires support the cylinder at two points only, this support system can be considered vibration-damp-free. In a nutshell, the wires act as electrical connection points as well as mechanical support.

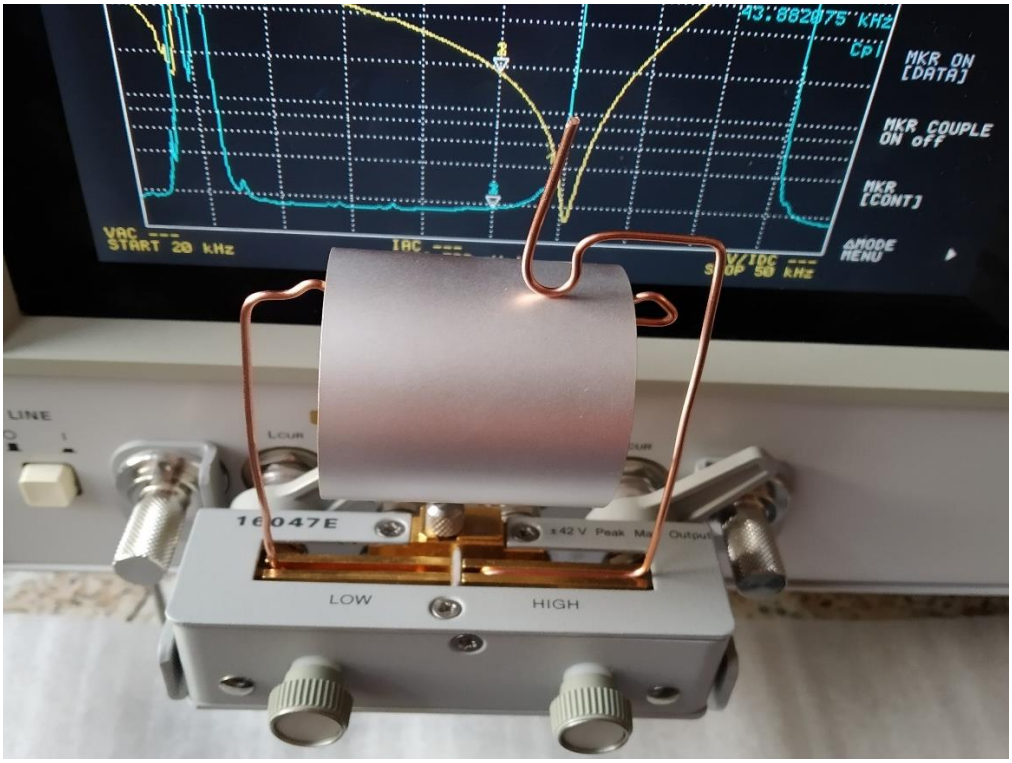

Figure 3.1 Supporting the cylinder on the test fixture using two metal wires for impedance measurement.

3.2 Methods

After mounting the cylinder on the analyser, the analyser is operated in a Direct-Current-Voltage mode, where it supplies the cylinder with electric signals over a wide frequency range. Then, it measures the formed impedance inhibited by the cylinder. The measurement was done on a frequency range of 40 Hz up to 50 kHz using a linear frequency sweep with increments of 15 Hz. The used oscillation level was 500 milli-Volts without a DC bias. According to the manufacturer, the device has an impedance measurement accuracy of ±0.08%. The raw results of this measurement are the absolute impedance amplitude, Z, and the phase difference Φ.

3.3 Results

3.3.1 Variation of the overall electrical impedance over the frequency range:

Using the Precision Impedance Analyzer, It was possible to measure both the electrical impedance amplitude, Z, and the phase difference Φ, as shown in Figure 3.2 and Figure 3.3, respectively. As can be seen in Figure 3.2, the impedance tended to decrease monotonically with increasing frequency, with only one exception in the form of an impedance spike occurring at a frequency of 47 kHz. This result means that the higher the incident frequency is, the more suitable the cylinder is for harvesting since it will have less impedance. However, since the current interest is in the harvesting of acoustic energy, there will be

limitations on the used frequency to be up to 20 kHz, the audible range. In such a case, the cylinder would be recommended to be used at the maximum audible frequency possible. For other applications involving ultrasonic waves, the cylinder would be operating at its optimum conditions.

Figure 3.3 shows the variation of the phase difference, Φ, versus the frequency. It is important to notice that the phase difference has a value that is very near to -90° over most of the range and especially in the range of acoustic spectrum up to 20 kHz. This means that in this range, the cylinder would have negligible resistance relative to the reactive impedance. Also, it can be noticed from the same figure that the phase difference jumps to a positive value twice. However, these jumps occur outside of the audible frequency range at approximately 23 kHz and 45 kHz.

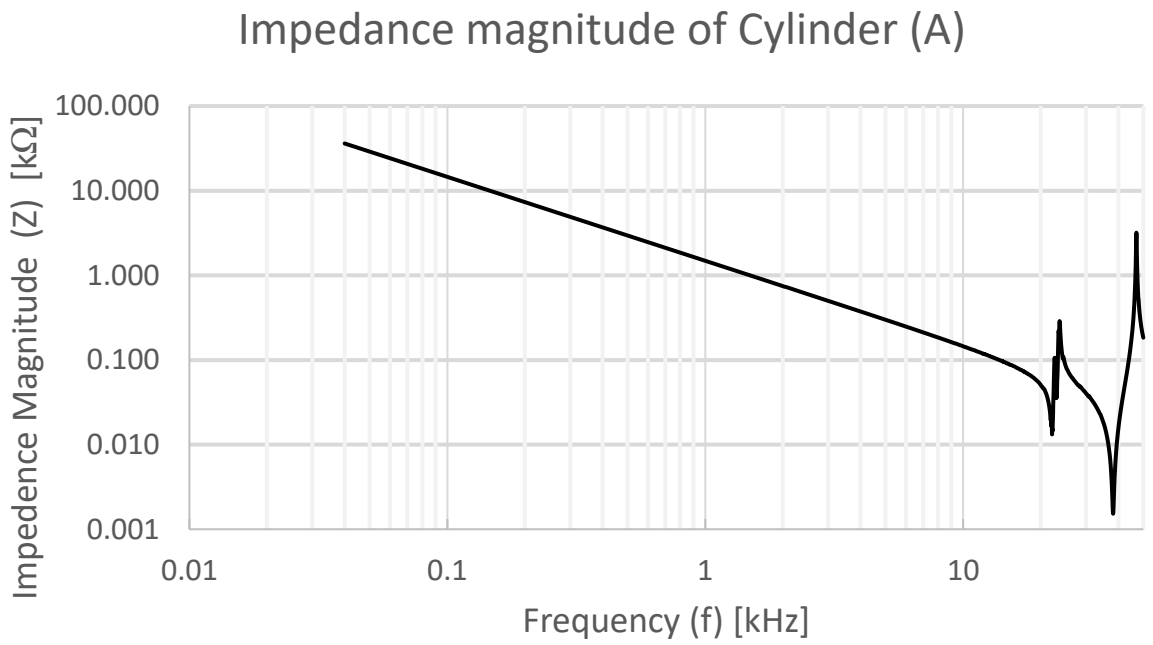

Figure 3.2 Variation of impedance magnitude across frequency for Cylinder (A)

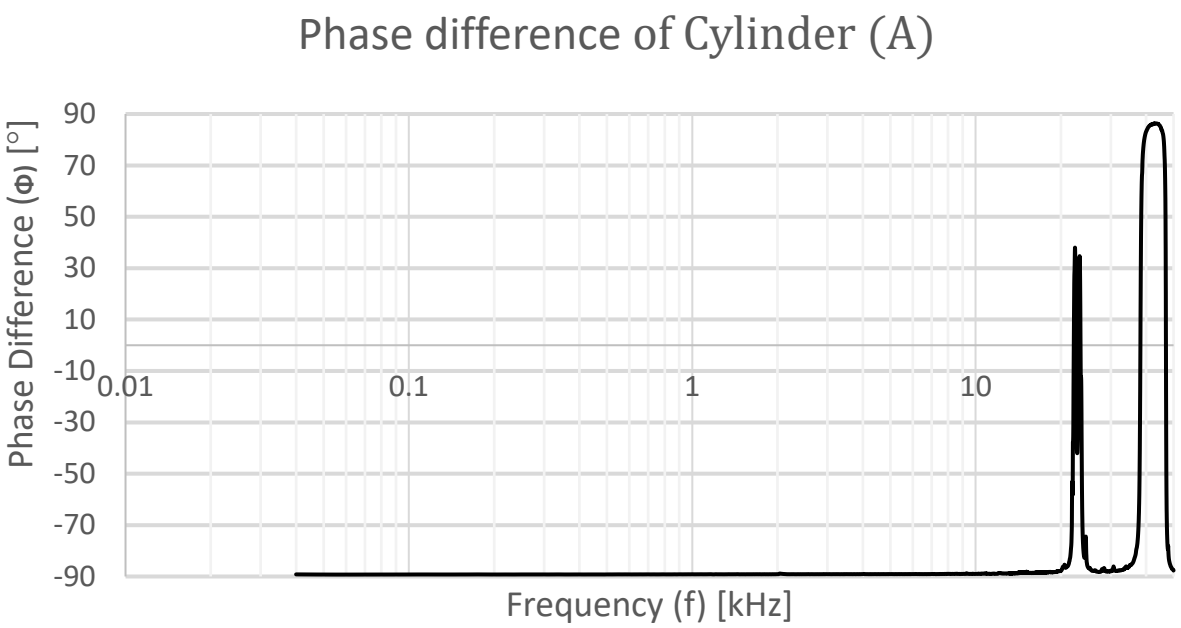

Figure 3.3 Variation of phase difference across frequency for Cylinder (A)

3.3.2 Variation of the resistive and reactive impedance components:

Using the values presented in Figure 3.2 and Figure 3.3, it would be possible to use equations (3.1) and (3.2) to calculate both the resistive, *R*, and the reactive, *X*, components of the impedance as shown in Figure 3.4 and Figure 3.5 respectively. Thanks to these data, it would be possible, when the cylinder is placed in a closed circuit, to select the specific electric components needed to balance the electric circuit relative to the cylinder.

In Figure 3.5, it can be noticed that the cylinder has negative reactive impedance *X* over the whole range. It is worth mentioning that the resultant reactive impedance *X* is the result of subtraction of the capacitive impedance, X_c, from the inductive impedance, X_l. Thus, having negative reactive impedance, *X,* means that the cylinder has a prevailing capacitance nature.

$$R = Z\ cos(\Phi) \tag{3.1}$$

$$X = Z\ sin(\Phi) \tag{3.2}$$

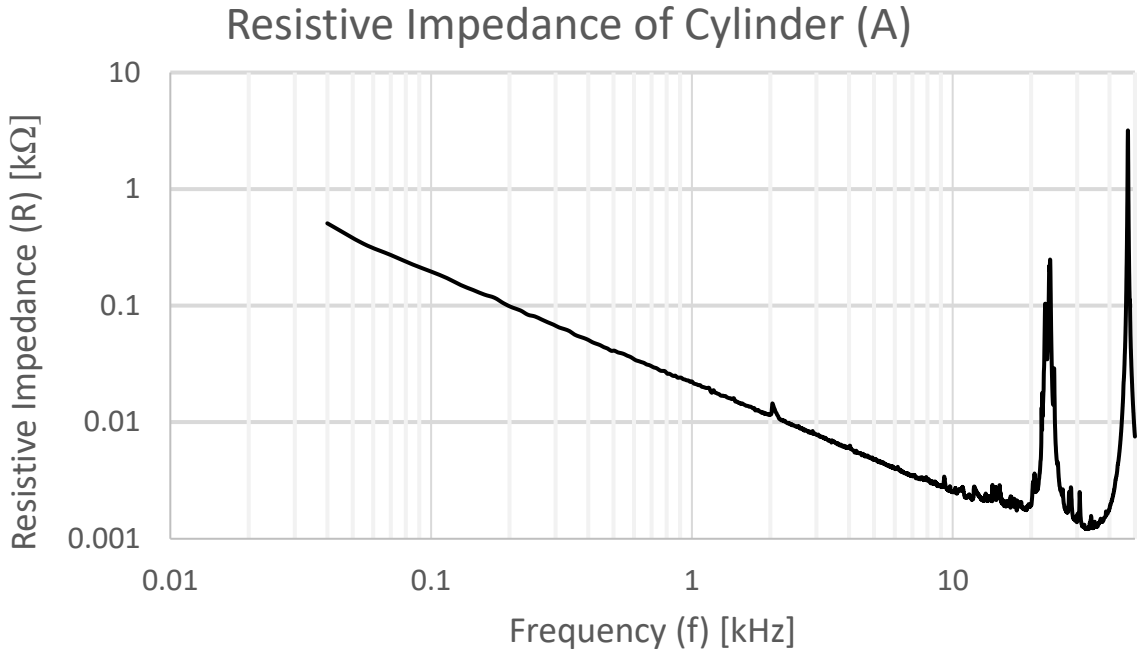

Figure 3.4 Variation of resistive impedance component across frequency for Cylinder (A)

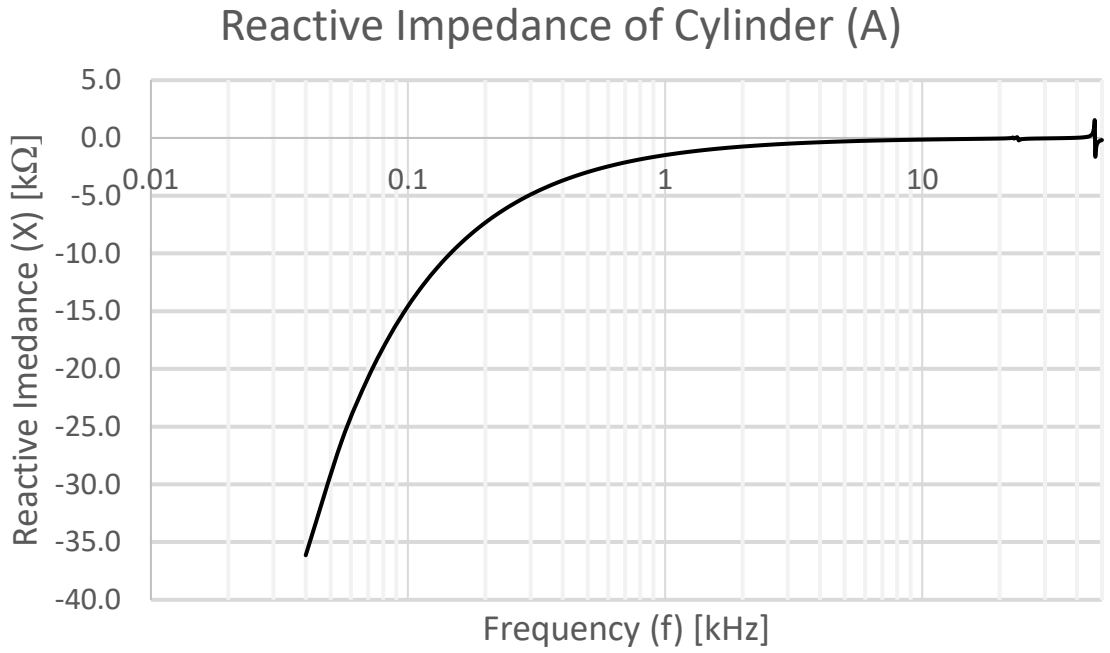

Figure 3.5 Variation of the reactive impedance component across frequency for Cylinder (A)

4 Mono-Frequency Energy Harvesting (Tonal):

4.1 Concept:

As was previously mentioned, the performance of the piezoelectric transducer is affected by the frequency characteristics of the incident energy. Hence, the quality of harvesting acoustic waves is affected by the incident sound frequency. Moreover, it is affected by the characteristics of the electric load. Therefore, the Single-Frequency Energy Harvesting measurements were performed to study this combined effect. The measurements are divided into two main parts: *Open-circuit measurements* and *Closed-circuit measurements.* For convenience, the two parts shall be defined as "*Phase (1)*" and "*Phase (2)"* respectively.

The open-circuit measurements were designed to study the effect of the incident sound frequency on energy harvesting. In this set of experiments, the transducer is not connected to any electric load. Nevertheless, the transducer is connected to a full-bridge rectifier, where only the transducer's open-circuit voltage is measured. In the closed-circuit measurements, the electric load shall be varied systematically in order to find the optimum electric load for maximized energy harvesting.

Moreover, it is worth mentioning that at this stage, only Cylinders (A) and (B), the 40 and the 20 mm cylinders, were considered for AEH measurements as they had the least resonance frequency, as indicated in Table 2-II.

4.2 Experiment Set-up:

As shown in Figure 4.1, the setup was built such that it was composed of speakers (1) supplying acoustic waves of a controlled frequency onto the cylinder (2). To do so, aluminium profiles were assembled to form a crane (3) from which the cylinder could be hanged. The cylinder was hanged from the crane using a malleable metallic strap (4) covered with a plastic cover (5). The cover was intended to have two functions: the first function was to electrically insulate the cylinder from the conductive aluminium frame, while the second function was to protect the cylinder's surface from scratches that may develop from metal-to-metal contact with the strap. Such a measure was necessary as such cracks may degrade the piezoelectric material.

After supporting the cylinder from the frame, the speakers were placed such that sound waves would be applied radially onto the cylinder. The main consideration behind the design of this setup was to support the cylinder from one point to avoid damping the vibration of the cylinder. Moreover, the design aimed to minimize the effect of sound reflection. This was achieved by minimizing the number of objects—including the ground—that were in the vicinity of the speakers.

The cylinder was connected to a breadboard by a pair of electric wires that were soldered to the inner and outer surfaces of the cylinder. Into the breadboard, four Schottky diodes

BAT 48 were mounted, forming a full-wave rectifier as shown in Figure 4.2, where the cylinder was modelled as an AC source. The BAT 48 diodes were produced by STMicroelectronics and were specifically preferred for their relatively low forward voltage value, $V_{f,}$ as it had a V_f of 240 mV only. Hence, it was determined that a total voltage drop of 480 mV should be imposed on the output of this circuit.

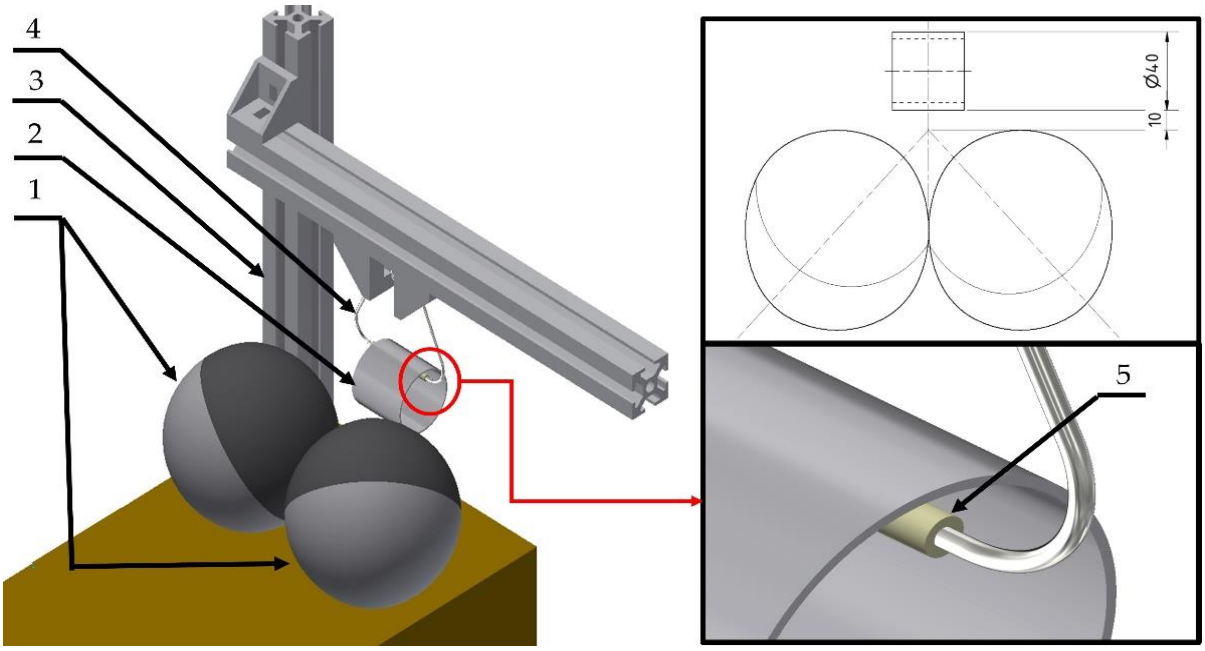

Figure 4.1 The setup of the Acoustic Energy Harvesting, AEH, experiment.

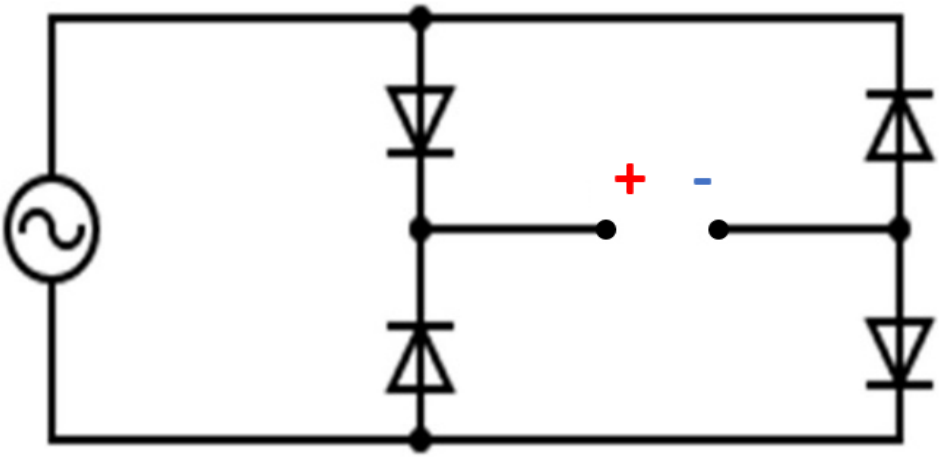

Figure 4.2 A schematic representation of the source circuit used in the Acoustic Energy Harvesting, AEH, experiment.

4.3 Open-circuit Measurements:

4.3.1 Methods:

In Phase (1), the cylinder was subjected to sound waves of different frequencies while the generated voltage over the bridge poles was monitored. The experiment was set up as defined above such that the distance between the speakers and the cylinder was almost 1 cm. A frequency sweep was performed from a frequency of 20 kHz, in steps of 1 kHz, up to a frequency of 1 kHz. Then, a step of 200 Hz was used from 1000 Hz up to 200 Hz. In case a peak point was found, additional measurements were performed in a range of 1 kHz centred at the found peak with a step between measurements of 200 Hz. At each frequency, the generated voltage across the circuit was measured using the multimeter UT–81A, as shown in Figure 4.3. The multimeter had accuracy specifications as shown in Table 4-I. Finally, it is worth mentioning that only Cylinders (A) and (B) were considered in this measurement.

Taking into consideration the capacitive nature of the cylinder, it was believed that the harvesting behaviour of the transducer would depend on how many charges were already stored in the cylinder. To neutralize this effect, it was set that the measurement would be repeated three times. Before each measurement, the bridge terminals were connected to a short circuit using a 2 Ω resistor to dissipate any residual electric charges that might be already stored in the cylinder. This procedure shall be repeated in all the coming measurements involving acoustic waves.

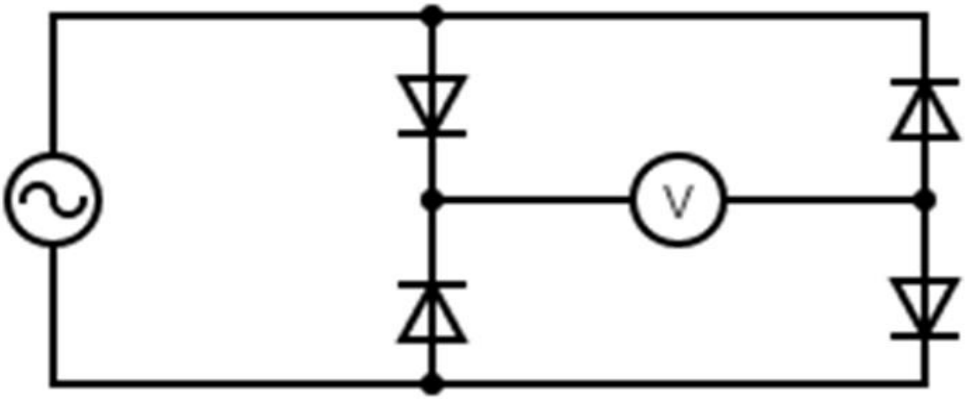

Figure 4.3 A schematic diagram of the circuit used in the open-circuit measurements, where the output voltage of the rectifier was measured via a multimeter.

Table 4-I UT–81A multimeter specifications

Parameter	Value	Error Margin (mV)
Number of vertical divisions	8	-
DC vertical gain accuracy	±0.8% reading	*Variable depends on the reading*
DC vertical offset accuracy	± 8 × least significant digit	±0.8

4.3.2 Results of open-circuit measurements:

4.3.2.1 Frequency-response:

Figure 4.4 shows the raw data of the voltage measured from the two cylinders. It can be noticed for both the cylinders that the voltage tended to generally increase with the increase in the sound frequency, achieving a maximum voltage at the top of the acoustic spectrum of 108.5 mV for Cylinder (A) and 44.3 mV for Cylinder (B). The difference in the voltage from the two cylinders is attributed to the difference in their surface area that collects the acoustic waves.

In the figure, it can also be noticed that several voltage peaks were formed for both cylinders. Cylinder (A) had a voltage peak at a frequency of 12.2 kHz. To investigate this peak, it was necessary to recall the data of the resonance frequencies presented in Table 2-II, where it can be noticed that this frequency corresponds to $F_{r_p}/4.07$, where $\mathrm{F_{r_p}}$ is the radial-mode resonance frequency of Cylinder (A).

In order to justify this peak, it was believed that the sound waves applied from the speakers with a frequency of 12.2 kHz would form other overtones with a harmonic number, *n*, equals 2–4. Such overtones would be sufficient to create vibrations in the cylinder with its resonance frequency, F_{r_p}. Moreover, a similar behaviour could be expected at the sound frequency $F_{r_p}/8$, where the eighth overtones of such waves could be able to achieve vibrations with the natural frequency. To furtherly investigate this observation, dashed red lines are plotted in Figure 4.4 at each of the frequencies representing $F_{r_p}/4$ and $F_{r_p}/8$. However, no peak in the voltage was found at the frequency $F_{r_p}/8$.

In the same figure, it can be seen that Cylinder (B) had its peak voltage at a frequency of 12.4 kHz. Following the procedure followed for Cylinder (A), this frequency is referenced to the radial-mode resonance frequency of Cylinder (B) and was found to represent 1/7.85 of the cylinder resonance frequency F_{r_p}, blue dashed line. Similar to Cylinder (A), it was not possible to find a peak at half of this frequency, 6.2 kHz, which represents 1/(7.85 × 2) F_{r_p}

for Cylinder (B), blue dashed line. Finally, the two cylinders shared a peak at a frequency of 9 kHz.

In addition to the mentioned peaks, the voltage from the two cylinders tended to increase, starting from the frequency 16 kHz up to the end of the acoustic range. It is possible that this rise is attributed to the left side of a peak that is centred around a frequency of 24.375 kHz, lying outside of the acoustic range. Such a frequency would represent 1/2 and 1/4 of the F_{r_p} of the Cylinders (A) and (B), respectively—Table 2-II shows that the F_{r_p} of Cylinders (A) and (B) are 48.75 and 97.5 kHz, respectively—Unfortunately, it was not possible to expand this measurement outside of the acoustic range to verify this hypothesis since the used speakers were rated up to 20 kHz only.

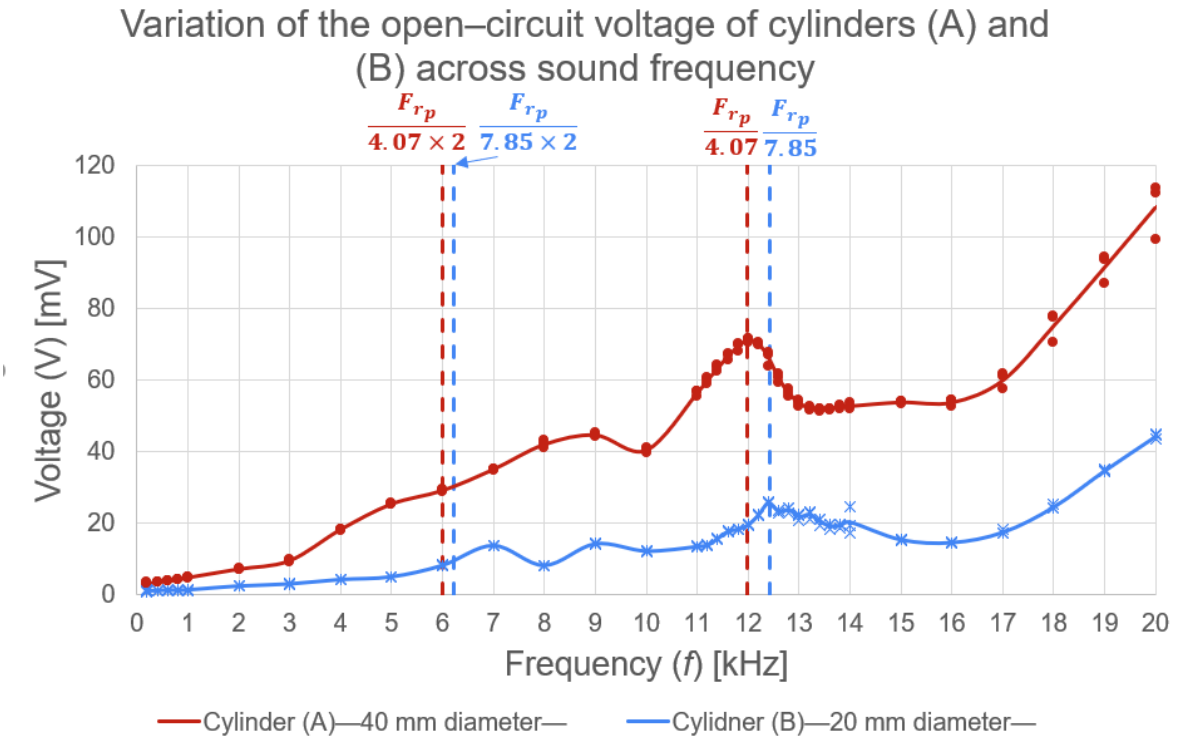

Figure 4.4 Variations in the open-circuit voltage from acoustic waves with the sound frequency for Cylinders (A) and (B).

4.3.2.2 The effect of cylinder size:

To investigate the potential relationship between the cylinder size and the frequency of the harvested sound waves, the data from Cylinder (A) was replotted in Figure 4.5 using a dimensionless frequency, f^{o}. This dimensionless number was defined as the ratio between the cylinder diameter D_{cyl} and the sound wavelength λ as shown in equation (4.1), where f is the sound frequency, and a is the sound speed in air taken to be 343 m/s. Moreover, this figure plots the data with respect to the error margins defined in Table 4-I.

$$f^{o} = \frac{D_{cyl}}{\lambda} = \frac{D_{cyl}}{\frac{a}{f}} = \frac{D_{cyl}\, f}{a} \tag{4.1}$$

By representing the data using the new dimensionless parameter, it was possible to divide Figure 4.5 into two parts separated by a green separation line at $f^{o} = 1$. The part on the left of the separation line represents the case when the cylinder diameter was less than the sound wavelength, and the part on the right of the separation line represents the case when the cylinder diameter was greater than the sound wavelength.

It can be noticed that the voltage tended to increase in the left part with increasing frequency up until the separation line exactly. On the other hand, the trend in the right part was different. By examining the right part, one would find that it was composed of four main sections: a, b, c, and d. Section (a) extended over the range of $f^{o} = 1$–1.16, where the voltage tended to drop with increasing frequency. Then, Section (b)—the aforementioned peak—extended over the range $f^{o} = 1.17$–1.52. Then, Section (c) extended over $f^{o} = 1.52$–1.87, where the voltage was almost constant. Then, Section (d), where the voltage tended to increase with increasing frequency, forming what is thought to be a peak centred at $F_{rp}/2$ outside of the acoustic range.

The difference in the trends of the two halves may be attributed to the relation between the sound wavelength and the cylinder size. In the left half, where the sound wavelength was larger than the cylinder diameter, the sound waves tended to diffract off the cylinder without transporting their energy into the cylinder. In other words, the cylinder was not able to well capture the mechanical energy of sound waves of large wavelength and small frequency. As the frequency increased and the wavelength decreased, the sound waves gradually lost their ability to diffract off the cylinder, and more energy was transferred from the acoustic waves to the cylinder. This may justify the direct proportionality between the generated voltage and sound frequency in the left half.

When the sound wavelength reached a critical value that was equal to the cylinder diameter, acoustic waves were no longer able to diffract and were rather either absorbed or reflected off the cylinder. In such a case, energy transfer between the waves and the cylinder depended only on the difference between the acoustic impedance of the two media—the cylinder and the air. Therefore, it would be expected that the right half of the scale would have a constant voltage level, which agrees with the obtained data—ignoring Sections (b) and (d), since they are altered by the resonance of the cylinder. However, the drop in voltage in Section (a) remains unjustified.

It is important to take into consideration the margins of measurement error. Considering the error margins plotted in the figure, it is possible that Section (a) had a constant voltage rather than a voltage drop. It could even have just a declined rate of voltage growth compared to Section (b) rather than a voltage drop.

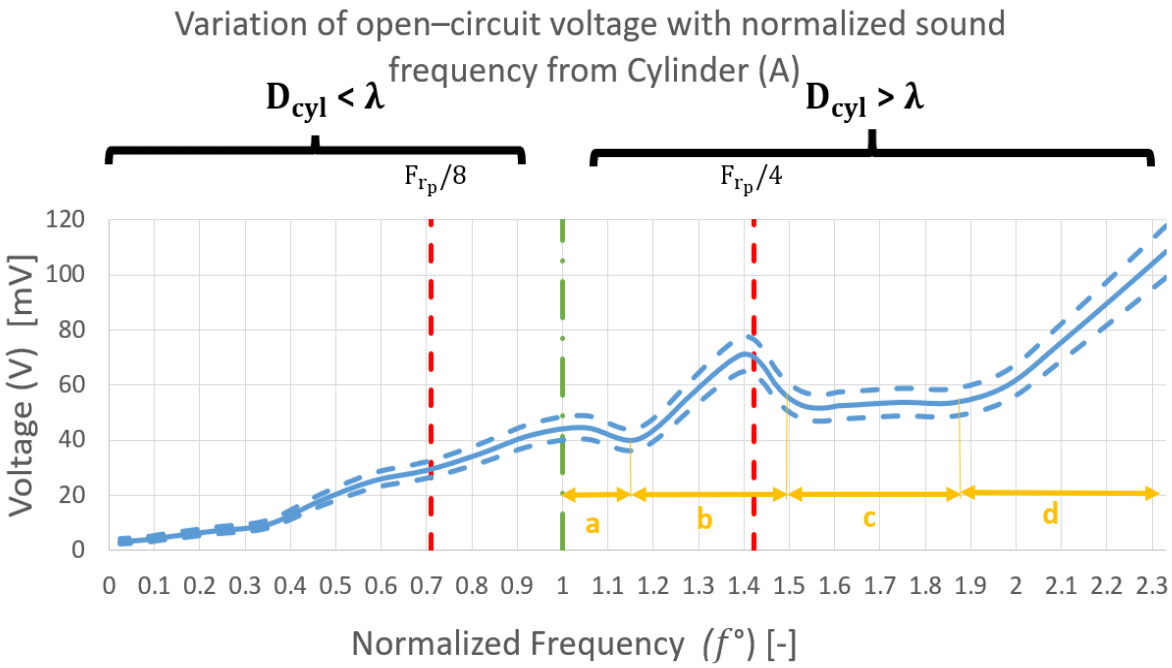

Figure 4.5 Variations in the open-circuit voltage of Cylinder (A) generated by Acoustic Energy Harvesting, AEH, across the normalized frequency, f^o. Dashed blue lines represent the upper and lower limits of the error margin.

Figure 4.6 shows the data of Cylinder (B) presented before, however, plotted versus the normalized frequency defined in equation (4.1). From the figure, it can be seen that the green separation line for this cylinder was at a frequency of 17.15 kHz, with the rise to the right of the line being attributed to a peak at a frequency of 24.375 kHz as was discussed previously. Unfortunately, it would not be possible to see the effect of the cylinder size since the green line is situated at the upper end of the acoustic frequency range, and the remaining part of the acoustic range, frequency 17.15 up to 20 kHz, is affected by the resonance peak. In order to check the hypothesis on the effect of the cylinder size presented above, it would be necessary to either use ultrasonic waves or to use cylinders bigger than Cylinder (A).

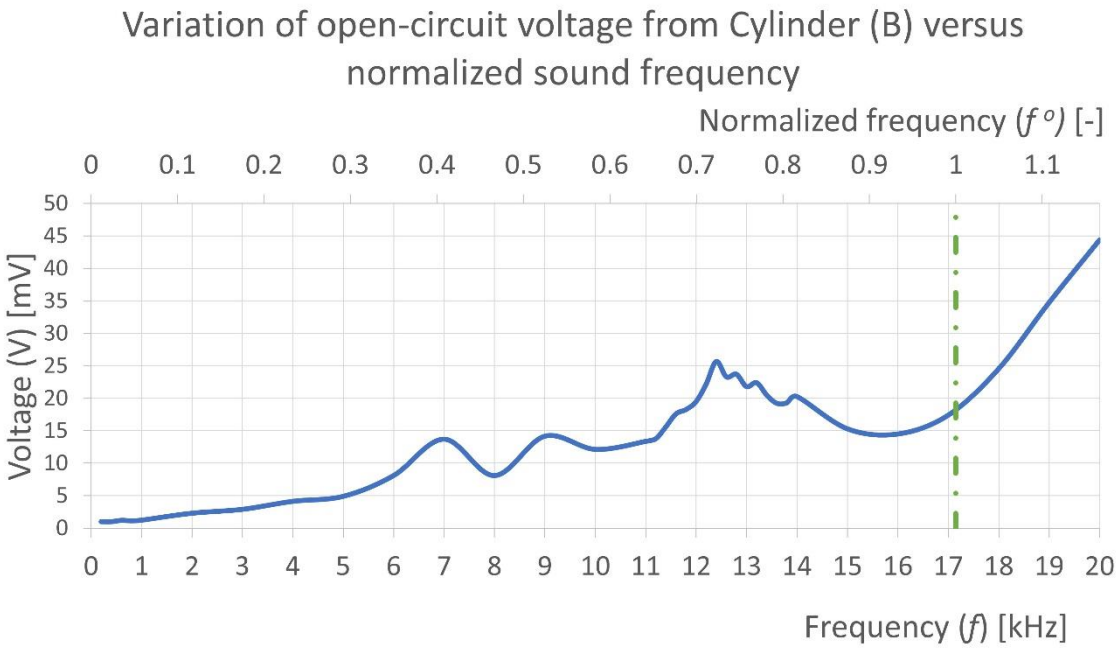

Figure 4.6 Variations in the open-circuit voltage of Cylinder (B) generated by Acoustic Energy Harvesting, AEH, across both frequency and normalized frequency, f^o.

4.3.3 Conclusion:

From the open-circuit measurement, it was found that the two cylinders—A and B—have given the highest open-circuit voltage among the acoustic frequency spectrum at a frequency of 20 kHz. Therefore, the design frequency shall be considered to be 20 kHz in the next stage. Moreover, since Cylinder (A) has given a higher open-circuit voltage than Cylinder (B), only Cylinder (A) will be used in the next stages.

4.4 Closed-circuit Measurements:

In Phase (2), an energy harvester is constructed respecting the maximum power transfer theorem. According to this theorem, a power source will transfer to its load a maximum amount of power when the source and the load are of conjugated impedances, i.e., matched impedance [56]. The harvester was optimized for sound waves with a frequency of 20 kHz, which were found to provide the best performance in Phase 1.

Thanks to the impedance measurements presented in Section 3.3.2, the impedance of Cylinder (A) at a frequency of 20 kHz is known to be 1.93 − 50.7*j* Ω. Therefore, the load can be designed using equations ((4.2)–(4.4)) to have an electric impedance of 1.93 + 50.7*j* Ω, where Z_t, *R*, Z_L, and Z_c refer to the total series impedance, the resistor, the impedance of an inductor, and a capacitor, respectively, while *f, L,* and *C* refer to the signal frequency, the inductance of the inductor, and the capacitance of the capacitor, respectively. To achieve impedance matching, it was set to use a resistor of value 2 Ω in the load. However, the setting of the values of the inductor and the capacitor needed special consideration to the frequency of the signal flowing in them.

$$Z_t = R + (Z_l - Z_c)\, j \tag{4.2}$$

$$Z_L = 2\,\Pi\, f\, L \tag{4.3}$$

$$Z_c = \frac{1}{2\,\Pi\, f\, C} \tag{4.4}$$

Since the output signal of the source circuit has been through a full-wave rectifier bridge, the signal is expected to be ideally of a frequency that is double the sound frequency, as explained in Figure 4.7. However, it was clear from the patterns obtained from the oscilloscope during the open-circuit measurements that the rectification did not occur with 100% efficiency. So, it was not clear which frequency to consider: 20 or 40 kHz. Such ambiguity makes defining the inductance and the capacitance values complicated since their impedance depends mainly on the frequency of the signal flowing in the load.

To solve this question, the problem was divided into two steps: Case (1) and Case (2). In Case (1), measurements were performed to set the design frequency that impedance matching shall consider. Then in Case (2), measurements were performed to find the best load circuit configuration.

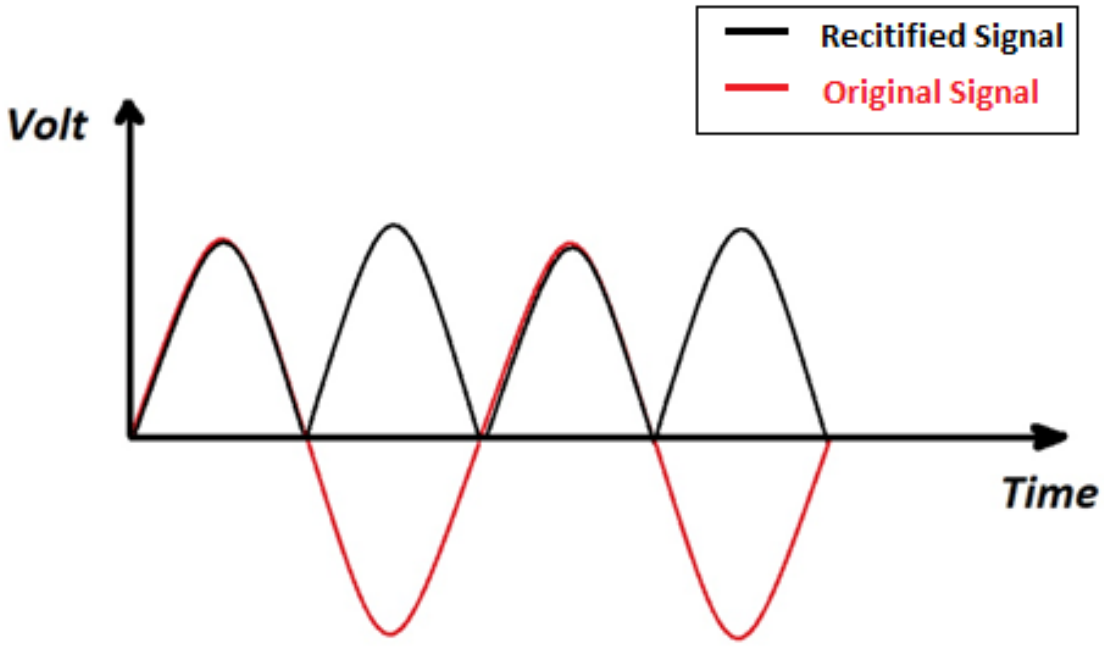

Figure 4.7 Signal rectification via a full-bridge rectifier. Red: the original signal, Black: the rectified signal.

4.4.1 Case (1):

4.4.1.1 Methods:

In this step, two designs of the load were considered. The load in each case was composed of the 2 Ω resistor, an inductor, and a capacitor. Design (1A) was to achieve impedance matching considering a sound frequency of 20 kHz, while Design (1B) considered a frequency of 40 kHz. The objective of the measurement shall be to find which configuration would harvest more power.

Since the influence of an inductor on the total value of impedance is more than the capacitor's, according to equations ((4.2))–(4.4)), it was decided to vary the inductance value while keeping the capacitance constant at a value of 220 μF. Hence, it was possible to choose an inductance value of 440 µH for Case (1A) and 220 µH for Case (1B) using equations ((4.2)–(4.4)). Table 4-II summarizes the details of the two circuits, while Figure 4.8 and Figure 4.9 show the schematic diagrams for circuits of Cases (1A) and (1B), respectively.

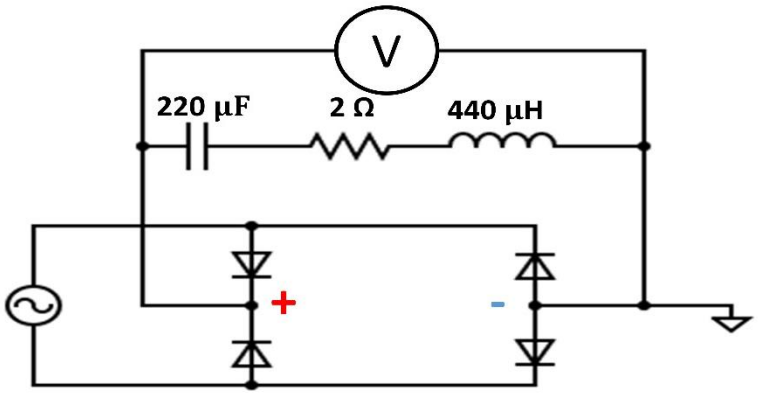

Figure 4.8 Schematic diagram for load case (1A).

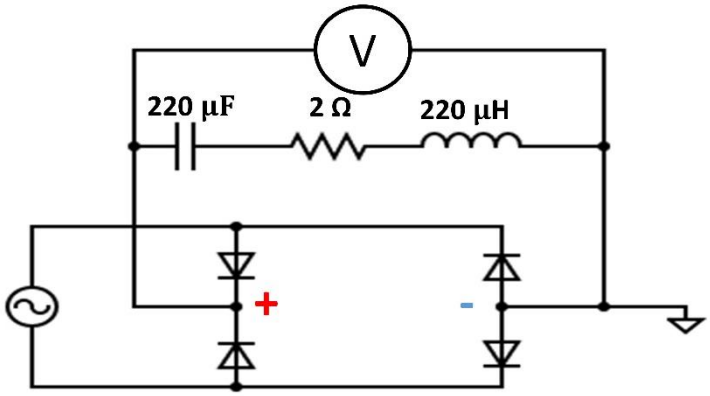

Figure 4.9 Schematic diagram for load case (1B).

For each load case, sound waves of frequency 20 kHz were applied on the cylinder using the same set-up described for the open-circuit measurement in Section 4.2 while measuring the generated voltage across the load, the R–L–C branch. The measurement was performed until the measured voltage flattened over time, i.e. the capacitor was full as much as possible. Unfortunately, it was not possible to measure the flowing electric current as it was very weak compared to the oscilloscope resolution. Therefore, the electric power, *P*, dissipated in the load was determined using equation (4.5).

$$P = \frac{V^2}{|Z_t|} = \frac{V^2}{\sqrt{R^2 + (Z_L - Z_c)^2}} \tag{4.5}$$

Table 4-II Summary of the electric impedance applied in the different circuits of Case (1).

Circuit	Flowing Signal Frequency [kHz]	Used Inductor [µH]	Total Impedance [Ω]
Source Circuit	20	-	1.93 – 50.7 *j*
Load Circuit Case (1A)	20	440	2 + 55.25 j
Load Circuit Case (1B)	40	220	2 + 55.23 j

4.4.1.2 Results of Case (1):

Figure 4.10 shows the voltage generated over time in both Cases (1A) and (1B). From Figure 4.10, it can be noticed that it took thirteen minutes to reach the steady-state voltage across the load. Moreover, it was noticed that Case (1A) achieved a high steady-state value of 115.6 mV. Regarding power, Figure 4.11 shows the power generated in the two cases, where 224 µW of power was harvested by the circuit of Case (1A), while only 116 µW of power was harvested by the circuit of Case (1B). Therefore, it is evident that Case (1A)—the case that considered that the frequency was not doubled inside the rectifier—was the better configuration. Hence, the design frequency shall be 20 kHz in the following stages.

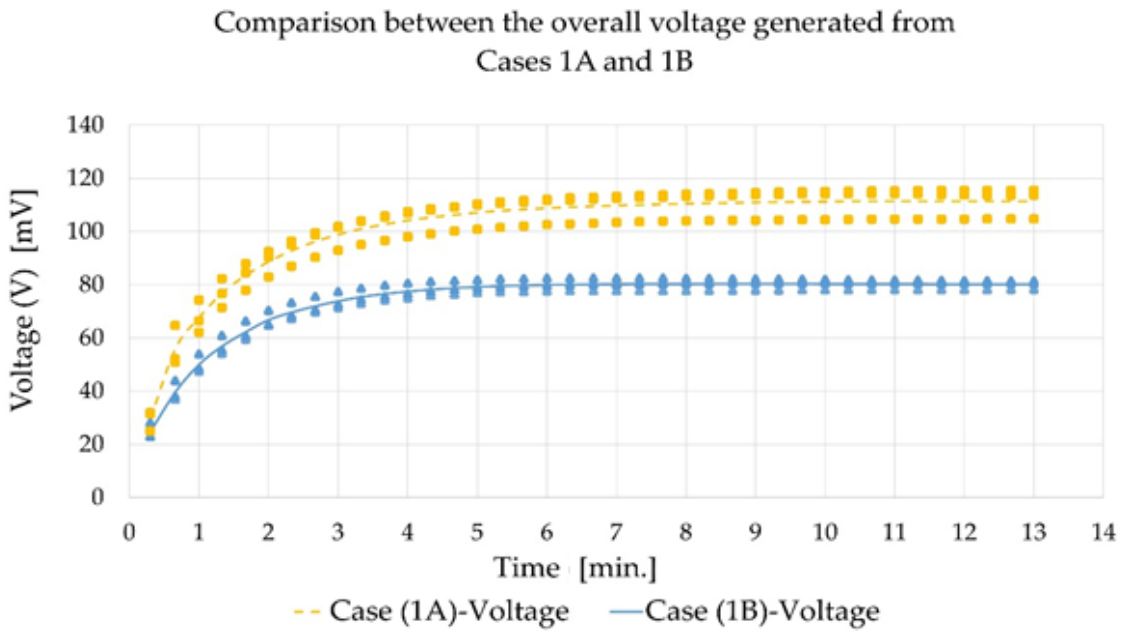

Figure 4.10 A comparison between the overall voltage generated in Case (1A) and Case (1B) of closed-circuit acoustic energy harvesting using Cylinder (A).

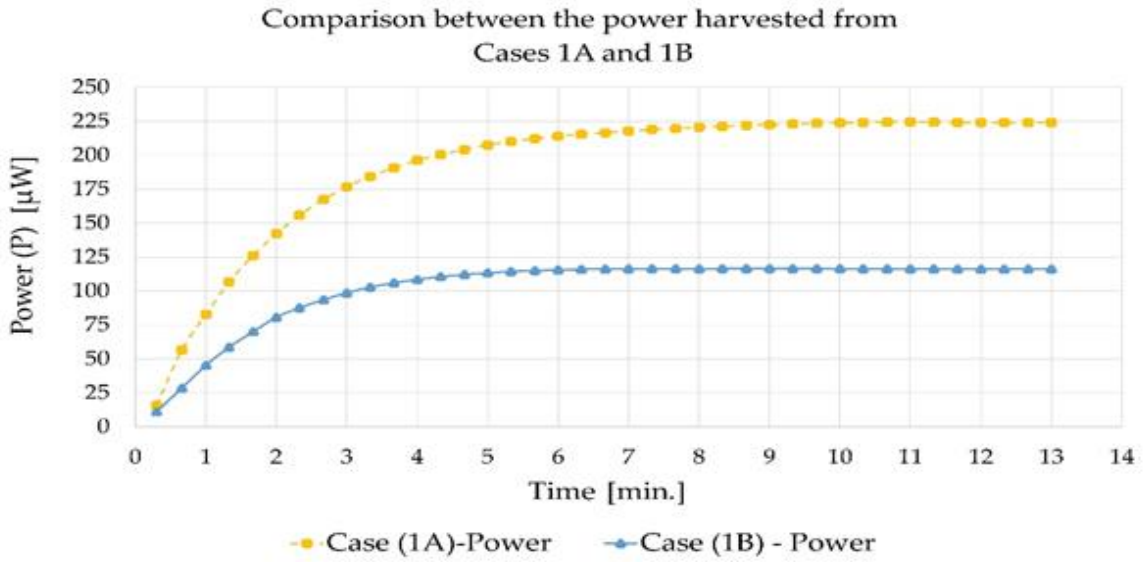

Figure 4.11 A comparison between the power harvested in Case (1A) and Case (1B) of closed-circuit acoustic energy harvesting using Cylinder (A).

4.4.2 Case (2):

4.4.2.1 Methods:

4.4.2.1.1 The electric measurement:

After defining the design frequency in Case (1), measurements of Case (2) were designed such that the capacitor value was varied while fixing the inductance value. This was performed to show the effect of impedance matching on harvesting performance. Three different values of capacitance—2, 10, and 1 µF—were chosen using equations ((4.2)–(4.4)) to achieve balanced impedance across the whole circuit. The data of the impedance values are summarized in Table 4-III. Moreover, at this phase, it would be interesting to look at the efficiency of energy harvesting. Therefore, it would be necessary to quantify the acoustic power involved in the measurements as well as the harvested electric power.

Table 4-III Summary of electrical impedance of the load circuits used in Case (2) of closed-circuit acoustic energy harvesting using Cylinder (A).

Used Load Capacitor [µF]	Load Impedance [Ω]	Ratio of the Source's Impedance Magnitude to the Load's [-]
2	2 + 51.3 j	0.988
10	2 + 54.49 j	0.933
1	2 + 47.37 j	1.071

After constructing the circuit as discussed above, the experiment was conducted using the same procedure that was followed in Case (1), where sound waves with a frequency of 20 kHz were applied to the cylinder, while the electric power was calculated using equation (4.5).

It is worth mentioning that all electric measurements were performed across the output terminals of the full-wave rectifier. This means that it would take into account the losses in voltage caused by the bridge. To quantify these losses—and also to make sure that none of the diodes had burned out during a previous measurement—, the total forward voltage across the bridge terminals V_{loss} was always measured before each measurement using a voltmeter set to the diode measurement mode. It was found out that the bridge imposes a total drop in voltage of 0.432 Volts. This value shall be relevant later during the efficiency calculations.

4.4.2.1.2 The acoustic measurement:

The acoustic power was measured using a microphone. Using this measurement, it would be possible to calculate the efficiency of the harvesting process. However, there were practical complications regarding the measurement of sound power level, L_W, or sound intensity level, L_i, at such a high frequency. To overcome this problem, it was focused on the near-field sound since the numerical value of the sound pressure level, SPL, was equal to that of the intensity level, L_i , to that of the velocity level, L_v. Hence, by measuring the sound pressure level in the near field, it would be possible to quantify the intensity, I, using equation (4.6) and, hence, the total amount of power incident on the cylinder using equation (4.7). In equation (4.6), I_{ref} is taken to be 10^{-12} W/m^2 according to the sound intensity threshold required for human hearing, while in equation (4.7), D_{cyl} and L_{cyl} were taken to be 0.04 m, for Cylinder (A).

$$I = 10^{(L_i/10)} \times I_{ref} \tag{4.6}$$

$$P_{acoustic} = I \times A_{cyl} = I \times \pi D_{cyl} L_{cyl} \tag{4.7}$$

4.4.2.2 Results of Case (2):

4.4.2.2.1 Results of the electric measurement:

Figure 4.12 shows the developed voltage across the load circuit over time in the case of using different capacitors, while Figure 4.13 shows the dissipated power in the load for each case. It was found that the load circuit with the 10 μF capacitor achieved the highest steady-state voltage. However, the circuit with the 1 μF capacitor dissipated the most power. This agrees with the data shown in Table 4-III, where it was expected that the circuit with the 1 μF capacitor would dissipate the most power since it had the best impedance match among the three circuits.

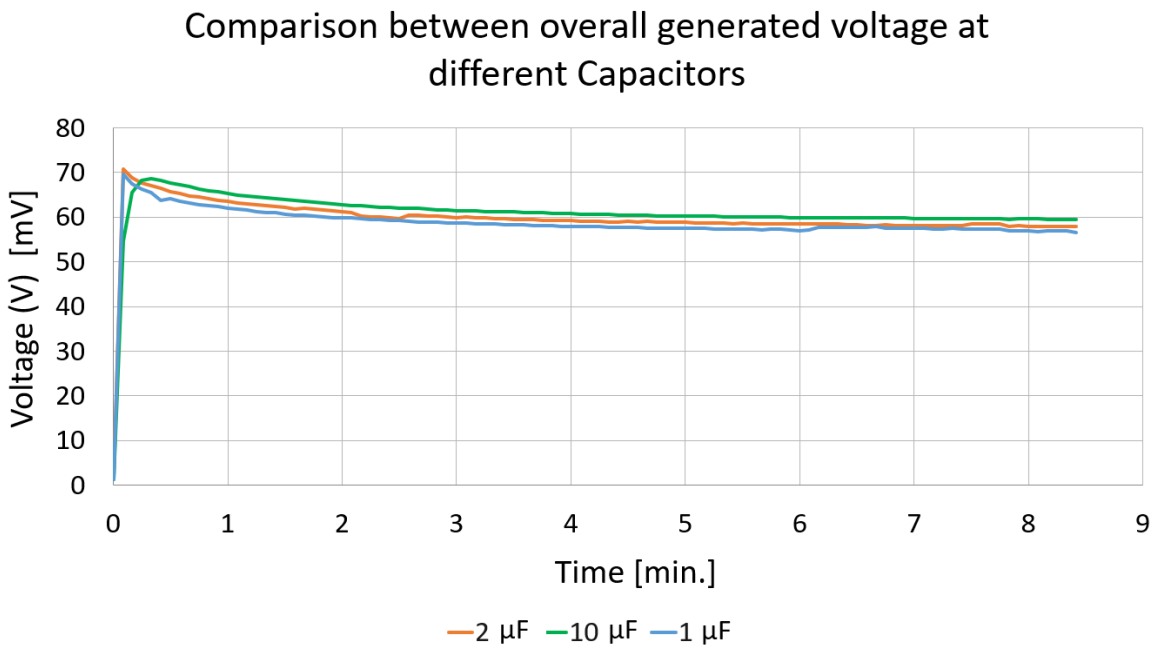

Figure 4.12 A comparison between the overall voltages generated using different capacitors in Case (2) of closed-circuit acoustic energy harvesting using Cylinder (A).

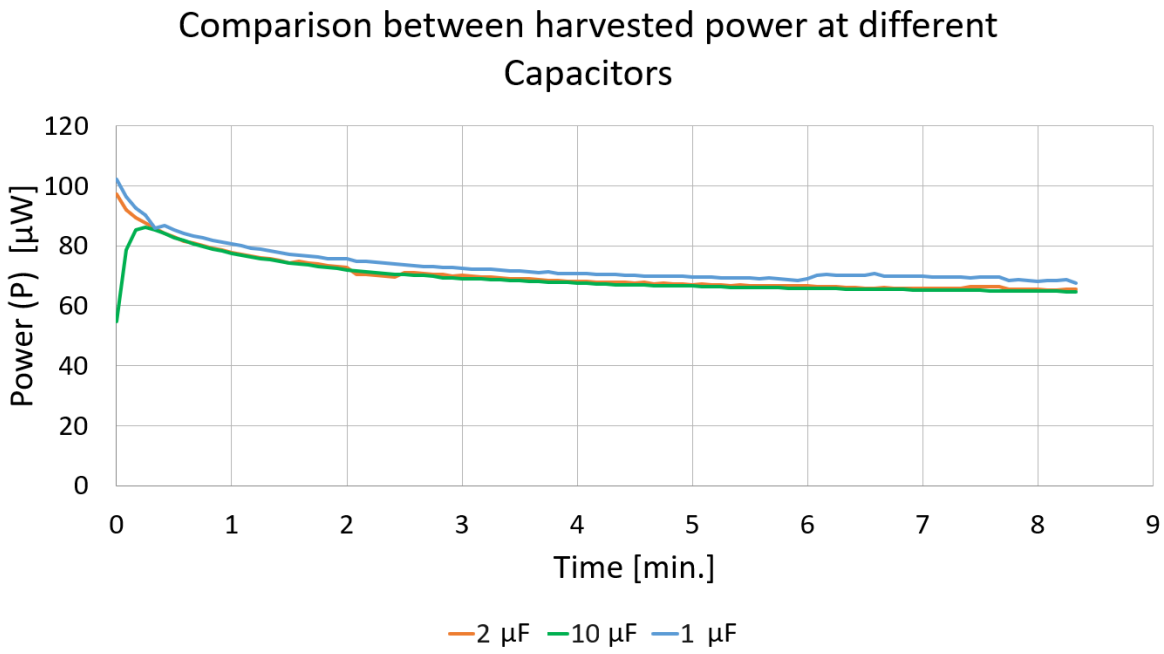

Figure 4.13 A comparison between the overall power dissipated across different capacitors in Case (2) of closed-circuit acoustic energy harvesting using Cylinder (A).

4.4.2.2.2 Results of the acoustic measurement:

Figure 4.14 shows the the Fast Fourier transform, FFT, of the sound pressure level, where the 20 kHz component pressure level was 102.5 dB. Using equations (4.6) and (4.7), it would be possible to calculate the total acoustic power collected by the cylinder to be 78.5 μW.

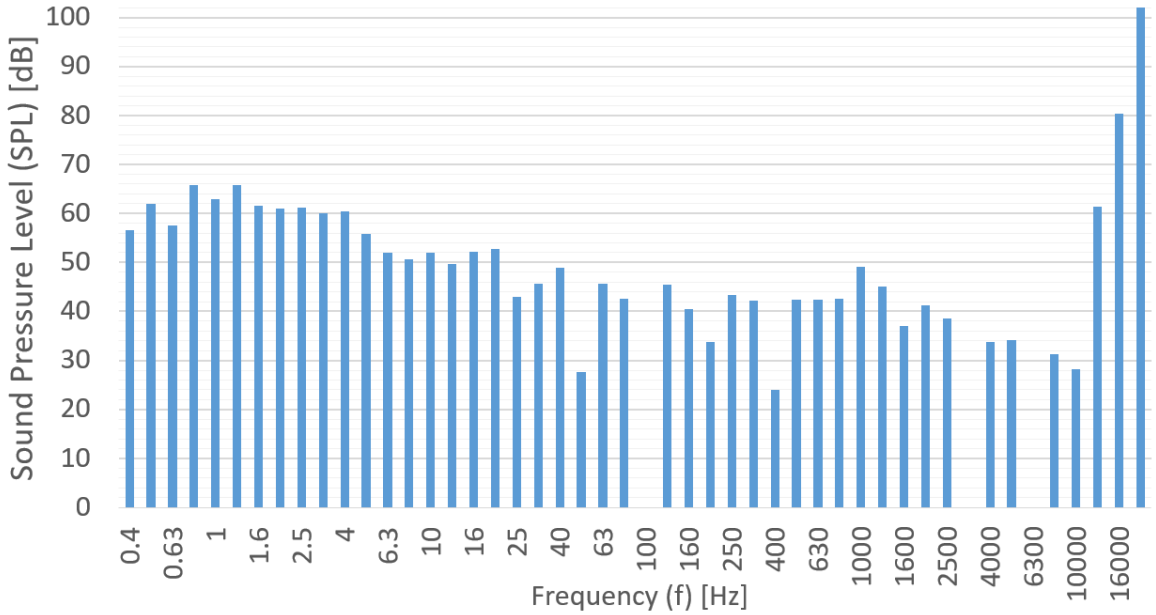

Figure 4.14 Fast Fourier transform, FFT, of the sound pressure level in Case (2) of closed-circuit measurement of acoustic energy harvesting.

4.4.2.2.3 The efficiency of energy harvesting:

To evaluate the performance of the energy harvester by Cylinder (A), it was possible to use equations (4.8) and (4.9) to calculate the harvesting efficiency, η, and energy harvesting density, ρ, respectively, where P is the harvested electric power calculated in equation 4.5). The results obtained from the data of the three capacitor cases are summarized in Table 4-IV, where it was found that the optimized harvester with the capacitor of 1 μF has achieved a harvesting efficiency of 86.1% with an energy-harvesting density of 1.3455 μW per unit squared centimeter of the cylinder's surface area.

$$\eta = \frac{P}{P_{acoustic}} \tag{4.8}$$

$$\rho = \frac{P}{A_{cyl}} = \frac{P}{\Pi D_{cyl} L_{cyl}} \tag{4.9}$$

4.4.2.2.4 Estimation of the Energy rectification Efficiency:

To evaluate the voltage drop imposed by the electric circuit, equation (4.10) was devised to calculate the voltage rectification efficiency, η_v , where V is the steady-state voltage across the load, and V_{loss} is the voltage drop across the bridge. As was mentioned previously in Section 2.3.2, the full-wave rectifier bridge imposed a total voltage drop, V_{loss}, of 432 mV. Therefore, it would be possible to calculate η_v for the different load circuits as summarized in Table 4-IV. It is worth mentioning that the voltage rectification efficiency depended mainly on the forward-voltage drop of the used diodes and the steady-state voltage generated by the cylinder. The steady-state voltage itself was related—via the voltage constant of the piezoelectric material—to the mechanical pressure applied to the harvester. In applications of acoustic energy harvesting, the magnitude of the pressure of the involved vibrations is relatively small. Therefore, the generated steady-state voltage will also be small, lowering the value of the voltage rectification efficiency.

$$\eta_v = \frac{V}{V + V_{loss}} \tag{4.10}$$

Table 4-IV Evaluation of acoustic energy harvesting in Case (2) of closed-circuit acoustic energy harvesting using Cylinder (A).

Used Load Capacitor C [µF]	**Steady-State Voltage V [mV]**	**Steady-State Power P [µW]**	**Harvesting Density ρ ($[\frac{\mu W}{cm^2}]$**	**Harvesting Efficiency η [-]**	**Voltage Rectification Efficiency [-]**
2	57.65	64.72	1.2882	82.4%	11.77%
10	59.3	64.4	1.2818	82%	12.07%
1	56.6	67.6	1.3455	86.1%	11.58%

4.5 Discussion:

4.5.1 Effect of the size and the geometry of the transducer on the energy harvesting process:

Based on the results obtained from the open-circuit measurements performed at different frequencies, it can be concluded that there is a critical sound frequency above which acoustic energy harvesting by a cylindrical transducer is improved. This frequency is related to a property of sound waves, which is sound diffraction. Such a property would not be relevant in the case of other geometries such as plate–shaped, ring–shaped or bending element transducers.

This critical frequency was based on the relationship between the corresponding sound wavelength and the diameter of the cylinder. By studying equation (4.1), it can be concluded that the bigger the cylinder is, the smaller this critical sound frequency. In other words, the cylinder will have a wider frequency range over which its harvesting performance is improved.

4.5.2 Evaluation of the complete energy harvester

It has been practically demonstrated that these piezoelectric cylinders can be used to harvest and store acoustic energy at a frequency of 20 kHz. The cylinder was able to harvest 67.6 μW of acoustic energy with an efficiency of 86.1% and an energy-harvesting density of 1.3455 $\mu W/cm^2$. In order to compare this piezoelectric cylinder to the other harvesters, the evaluation method set by the authors in [58] was used, where they calculated the *Metric* parameter defined in equation (1.12) for various harvesters reported in the literature. By applying equation (1.12) to the piezoelectric cylinder proposed in this paper, it turns out that Cylinder (A) has achieved a *Metric* of 0.2152, which outperformed 16 out of the 17 designs on their list. In the following section, some of the interesting designs that share some of the working conditions of the piezoelectric cylinder highlighted for a more in–depth comparison. A summary of the data on these harvesters can be found in Table 4-V.

The design presented by Khan et al. [73] had a *Metric* score of 14.536 $\mu W/(cm^3.Pa^2)$, and it was the only design with a *Metric* that was higher than that of the piezoelectric cylinder; it is based on electromagnetic transduction rather than piezoelectric. It harvests acoustic energy using a set of composed wound coils mounted on a thin membrane, a permanent magnet, and a Helmholtz resonator. Energy harvesting starts when the acoustic waves make the air particles vibrate inside the Helmholtz resonator. Because of the resonation mechanism of the resonator, the vibration of the air particles inside the resonator neck are amplified, which in turn, induces vibrations in the thin membrane causing motion of the

coil. Then, the induced motion of the coil relative to the permanent magnet eventually generates electric energy. The design managed to provide a voltage of 198.7 mV over a load of 50 Ω. This means it harvested 789.6 μW of electric power. The input sound waves were of a frequency of 319 Hz—the resonance frequency of this harvester—and an SPL of 100 dB, which is quite similar to the SPL used in the experiment performed on the piezoelectric cylinder. By comparing the operating conditions of this harvester to the operating conditions of the piezoelectric cylinder, it can be noticed that the two harvesters shared the same operating sound pressure. However, the electromagnetic harvester was operating at its resonance frequency, while the cylinder was operating at a frequency near to half of its resonance frequency, where the resonance frequency lies outside of the acoustic range.

Among the designs in the list in [58] was the harvester proposed by Horowitz et al. in [74]. Their harvester is a micro-machined acoustic energy harvester that uses a Helmholtz resonator to amplify the sound pressure. The harvester uses a silicon wafer as a diaphragm and a ring-shaped PZT as a piezoelectric material. They were able to harvest 6×10^{-6} μW with the harvester at the resonance frequency of 13.57 kHz from sound waves of SPL of 149 dB. This design had the highest operating sound frequency in the list, where it presented 67.8% of the sound frequency used by the piezoelectric cylinder understudy in this research. Yet, the cylinder outperformed this design as can be seen by the *Metric* number, where this design achieved a Metric of 7.7228×10^{-12}.

Another design that was mentioned in the same comparison was the design reported by Li et al. [75]. This energy harvester is based on a quarter-wavelength straight tube resonator and multiple piezoelectric cantilever plates placed in the first half of the tube. This harvester was able to harvest remarkably high electric power—it was the highest in the list—where it generated 12,697 μW of power at an SPL of 110 dB and a frequency of 199 Hz. This high power was harvested by a relatively compact harvester, where it scored a Metric value of 0.187. It would be difficult to compare this design to the cylinder since they were designed for two very different sound frequencies—199 Hz versus 20 kHz. However, if the cylinder is to be coupled with other harvesters and a resonator, it can have the potential to harvest more energy even at smaller sound frequencies.

Table 4-V A comparison between acoustic energy harvesting by Cylinder (A) and other harvesters reported in the literature.

Harvester	**Concept of Transducer**	**Incident SPL** $[\mathbf{dB}]$	**Sound Frequency *f*** $[\mathbf{kHz}]$	**Power Output P** $[\mu\mathbf{W}]$	**Metric** $[\mu\mathbf{W}/(\mathbf{cm^3}.\mathbf{Pa^2})]$
Piezoelectric cylinder	Piezoelectric	101	20	67.6	0.2152
[73]	Electro-magnetic	100	0.319 (resonance condition)	789.6	14.536
[74]	Piezoelectric with a Helm-Holtz resonator	149	13.57 (resonance condition)	6×10^{-6}	7.7228×10^{-12}
[75]	Multiple piezoelectric cantilever plates with a quarter-wavelength straight tube resonator	110	0.199	12,697	0.187

5 Broadband Energy Harvesting (FIV):

5.1 Concept:

As was previously mentioned in Section 1.4, a body submerged in a flow shall undergo vibration of frequency f_s due to vortex shedding off the body, where the regime of these vortices is governed by the Reynolds number of the flow. The measurements described in this chapter were designed to look at the interaction of cylinders of a piezoelectric ability with a vortices-containing flow. Different diameters of the cylinders, together with different mainstream speeds *U* are used to achieve an array of various Reynolds number conditions versus cylinder diameters.

Following the procedure of the measurements of AEH, the investigation used open-circuit and closed-circuit measurements. In the open-circuit measurements, the characteristics of the generated voltage signals were studied and correlated to the models on vortex-shedding known from the literature. In the closed-circuit measurements, the performance of the cylinders as energy harvesters dissipating electric energy across an electric load shall be investigated. Contrary to loads involved in AEH, the loads from the airflow required a special fixture of the cylinders inside the wind tunnel. Such a fixture was expected to have its own effect on the measurements. Therefore, it was necessary to measure its natural frequency using free-vibration tests prior to the open-circuit forced-vibration tests.

5.2 Experiment Set-up:

The set-up was composed of a wind tunnel of the closed-circuit type. The wind tunnel has an operating wind speed in the range of 1–7 m/s. Inside the wind tunnel test section, a wooden beam was used as a mounting axis for the cylinders, as shown in Figure 5.1. The beam was clamped via two bench vises such that the cylinder axis was horizontal and perpendicular to the flow direction. The cylinder was mounted on the wooden beam by means of a sponge that was fitted between the inner surface of the cylinder and the wooden beam, as shown in Figure 5.2. Electric measurements were realized using the bench oscilloscope MSO-X 3054 A by Agilent Technologies with specifications as summarized in Table 5-I.

Table 5-I MSO-X 3054 A Oscilloscope accuracy settings.

Parameter	Value	Error Margin [mV]
Number of vertical divisions	10	-
DC vertical gain accuracy	±2.0% full scale	±2
DC vertical offset accuracy	±0.1 div ± 2 mV ± 1% of offset setting	±3

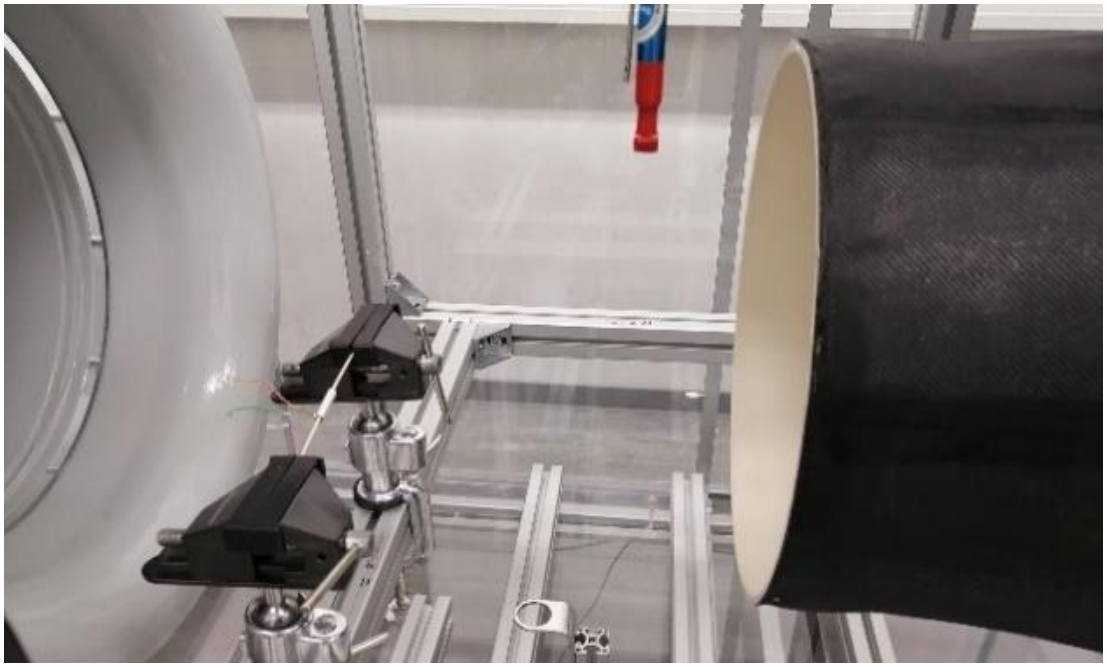

Figure 5.1 The cylinder is placed inside the tunnel test section perpendicular to the flow.

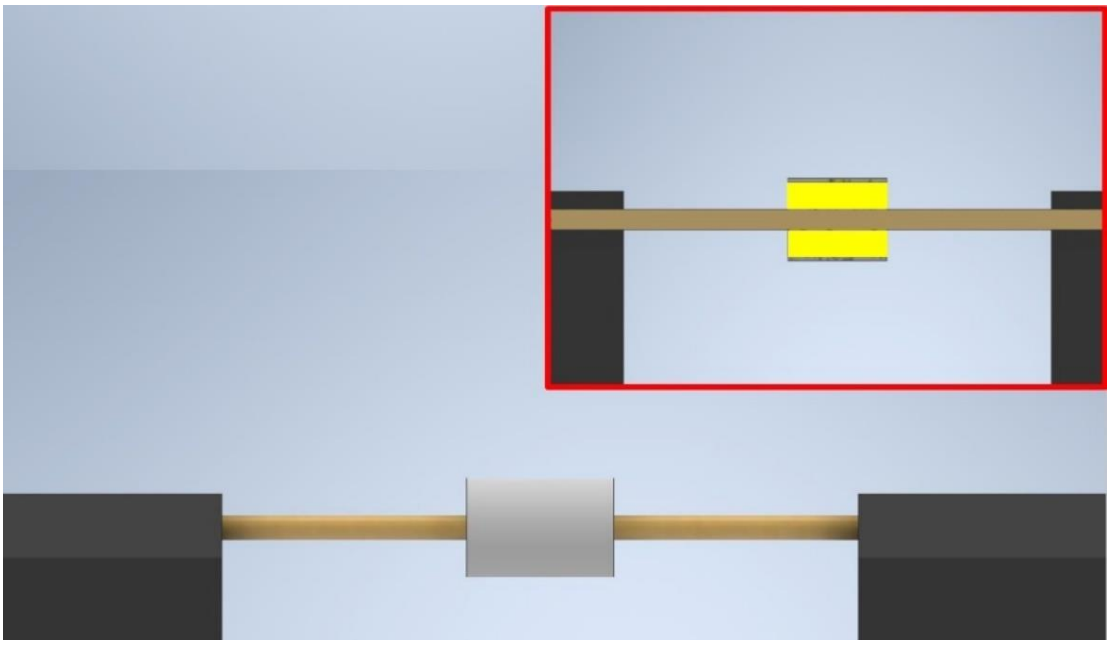

Figure 5.2 A 3D model of the fixation of the cylinder inside the wind tunnel test section.

5.3 Free-vibration Test of the Cylinder-support System.

In order to avoid any interference between the effect of the support–transducer characteristics and the process itself, it was necessary to define the natural frequency of the transducer together with its support. By doing so, it will be possible to identify if a certain behaviour is due to the fixation of the cylinder or if it is due to a different factor in the process. To identify the natural frequency of the system, free-vibration tests were performed for each cylinder–support system. It is worth mentioning that this measurement aims at finding the natural frequency of each system rather than comparing the signal amplitude of the different systems to each other.

Inside the wind tunnel, the cylinder was manually displaced downwards approximately one centimeter, as shown in Figure 5.3, while the generated voltage from the cylinder was measured using the oscilloscope. For convenience, the oscilloscope probes were connected to the cylinder poles in such a way that a positive signal was obtained in response to the compressive loads from the airflow. Unfortunately, it was not possible to set up a trigger. Therefore, a signal was recorded for five seconds, during which the cylinder was displaced manually.

Figure 5.4 and Figure 5.5 show the obtained time- and frequency-responses, respectively, for all the systems. The five strongest peaks for each system were chosen as the system characteristic peaks and are summarized in Table 5-II It can be noticed that a common frequency among the four cylinders was 50 Hz, which is believed to be due to the electric field radiation from the electrical outlets in the walls as well as the AC motor of the wind tunnel with its speed control systems.

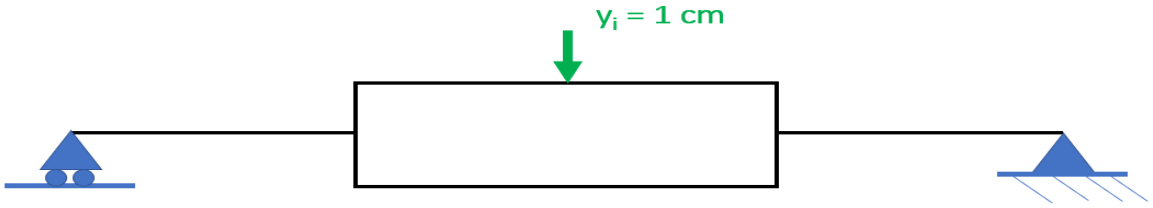

Figure 5.3 A schematic diagram of the cylinder–support system

Table 5-II Peak frequencies from the free-vibration tests of the cylinder–support systems, frequencies in Hz.

	Peak (1)	**Peak (2)**	**Peak (3)**	**Peak (4)**	**Peak (5)**
Cylinder (A)	7.45	12.7	24.5	50	53.58
Cylinder (B)	10.55	19	29.4	50	97.15
Cylinder (C)	5.9	13.4	22	35.1	50
Cylinder (D)	4.9	13	50	57	123.15

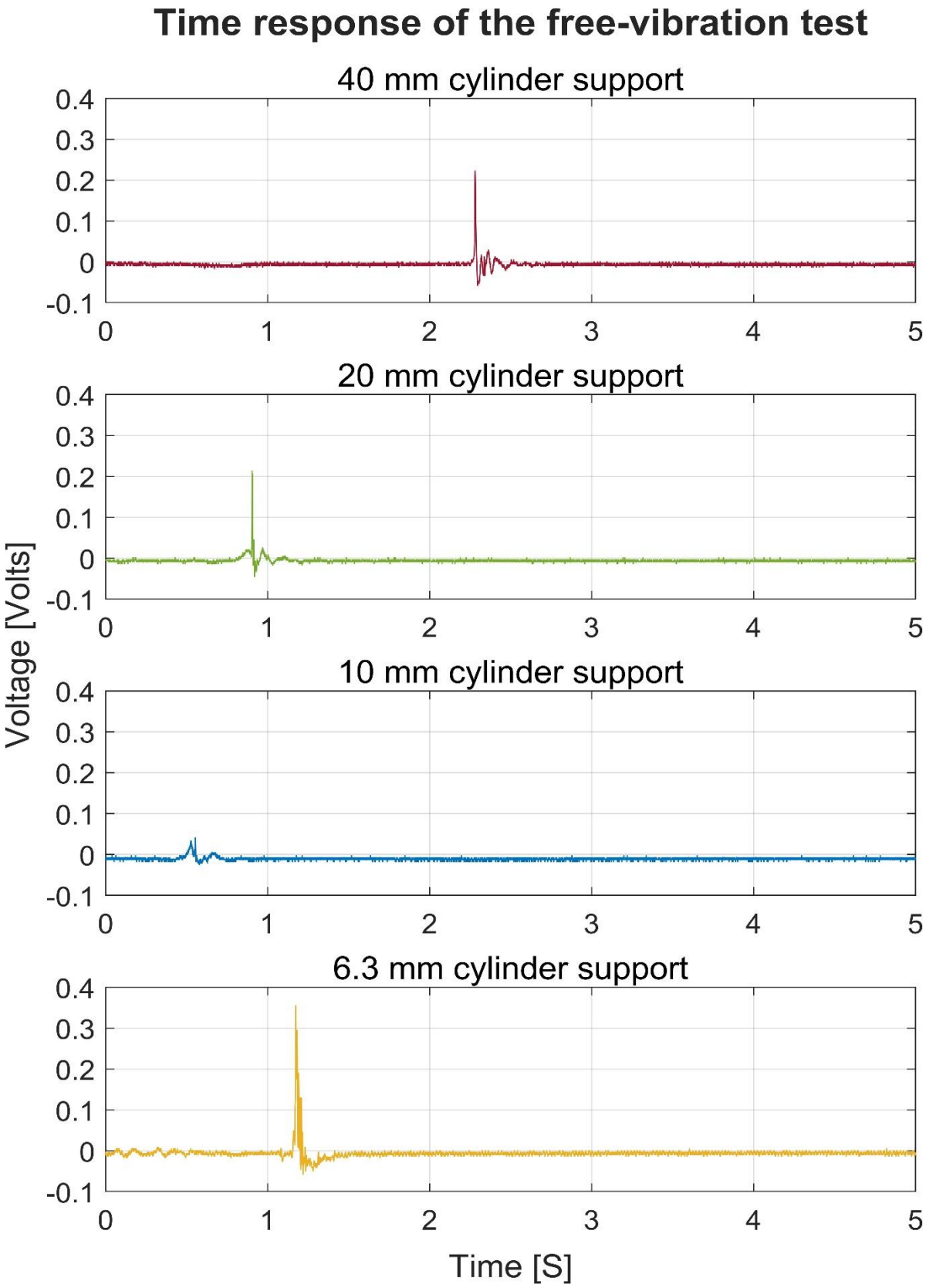

Figure 5.4 Time-response of the free-vibration test of the cylinder-support system.

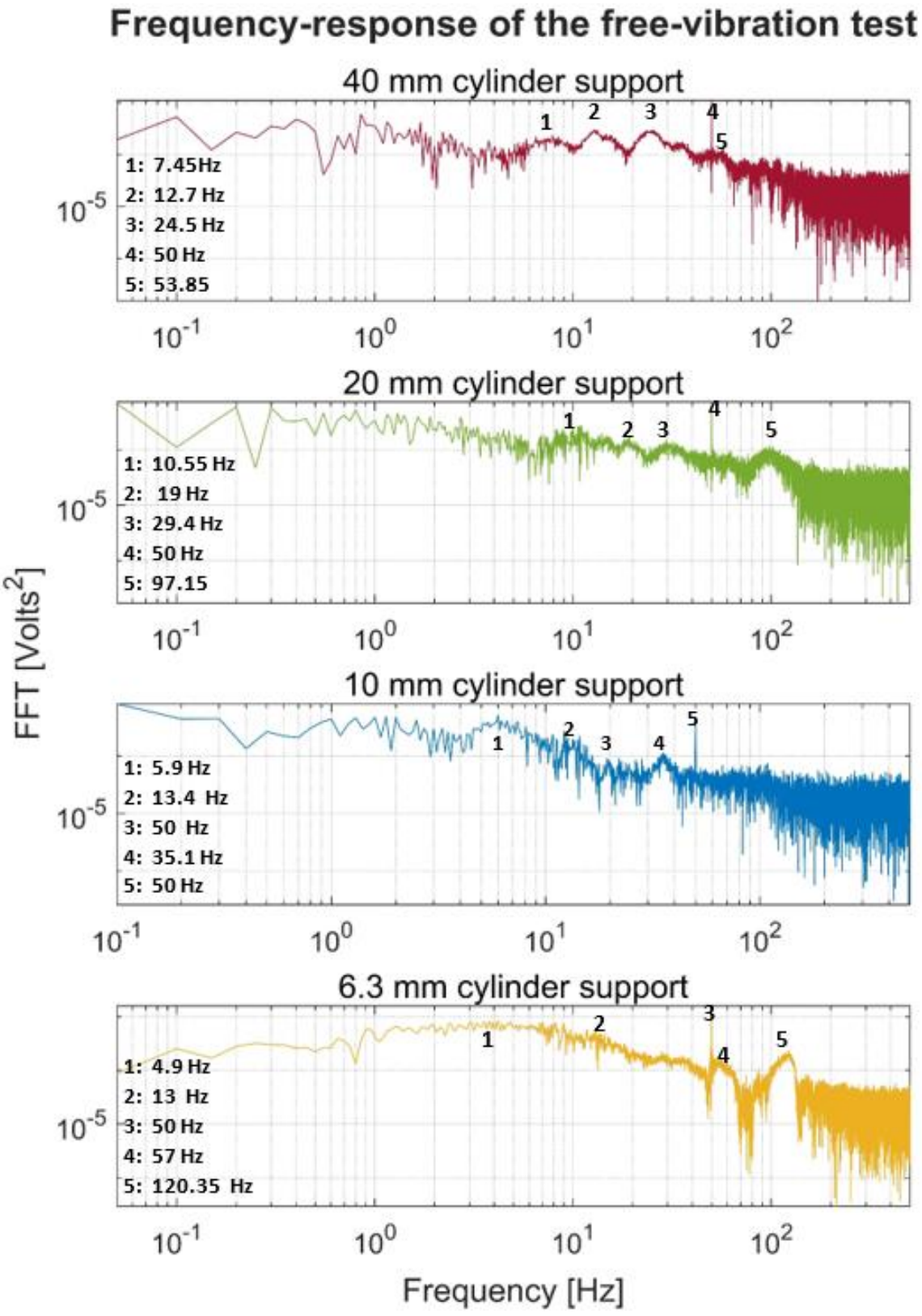

Figure 5.5 Frequency-response of the free-vibration tests of the cylinder–support system

5.4 Open-circuit Measurements:

5.4.1 Methods:

To study the response of the piezoelectric cylinders to airflow, each cylinder was subjected to airflow of a defined speed *U* while measuring the open-circuit voltage *V* signal generated on the cylinder surface. The voltage was measured via the same oscilloscope used in the free-vibration test. Each signal was recorded for a duration of twenty seconds with a temporal resolution of 0.32 milliseconds. The oscilloscope vertical resolution was set to 10 mV/division, while the vertical offset was set to zero. The recorded time signals were used to calculate the FFT of each measurement case. The computed spectrum spanned over 1 kHz centred at 500 Hz with a spectral resolution Δf of 0.0153 Hz. Table 5-III summarizes the data of acquisition settings.

Table 5-III Signal acquisition settings for Flow-Induced Vibration measurements.

Signal Duration [s]	20
Vertical Precision [mV/div.]	10
Temporal Resolution [ms]	0.32

The measurements were performed at wind speeds ranging from 1 to 7 m/s in steps of 1 m/s, with one additional measurement taken at a speed of 1.5 m/s. At each windspeed *U* for each cylinder of diameter D_{cyl}, it was possible to determine the Reynolds number *Re* of the flow using equation (5.1) , where the kinematic viscosity *v* was assumed to be 1.56×10^{-5} m^2/s. Then, it was possible to use Roshko's model for the Strouhal number *St* at *Re* above 300 [76] to calculate the respective Strouhal number using equation (5.2). Finally, it was possible to calculate the expected vortex shedding frequency f_s using equation (5.3).

$$Re = \frac{U\, D_{cyl}}{\nu} \tag{5.1}$$

$$St = 0.212\left(1 - \frac{12.7}{Re}\right) \tag{5.2}$$

$$f_s = \frac{St\, U}{D_{cyl}} \tag{5.3}$$

5.4.2 Results:

Figure (A – 1) – Figure (A – 8) in the appendix show the obtained time-responses from the four cylinders at different airflow speeds. The figures also indicate the shedding frequency f_s calculated using equation (5.3). From these figures, it can be noticed that the cylinders have indeed generated an oscillating voltage signal. Such oscillations are characteristic of the phenomenon of vortex shedding. For the 40, 20, and 6.3 mm cylinders, it was possible to find clear pulses in the signals at some flow speeds. To name a few examples, pulses were found in the signals from the three cylinders at a flow speed of 1 m/s. Moreover, the 10 mm cylinder gave interesting pulses at flow speeds of 1.5 and 7 m/s.

5.4.2.1 Effect of the Airflow Speed on the Cylinder Response

Figure 5.6 and Figure 5.7 show the variation in the mean voltage across each of the airflow speeds and the Reynolds number, respectively, for the four cylinders. By performing the measurements on cylinders of various diameters over the same speed range, it was possible to demonstrate the energy transfer behaviour over a wide range of Reynolds numbers, as shown in Figure 5.7. The lower range of Reynolds numbers was demonstrated using the smaller diameters, while the larger range was demonstrated using the larger diameters.

From Figure 5.6, it can be seen that the 40- and the 20-mm cylinders tended to generate more voltage at a lower flow speed—a less turbulent flow—generating a maximum voltage of 11.7 and 12.2 mV, respectively, at a flow speed of 1 m/s. However, as the velocity increased, the two cylinders' output dropped, generating minima of 3.6 and −1.3 mV, respectively, at a flow speed of 7 m/s. The drop rate of the mean of the two cylinders changed over airspeeds of 1.5–3 m/s, where the 40-mm cylinder drop decelerated over the range mentioned above while the 20-mm cylinder drop even rose before dropping again at speeds above 3 m/s.

The cylinders' behaviour can be interpreted differently across the Reynolds number scale, as shown in Figure 5.7. It can be seen that the two cylinders' voltages tended to decline with the increase in Reynolds number, with an exception for the 20-mm cylinder in the range $2000 < Re < 4000$—which corresponds to $1.5 < U < 3$ m/s—which is the transitional region between the laminar and turbulent flow. Unfortunately, it was not possible to test these two cylinders in the laminar range of the Reynolds number scale, since these cylinders' sizes would require lower velocities than those that were rated for the wind tunnel operation. Finally, it was quite interesting that the two cylinders showed an identical and substantial voltage drop rate at $Re > 5000$.

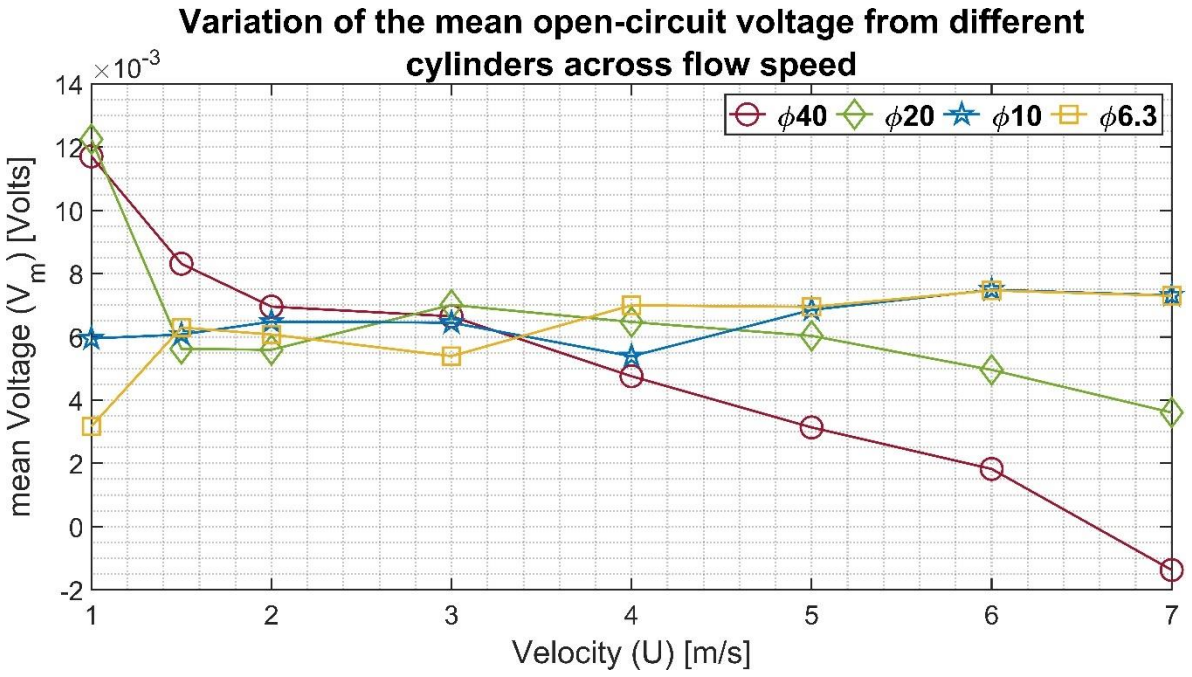

Figure 5.6 Variation in the mean voltage V_m from all cylinders across the flow speed U

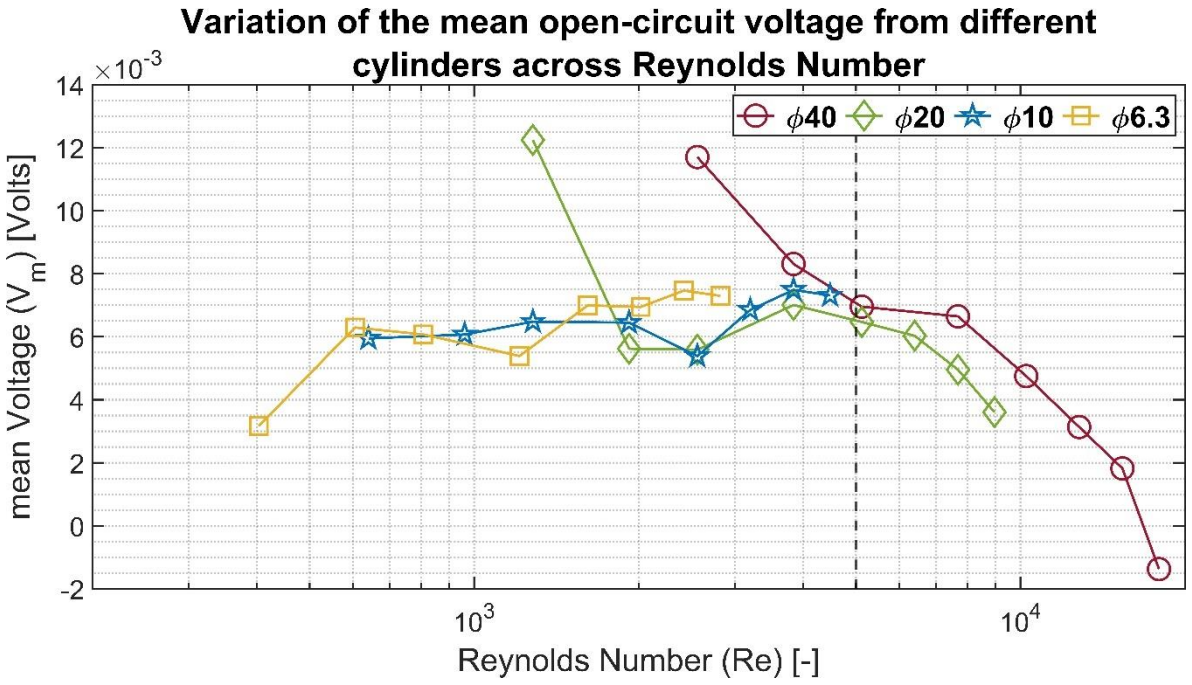

Figure 5.7 Variation in the mean voltage V_m from all cylinders across Reynolds number Re. The black dashed line shows the onset of vortex shedding degradation according to [77].

Considering the 10- and 6.3-mm cylinders, it was found that they showed different behaviours from the first two cylinders. The cylinders' mean voltage tended to increase with

the increase in the flow speed, with one exception for each cylinder. The 10-mm cylinder voltage dropped at a speed of 4 m/s—Reynolds number of 2562, while the 6.3-mm cylinder voltage dropped over the speed range 1.5–3 m/s—Reynolds number of 600–1200. Finally, it is important to point out that it is expected that the cylinder size will play a role in interaction with the flow turbulence according to the relationship between the cylinder diameter and the turbulence scale.

The drop in the generated voltage at Re > 5000 was found to agree with the findings of Norberg [77]. He showed using Laser Doppler Velocimetry, LDV, that the vortex shedding is of a high quality over the range $260 < Re < 5000$, while it changes its appearance over $5000 < Re < 2 \times 10^5$, where it becomes broader due to the change in shedding frequency over time. Therefore, a vertical dashed line is plotted in Figure 5.7 at $Re = 5000$. It is clear from the figure how the mean voltage drops past this line.

5.4.2.2 Frequency Response

Figure 5.8 – Figure 5.15 show the frequency-response that was obtained from the four cylinders. In these figures, a black vertical dashed line indicates the expected shedding frequency, while black solid lines indicate the five measured natural frequency of the respective system presented in Table 5-II. The FFT of the voltage signals extended over a wide range—thousands-fold, as will be shown later in Section 5.4.3.1.3. The present section will focus only on the range up to 2.2×10^{-4} on a linear scale. It was interesting to find some significant broadband peaks that coincided with the shedding frequencies f_s calculated from equation (5.3), while other peaks coincided with the natural frequencies measured in Section 5.3.

Figure 5.8 and Figure 5.9 show the generated frequency spectra from the 40-mm cylinder on a linear vertical scale. It can be seen that a peak was created from the 1.5 m/s flow at a frequency of 3.9 Hz. This peak did not coincide with any of the system frequencies, which indicates it belongs to the flow dynamics. However, it was also far from the shedding frequency. For the flows at 2 and 3 m/s, peaks were created at 9.75 Hz and 16.6 Hz, respectively, which well-matched with the respective shedding frequencies, as well as were far from any of the natural frequencies.

Flows at speeds of 4–7 m/s had their shedding frequency almost-matched with the shedding frequency; however, it was always in the vicinity of a system frequency. Unfortunately, such a fact may indicate it was a result of both the flow and system characteristics. Finally, the flow at one m/s had its peak at 10.6 Hz away from the shedding frequency and quite close to the system's. Unfortunately, such results indicate that the design of the cylinder support was not suitable and should have considered targeting a precisely-designed natural frequency that lies away from the shedding frequency.

Figure 5.10 and Figure 5.11 show the generated frequency spectra from the 20-mm cylinder. Unfortunately, there was a quite good match between the system frequencies and

the expected shedding frequency at speeds from 1 up to 5 m/s. Therefore, it would not be possible to use the frequency data from these measurements. At a speed of 6 m/s, a peak was formed; however, it matched with the system frequency. Finally, at a speed of 7 m/s, a peak has well-matched with the shedding frequency, and it was relatively far from the system frequencies.

Figure 5.12 and Figure 5.13 show the frequency spectra of the signals from the 10 mm cylinder. It was interesting to notice the growth of a very strong peak around 9 Hz between two system frequencies. The peak started to appear at speeds of 2–6 m/s; however, it disappeared at a speed of 7 m/s. Apart from this peak, many other spike-frequencies were formed at frequencies under 2 Hz.

Figure 5.14 and Figure 5.15 show the frequency spectra of the signals from the 6.3 mm cylinder. Similar to the 10 mm cylinder, a significant peak started to appear at speeds of 2–7 m/s around a frequency of 12 Hz together with its harmonics. Unfortunately, the peak has very-well-matched with the system frequencies. In addition to these peaks, the cylinder has generated several spike-like peaks at frequencies under 1 Hz.

Finally, it is worth mentioning that the 6.3 mm cylinder specifically has been the cylinder most affected by the system frequencies. This could be due to the fact that it has the least mass among all the cylinders. On one side, the least mass would make it the most affected by the support vibration. On the other side,—being the smallest cylinder—the cylinder would have the least surface area, which means the least ability to collect the flow energy to create electric charges. These two facts together shall amplify the effect of the support on the account of the effect of the flow.

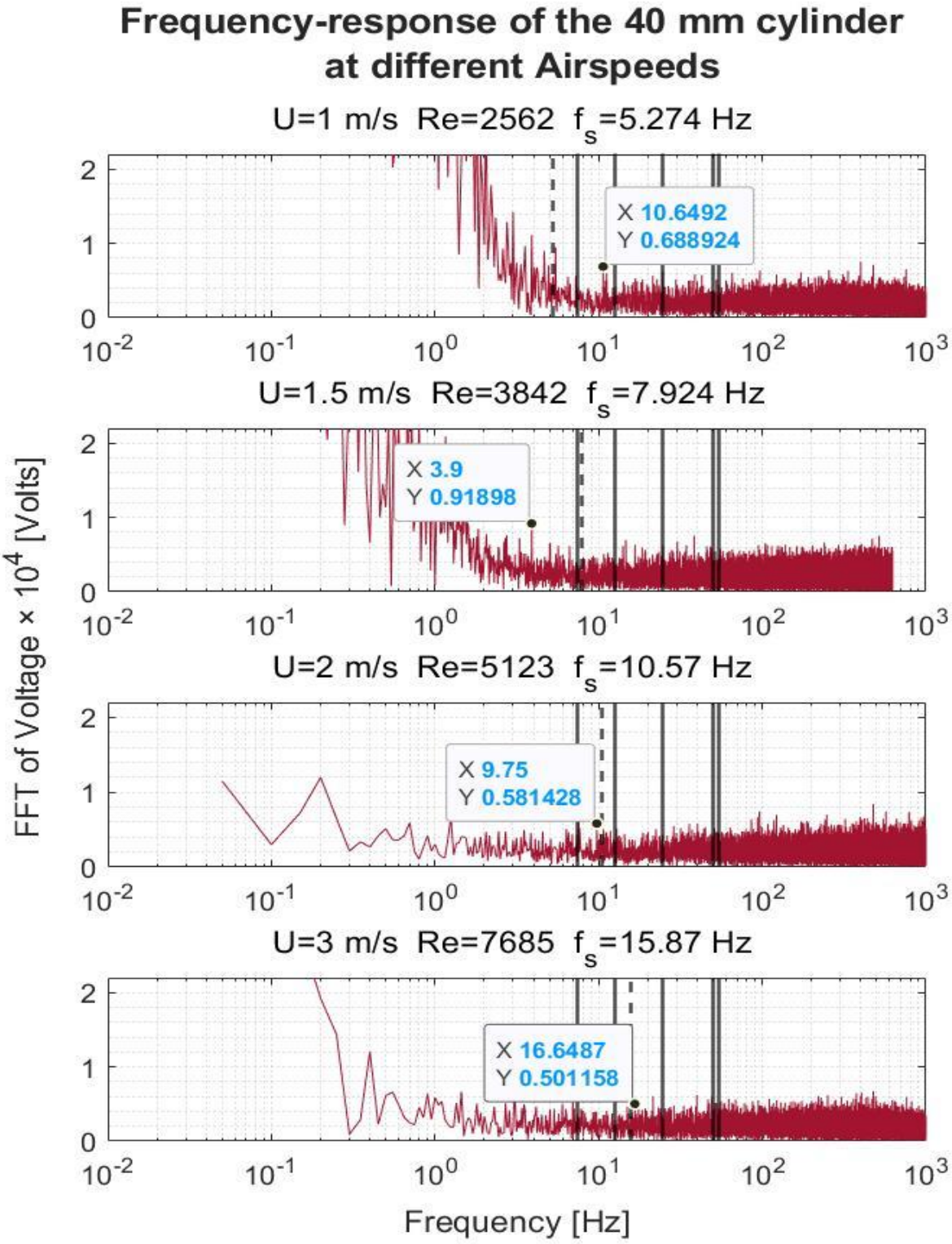

Figure 5.8 Frequency-response of Cylinder (A), diameter 40 mm, at flow speed 1–3 m/s. Black solid lines: natural frequency. Black dashed lines: shedding frequency calculated from Roshko's model.

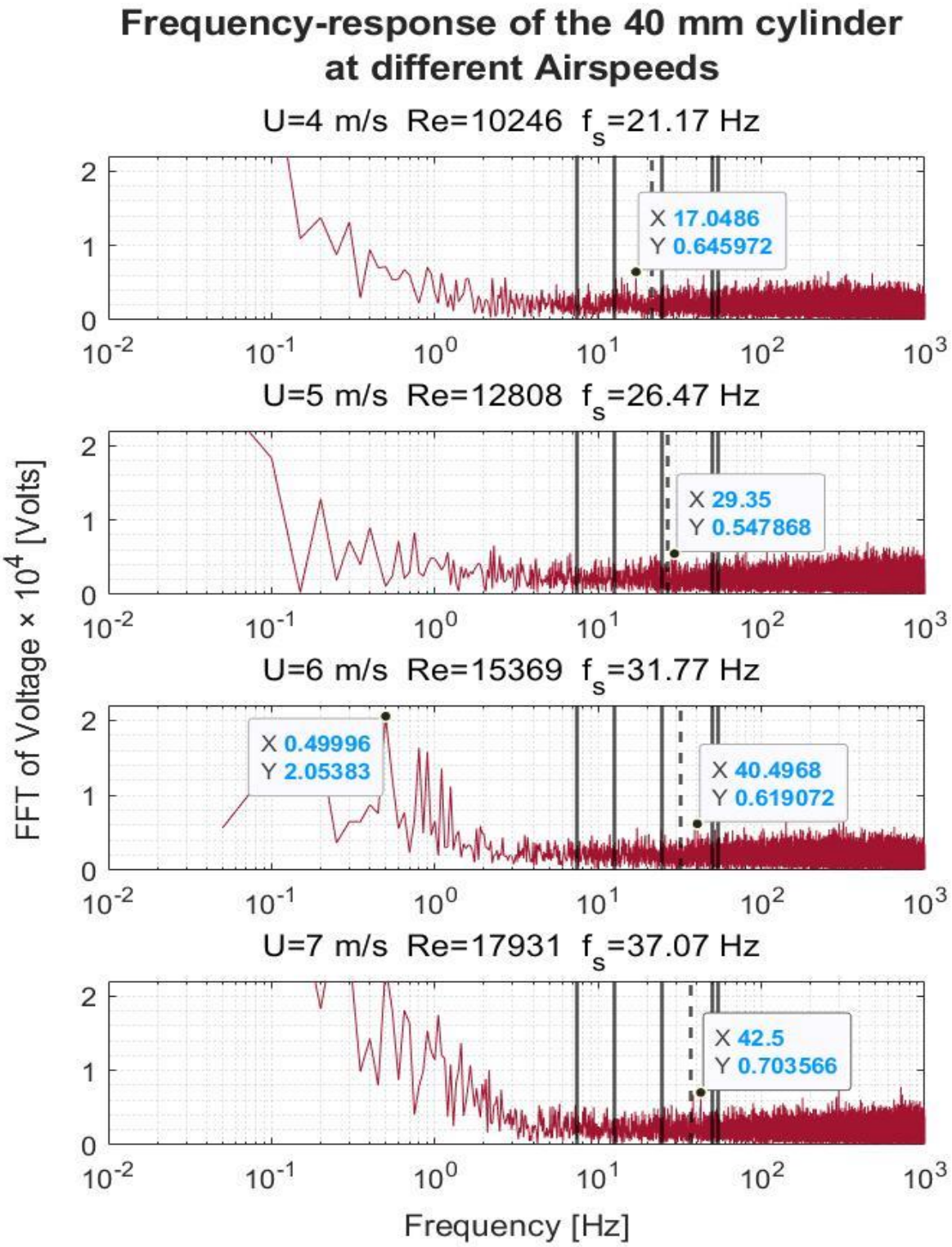

Figure 5.9 Frequency-response of Cylinder (A), diameter 40 mm, at flow speed 4–7 m/s. Black solid lines: natural frequency. Black dashed lines: shedding frequency calculated from Roshko's model.

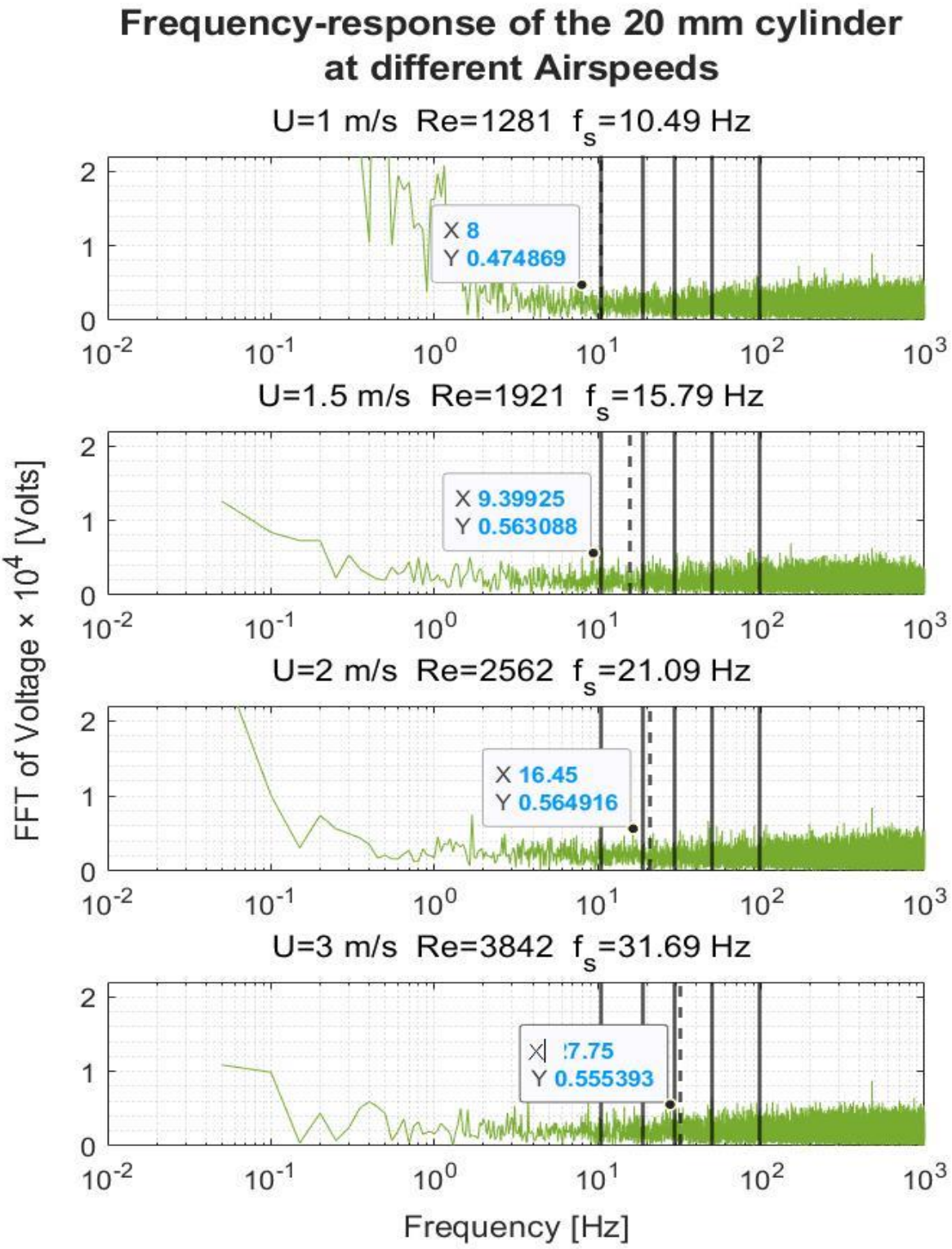

Figure 5.10 Frequency-response of Cylinder (B), diameter 20 mm, at flow speed 1–3 m/s. Black solid lines: natural frequency. Black dashed lines: shedding frequency calculated from Roshko's model.

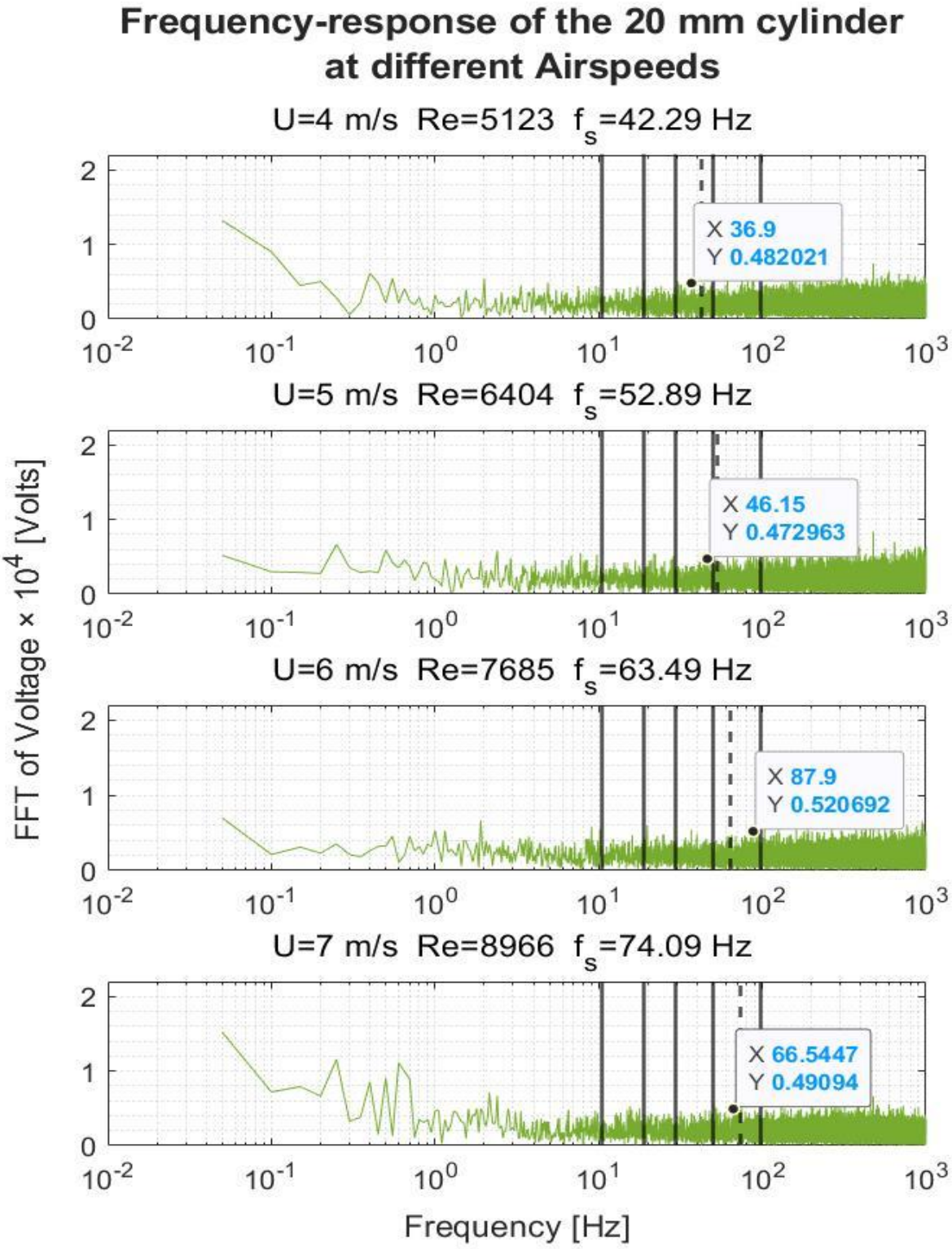

Figure 5.11 Frequency-response of Cylinder (B), diameter 20 mm, flow speed 4–7 m/s. Black solid lines: natural frequency. Black dashed lines: shedding frequency calculated from Roshko's model.

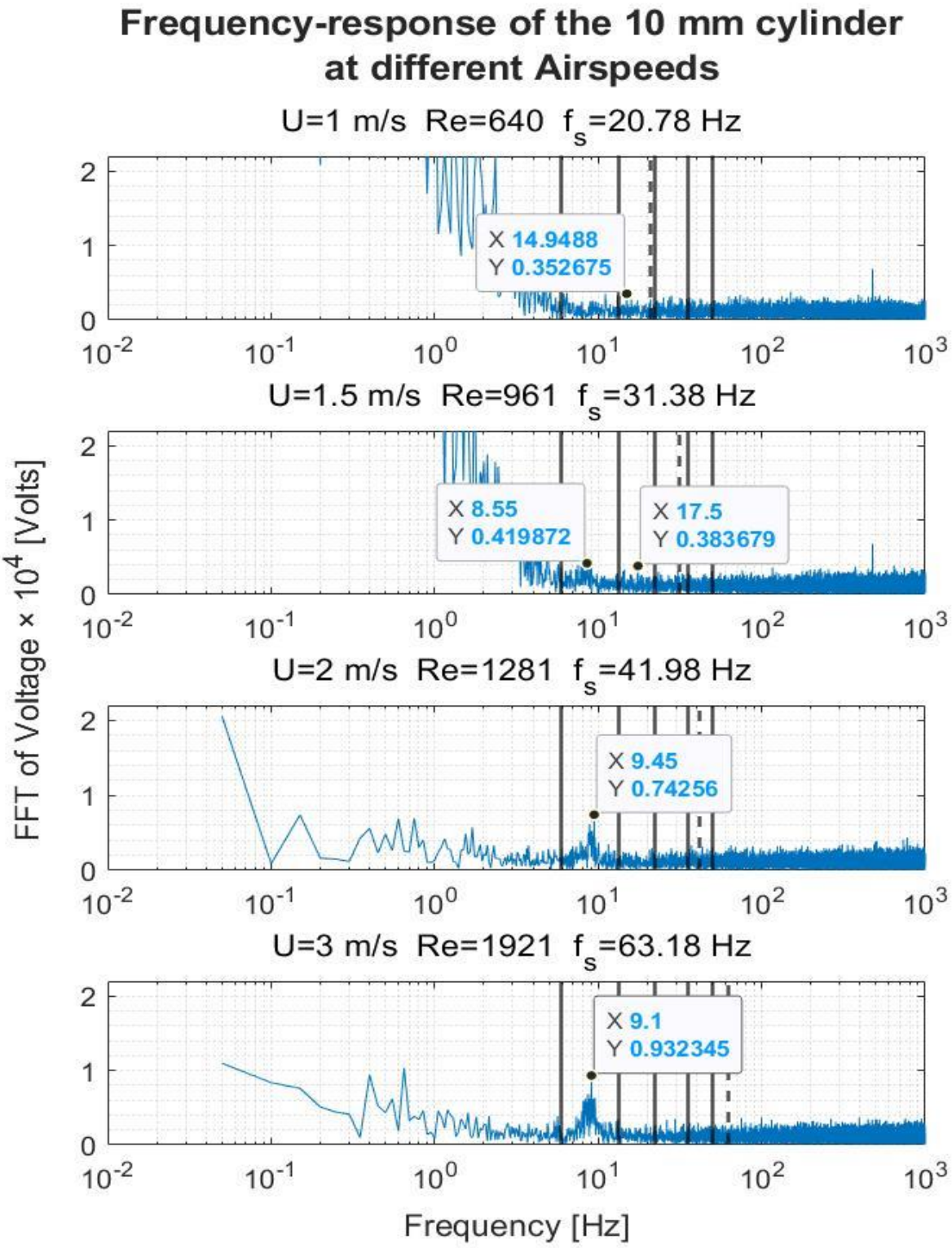

Figure 5.12 Frequency-response of Cylinder (C), diameter 10 mm, at flow speed 1–3 m/s. Black solid lines: natural frequency. Black dashed lines: shedding frequency calculated from Roshko's model.

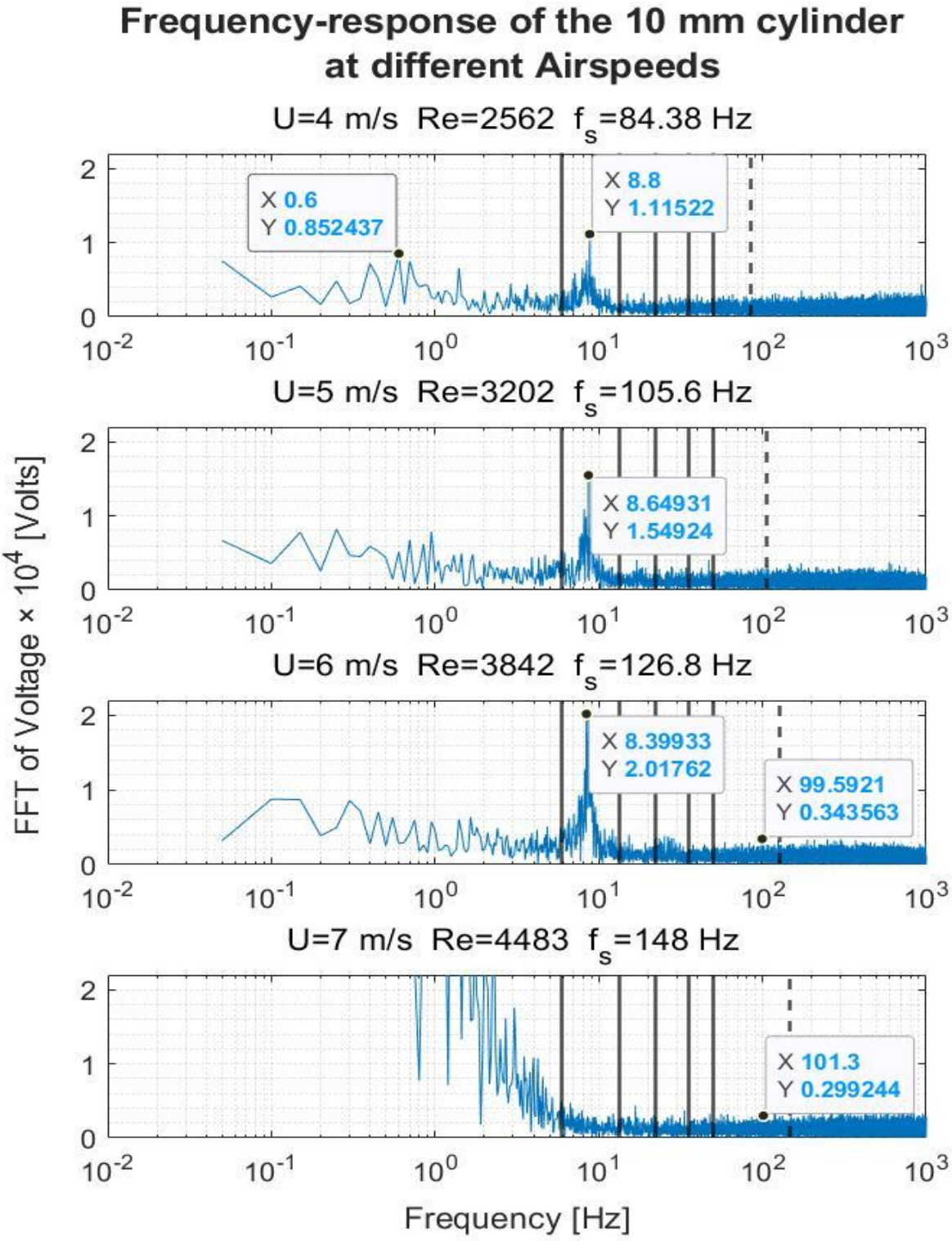

Figure 5.13 Frequency-response of Cylinder (C), diameter 10 mm, at flow speed 4–7 m/s. Black solid lines: natural frequency. Black dashed lines: shedding frequency calculated from Roshko's model.

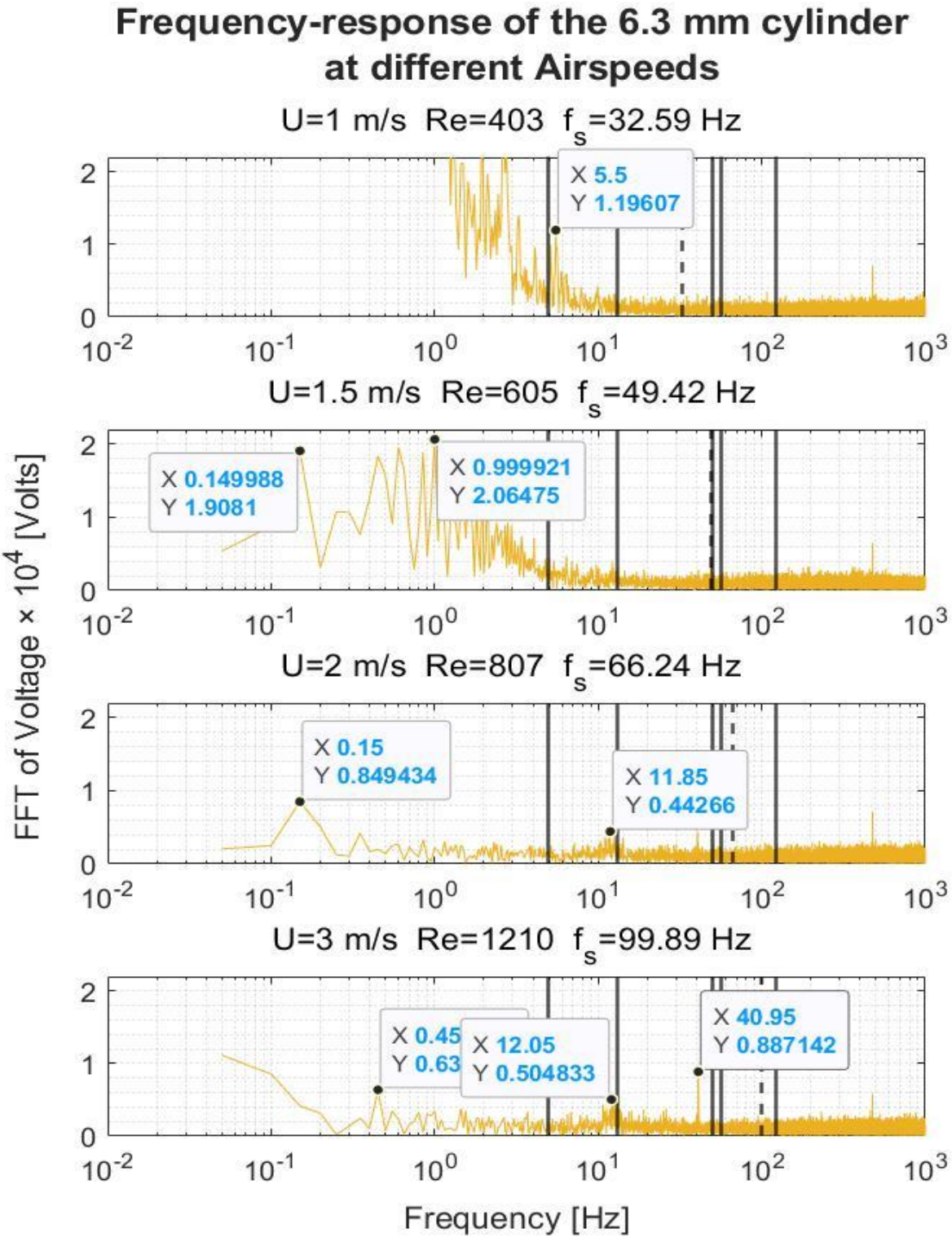

Figure 5.14 Frequency-response of Cylinder (D), diameter 6.3 mm, at flowspeed 1–3 m/s. Black solid lines: natural frequency. Black dashed lines: shedding frequency calculated from Roshko's model.

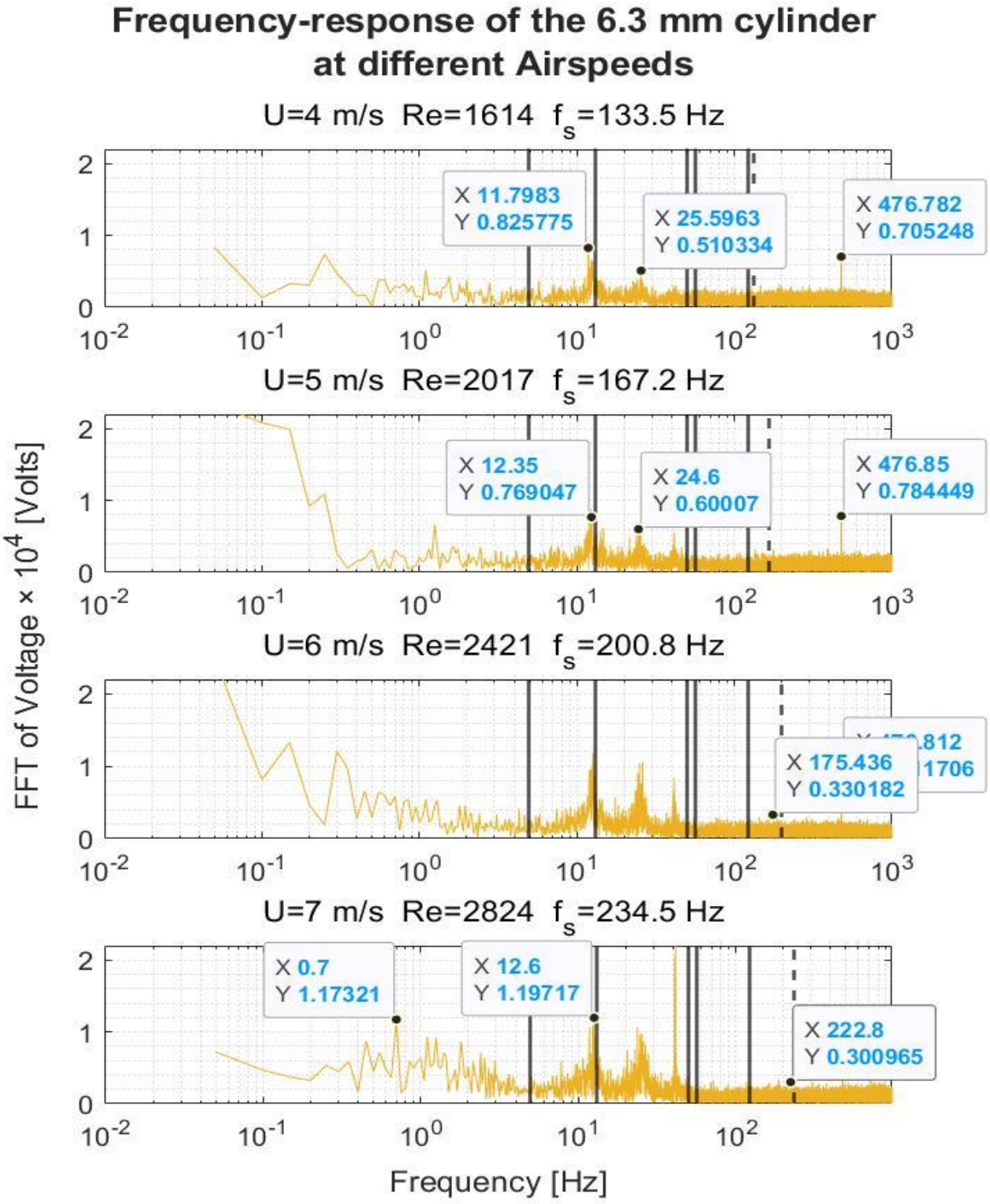

Figure 5.15 Frequency-response of Cylinder (D), diameter 6.3 mm, at flow speed 4–7 m/s. Black solid lines: natural frequency. Black dashed lines: shedding frequency calculated from Roshko's model.

5.4.3 Discussion

The first implication of the obtained results is that the contribution of the ambient electric field in the signals' power is relatively weak. This is concluded from the fact of the absence of any strong peak at a frequency of 50 Hz in any of the frequency-responses. This implies that most of the measured voltage is indeed created by the flow, which is important for the evaluation of energy harvesting.

5.4.3.1 The analogy between vortex shedding and piezoelectric transduction

5.4.3.1.1 Variation of the mean generated voltage versus the quality of vortex shedding

It was expected that the energy content of the airflow—and, hence, the cylinder open-circuit voltage—would be proportional to the second power of airspeed. However, the data in Figure 5.6 showed otherwise. It was difficult to find a general trend for the output voltage over airspeed. However, more clear trends in the voltage over Reynolds number were found in Figure 5.7, where it was clearly shown that the generated voltage drops at Re > 5000. This drop was confirmed by two cylinders, the 40-mm and the 20-mm cylinders, and agreed with other data of vortex-shedding off cylinders independently measured by [77] using Laser-Doppler-Velocimetry. This agreement may indicate an analogy between the fluid phenomena and the piezoelectric transduction—at least for the 40- and 20-mm cylinders. Moreover, it proved that the critical parameter for VIV harvesting is the Reynolds number rather than the airspeed.

5.4.3.1.2 Variation in charge generation across Reynolds Number

Piezoelectric transducers respond to mechanical loads by forming electric charges. According to the transducer's electrical capacitance, the electric charges will form an electric potential. Therefore, it would be interesting to look at the energy transfer process—from mechanical to electrical—using the above data, normalized to the individual cylinder characteristics.

To exclude the effect of the individual cylinder—the cylinder surface area and the capacitance—on the generated signal, the mean electric charge Q_{mean} and the specific electric charge q—charge per unit cylinder surface area—were calculated using equations (5.4) and (5.5) respectively. The total electric charge was plotted across flow speed and Reynolds number in Figure 5.16 and Figure 5.17, respectively, and so was the specific electric charge in Figure 5.18 and Figure 5.19, respectively.

$$Q_{mean} = CV_m \tag{5.4}$$

$$q = \frac{Q_{mean}}{\pi\, D_{cyl} L_{cyl}} \tag{5.5}$$

In Figure 5.16, it can be noticed that the total electric charge had a similar trend across windspeed similar to that of the mean voltage shown before in Figure 5.6. This similarity was expected due to the linear relation between the electric charge and the voltage. Moreover, the data in Figure 5.16 show that more charges were generated from the cylinder with the bigger diameter. This behaviour prevailed up to a speed of 5 m/s. Above this speed, the 10-mm cylinder had the highest charge.

In the sub-five-meter-per-second range, the 10- and 20-mm cylinders had almost equal charge values. It is worth mentioning that the difference between their capacitances is 1 nF, as was indicated in Table 2-II. The data appear more clearly over the Reynolds number scale as plotted in Figure 5.17, where again, a black dashed line represents the onset of vortex shedding degradation according to [77], similar to the behaviour of mean voltage shown in Figure 5.7.

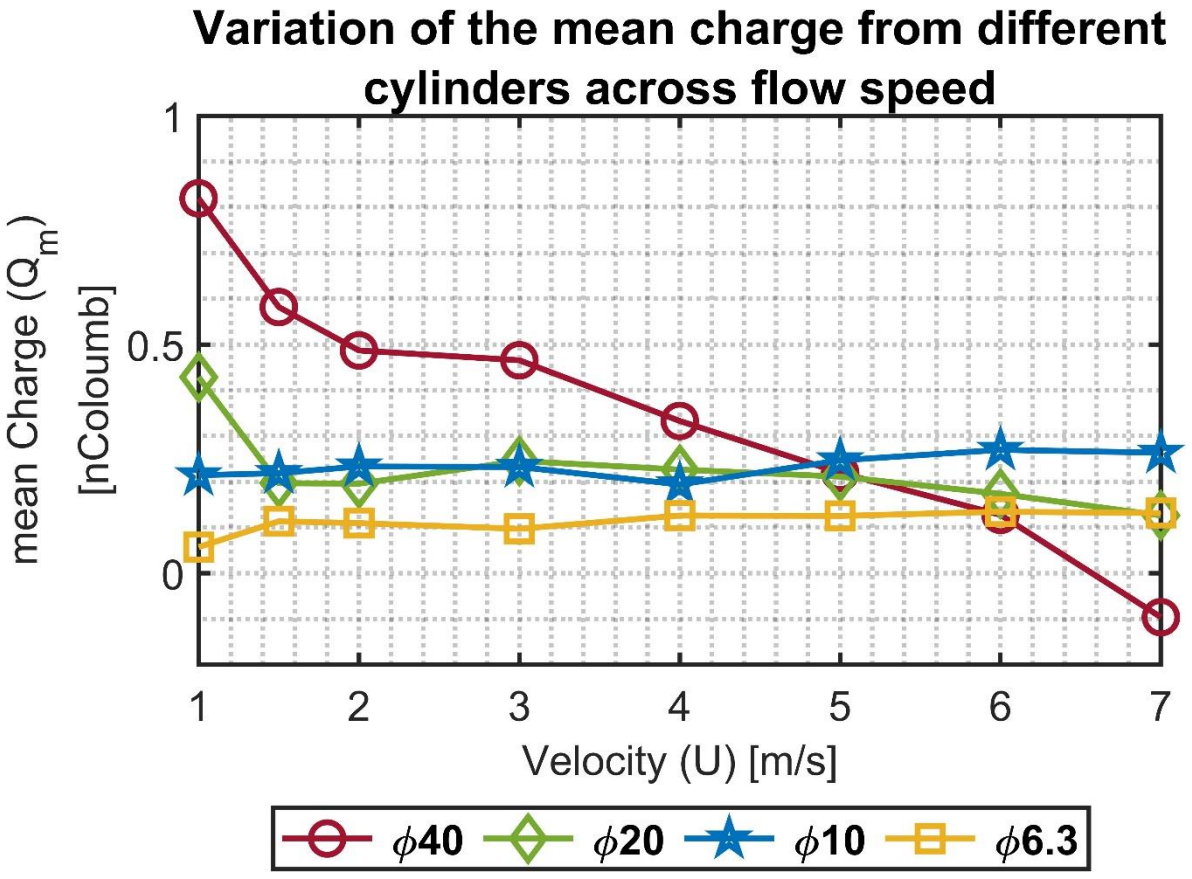

Figure 5.16 Variation of the mean total charge Q across the flow speed.

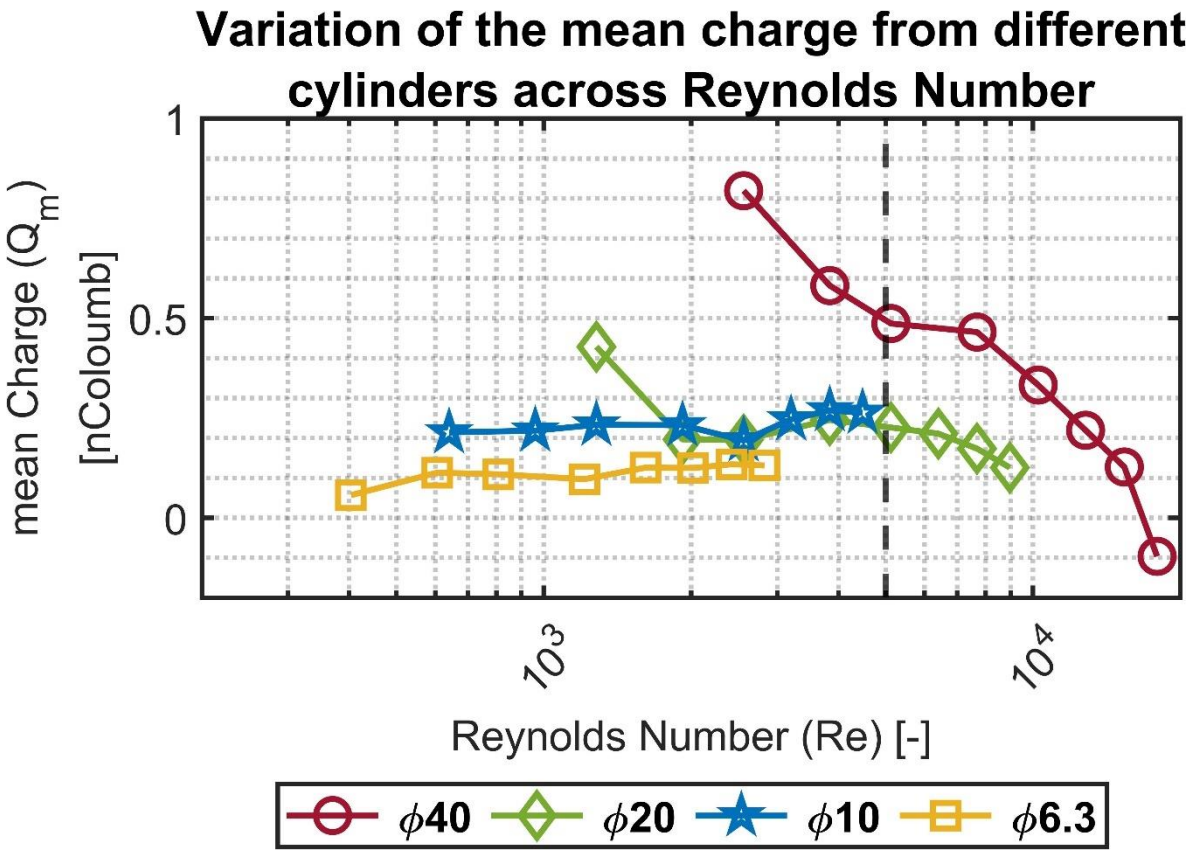

Figure 5.17 Variation of the mean total charge Q_m across Reynolds number. The black dashed line shows the onset of vortex shedding degradation according to [77]

Figure 5.18 and Figure 5.19 show the variation in the specific electric charge over the flow speed and Reynolds number, respectively. In Figure 5.18, it was interesting to find that the 10-mm cylinder had the highest specific charge generation among all cylinders. Moreover, charge generation had two peaks, at 2 m/s and 6 m/s, which corresponds to Reynolds numbers of 1281 and 3842, respectively. By plotting these data across the Reynolds number range in Figure 5.19, it was interesting to find that the 40-mm and 20-mm cylinders achieved continuity in the specific charge at Reynolds number ranges above 5000, while such continuity was missing for the 10- and 6.3-mm cylinders. Again like Figure 5.7, a black dashed line indicates in Figure 5.19 the onset of vortex-shedding degradation according to Norberg [77].

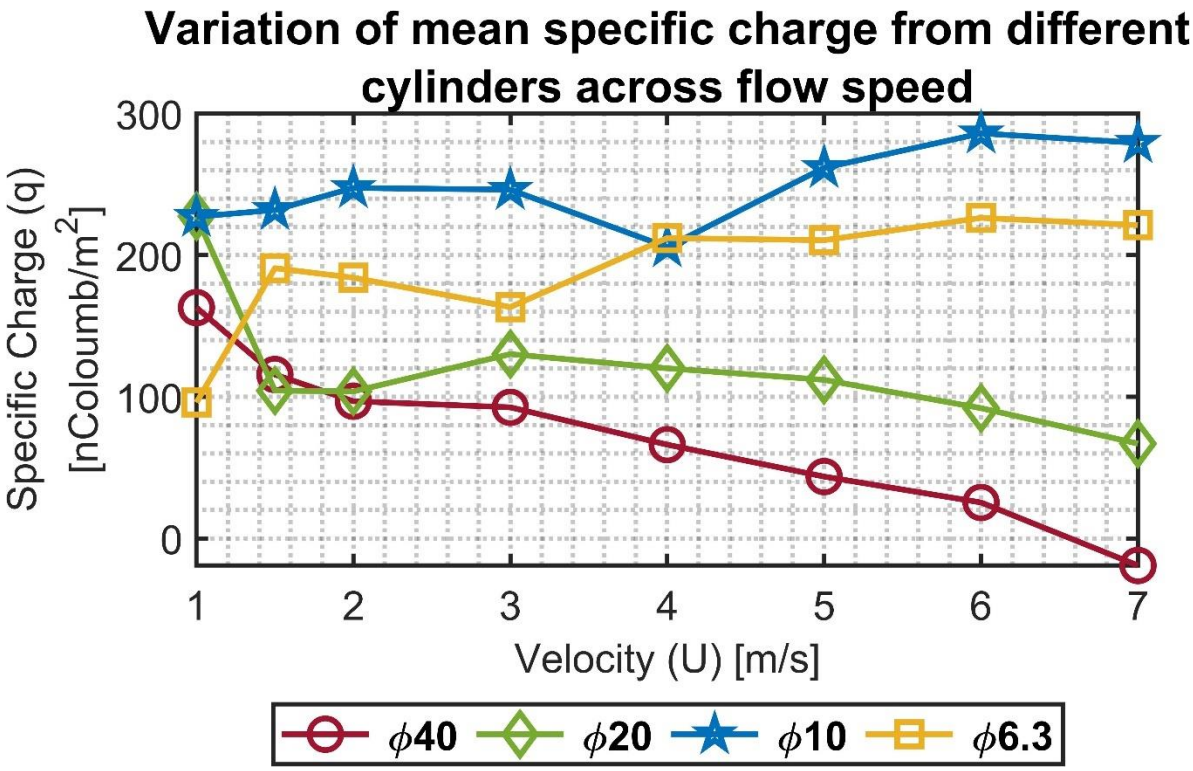

Figure 5.18 Variation of the specific charge q across the flow speed.

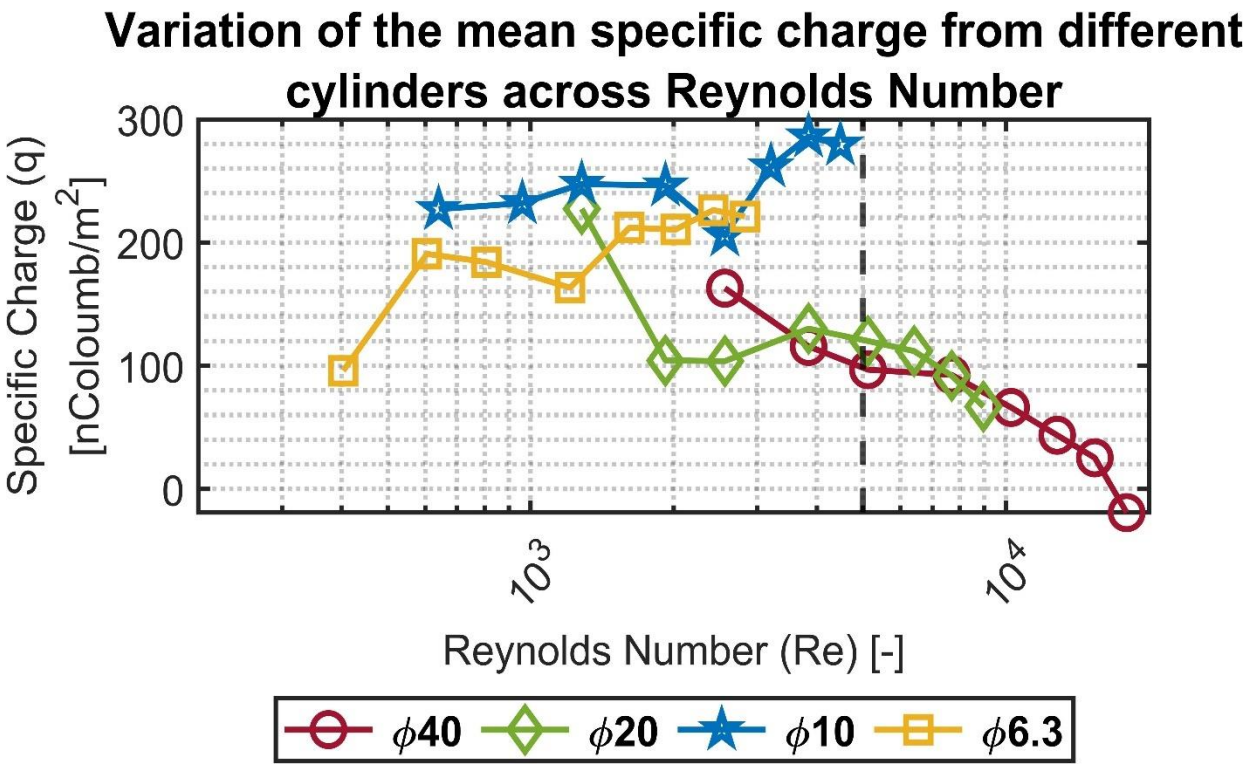

Figure 5.19 Variation of the specific charge q across Reynolds number. The black dashed line shows the onset of vortex shedding degradation according to [73]

5.4.3.1.3 The frequency response

Figure 5.20 – Figure 5.27 show the generated frequency spectra shown before–however in a logarithmic scale–together with lines indicating logarithmic drop rates of five-thirds and two-thirds, each plotted above the regions of the FFT that had such a drop rate.

Figure 5.20 and Figure 5.21 show the response of the 40-mm cylinder. For flows of 1 m/s, the strength of the FFT followed a two-thirds logarithmic drop rate from the lowest frequency up to 1 Hz. Over 1–5 Hz, the drop rate was five-thirds. The same behaviour was found at flows of 1.5 m/s and 7 m/s, with a transition from the two-thirds rate to the five-thirds rate occurring at a higher frequency. A two-thirds drop rate was captured over some frequency ranges for the 4 m/s and 6 m/s airflow speeds. For the 20-mm cylinder, shown in Figure 5.22 and Figure 5.23, it was only possible to capture the five-thirds rate in the case of the 1 m/s speed, while a two-thirds rate was captured for the 4 m/s speed.

For the 10-mm cylinder responses shown in Figure 5.24 and Figure 5.25, the two drop rates were found together at speeds of 1 and 1.5 m/s. Moreover, a two-thirds rate was found at 3 m/s and 4 m/s flow speeds, while a five-thirds rate was found at 7 m/s. Finally, Figure 5.26 and Figure 5.27 show the frequency spectrum from the 6.3 mm cylinder. Both the drop rates were found together in case of the 1 m/s and 1.5 m/s speeds. The two-thirds rate was found at a speed of 3 m/s and 4 m/s, while the five-thirds rate was found in the 7 m/s only.

From the previous discussion, it is evident that it was always possible to find a five-thirds linear drop rate at a speed of 1 m/s—the most laminar measurement for each cylinder—from all the cylinders. It was even possible to find this rate at other flow velocities. This linear drop—being plotted on a logarithmic plot versus frequency—indicates that the voltage *V* is distributed across its frequency *f* according to a power law of order of negative five-thirds as summarized by equation (5.6), where *ß* is a proportionality constant.

Assuming that the generated voltage *V* corresponds to the turbulence energy of the flow *E* and that the frequency *f* is analogous to the turbulence wavenumber *k*, this model is found to resemble the model established by Kolmogorov to describe a turbulent flow in the inertial range of the Reynolds number and how the different turbulence scales interact and cascade the energy from the larger scales to the smaller ones [78]. His model was described by equation (5.7) which relates the turbulence spectral energy *E(k)* of each wave number *k* to the respective wavenumber and the turbulence dissipation rate ε_k, where α is another proportionality constant. Comparing equations (5.6) and (5.7), the level of resemblance between the piezoelectric transduction and fluid turbulence is clear.

$$\mathrm{V}(f) = \beta \times (f)^{\frac{-5}{3}} \tag{5.6}$$

$$\mathrm{E(k)} = \alpha . \varepsilon_k^{\frac{-2}{3}} \times (k)^{\frac{-5}{3}} \tag{5.7}$$

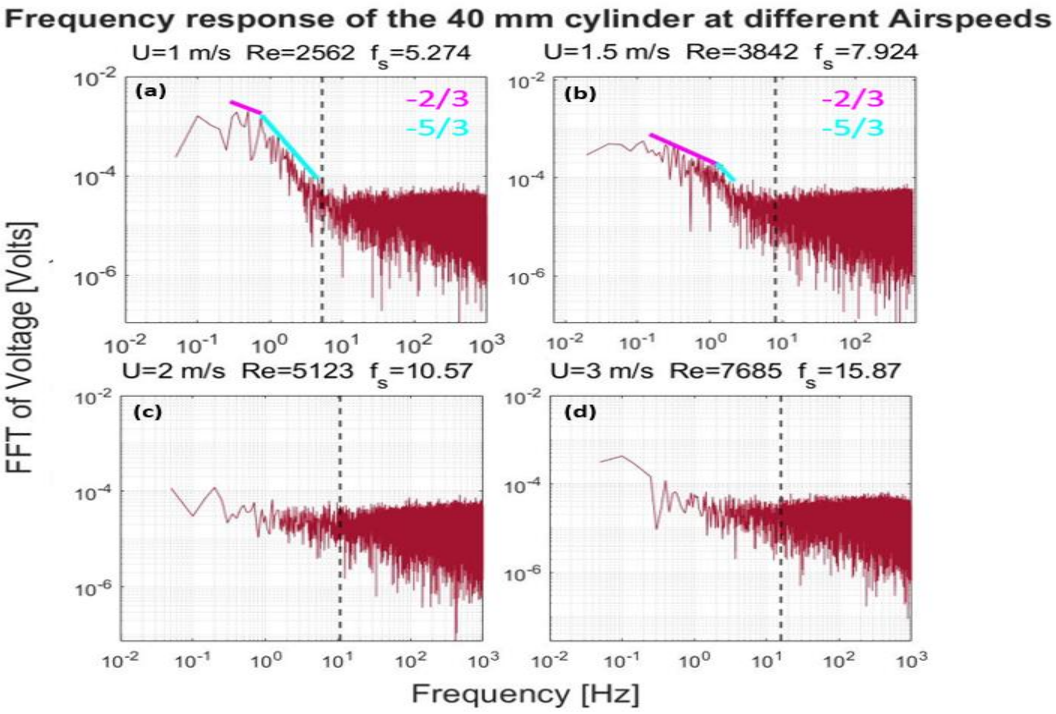

Figure 5.20 Frequency-response of Cylinder (A), diameter 40 mm, at flowspeeds 1–3 m/s in relation to Kolomogorov's Scales

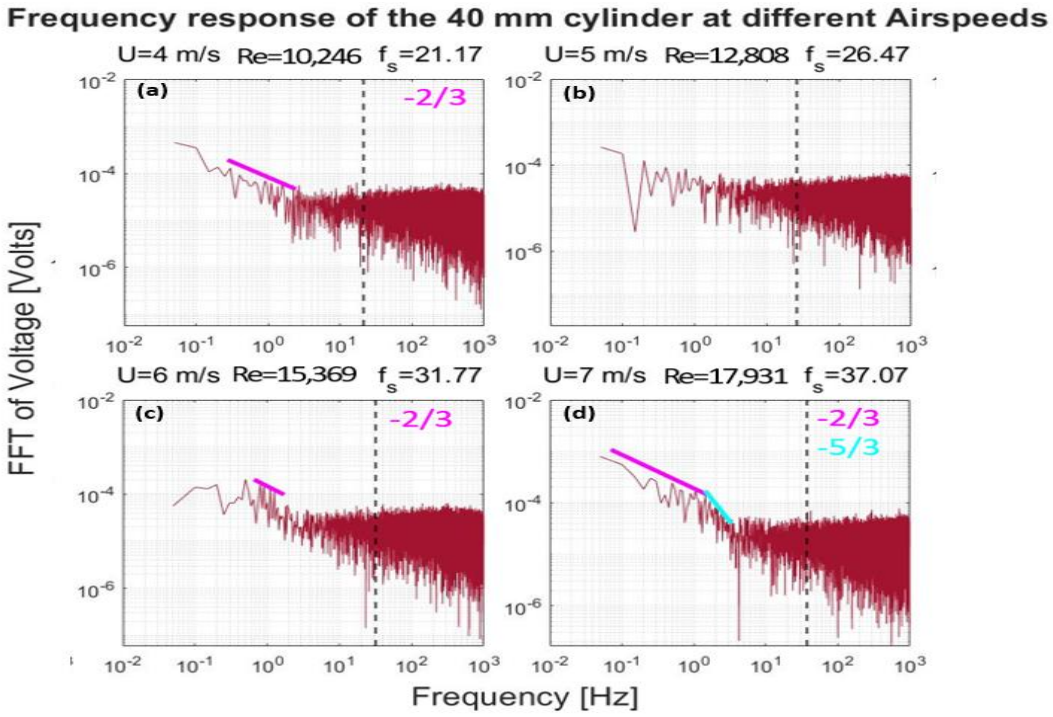

Figure 5.21 Frequency-response of Cylinder (A), diameter 40 mm, at flowspeeds 4–7 m/s in relation to Kolomogorov's Scales

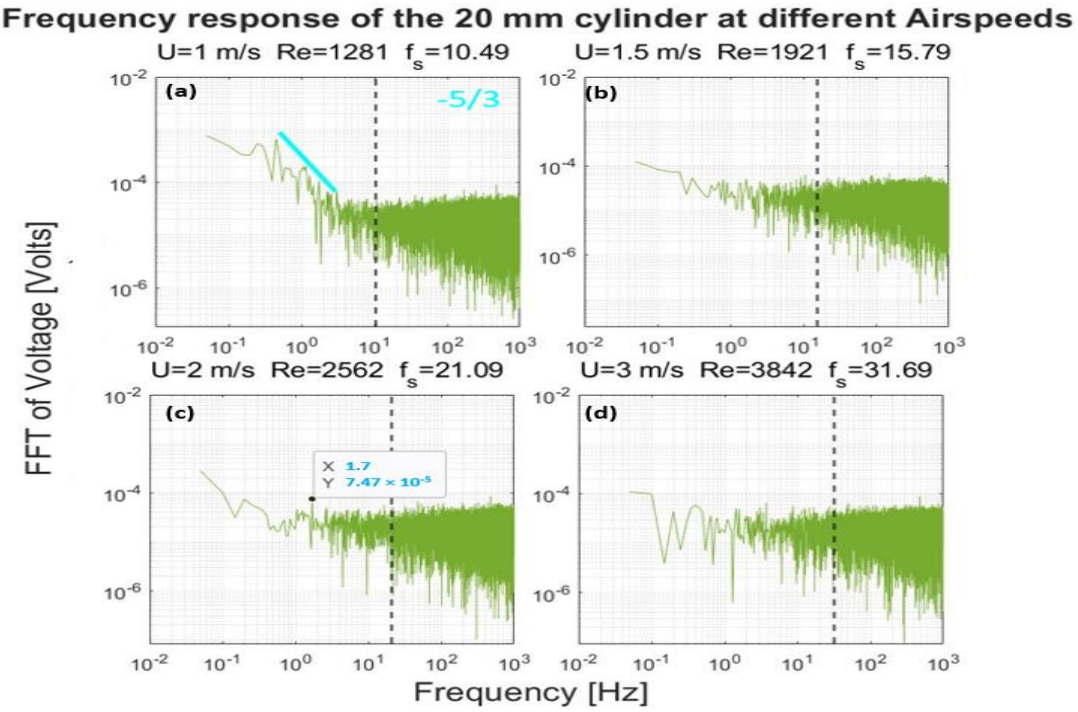

Figure 5.22 Frequency-response of Cylinder (B), diameter 20 mm, at flowspeeds 1–3 m/s in relation to Kolomogorov's Scales

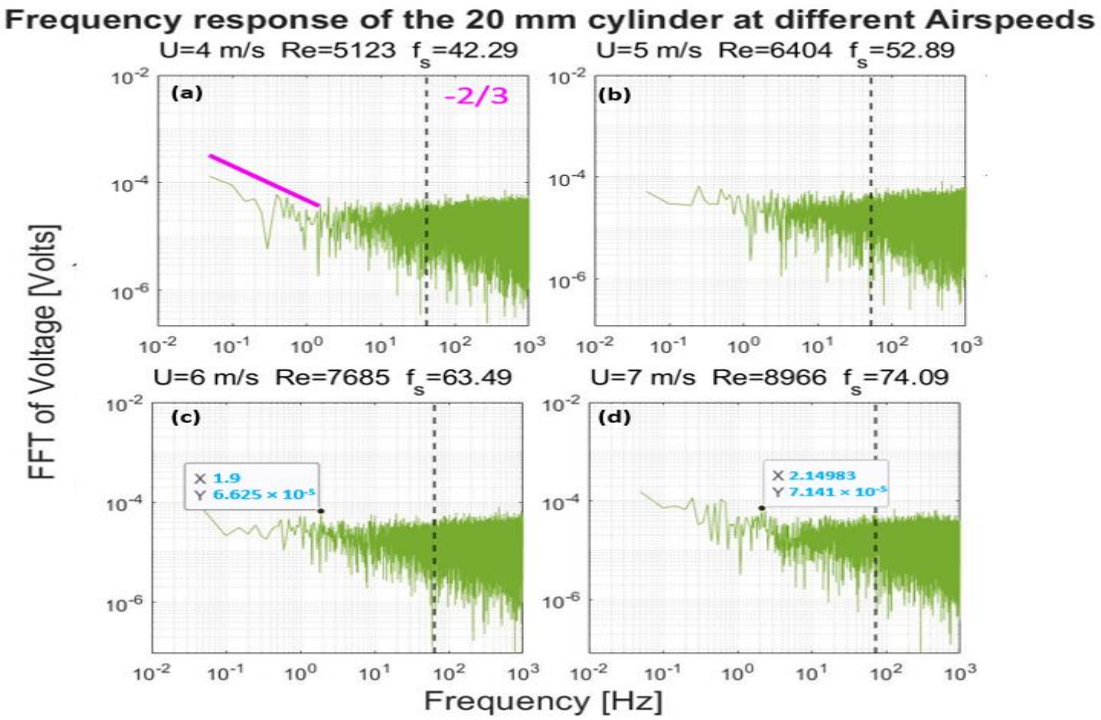

Figure 5.23 Frequency-response of Cylinder (B), diameter 20 mm, at flowspeeds 4–7 m/s in relation to Kolomogorov's Scales

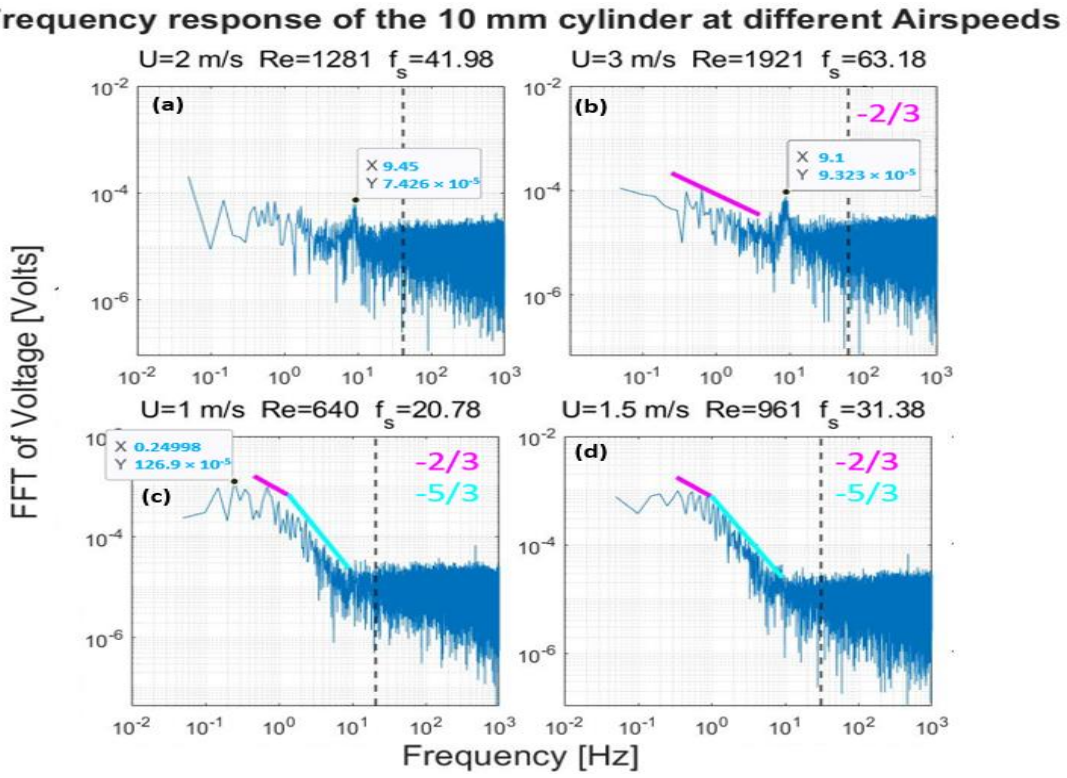

Figure 5.24 Frequency-response of Cylinder (C), diameter 10 mm, at flowspeeds 1–3 m/s in relation to Kolomogorov's Scales

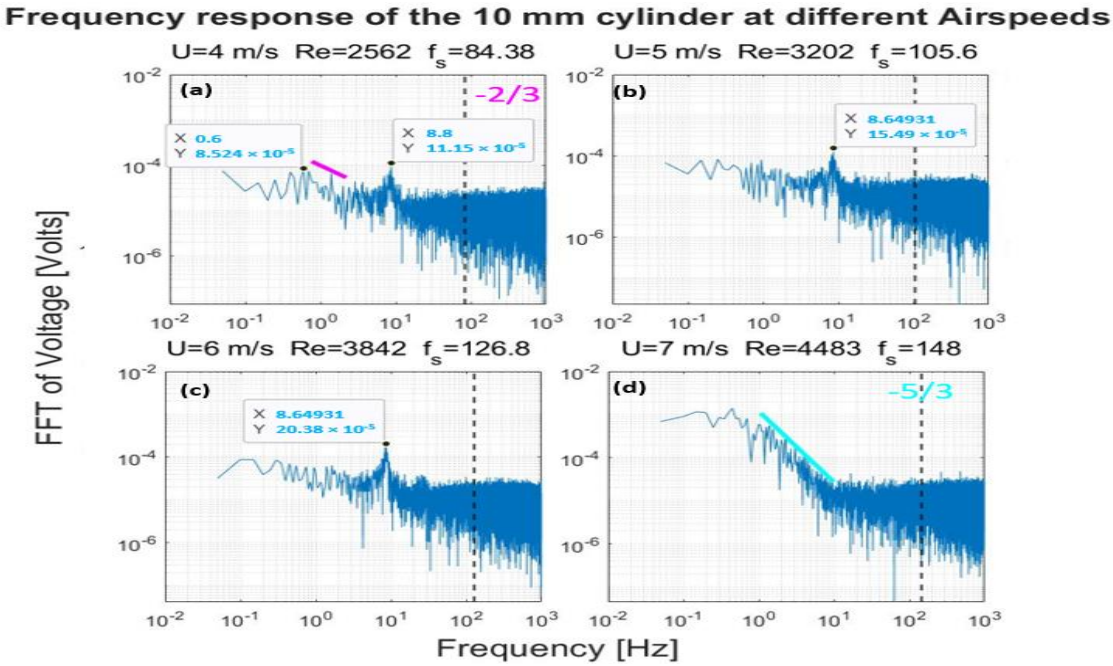

Figure 5.25 Frequency-response of Cylinder (C), diameter 10 mm, at flowspeeds 4–7 m/s in relation to Kolomogorov's Scales

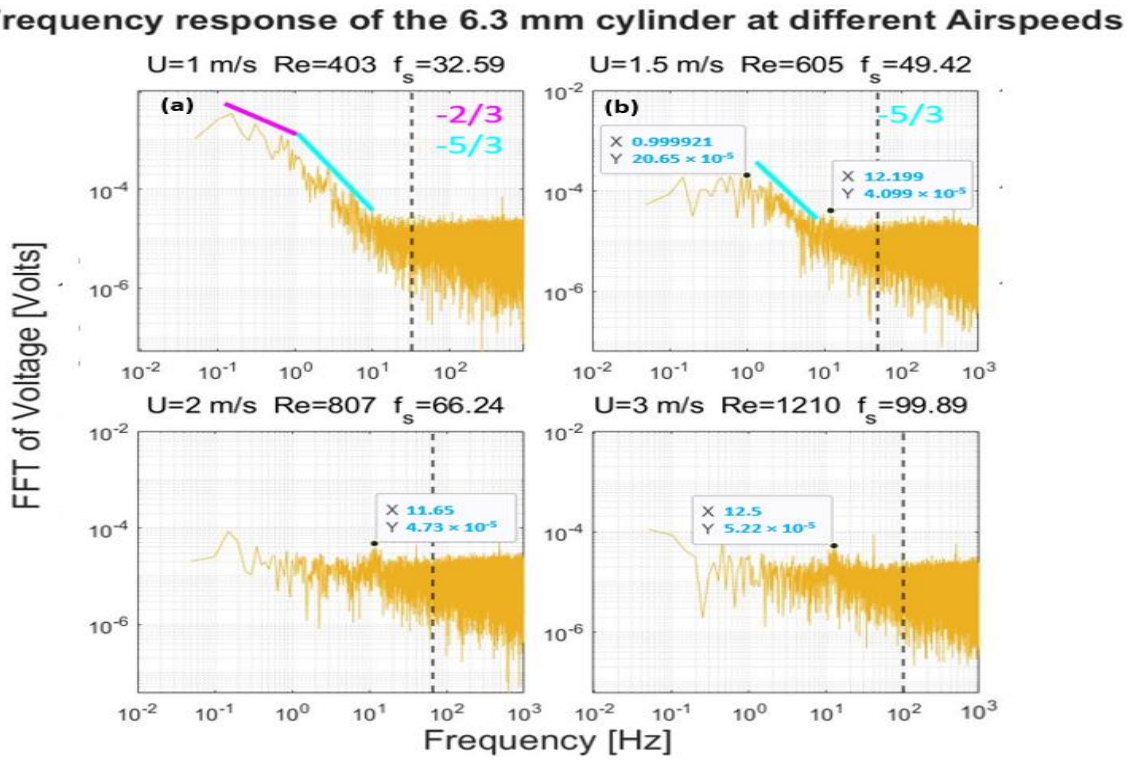

Figure 5.26 Frequency-response of Cylinder (D), diameter 6.3 mm, at flowspeeds 1–3 m/s in relation to Kolomogorov's Scales

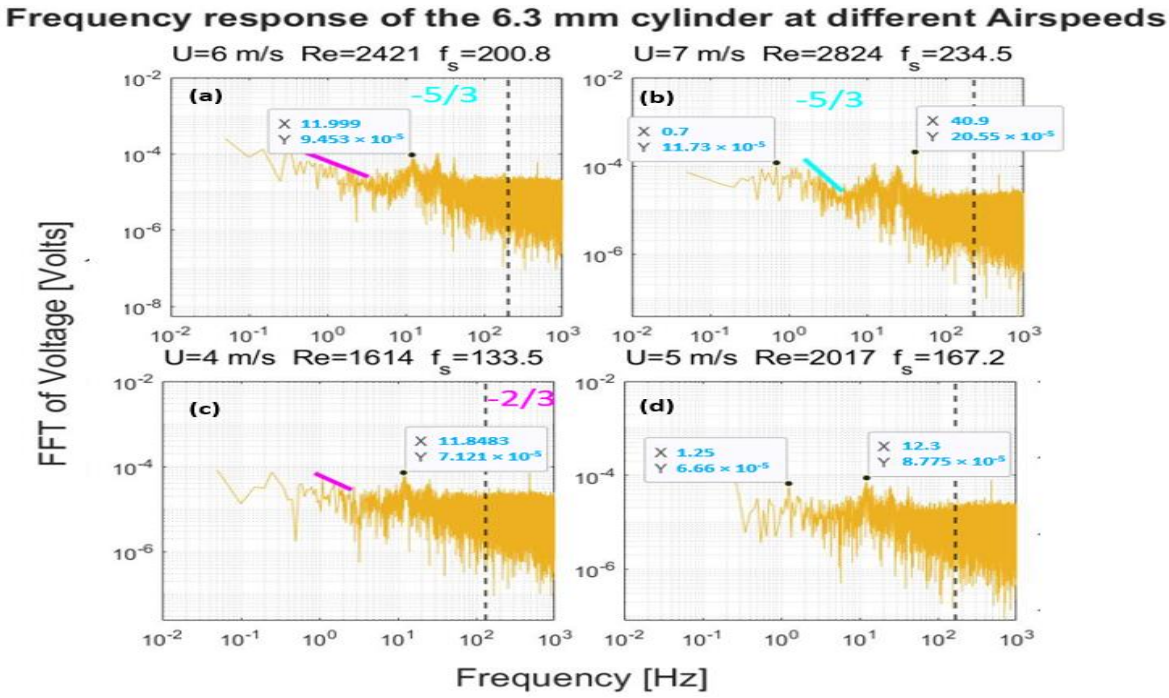

Figure 5.27 Frequency-response of Cylinder (D), diameter 6.3 mm, at flowspeeds 4–7 m/s in relation to Kolomogorov's Scales

5.4.3.2 The mode of turbulence

The agreement in the frequency distribution, as well as the drop in voltage at Reynolds number above 5000, confirm that the measured response of the cylinders is indeed related to the dynamics involved in the fluid flow. Though, the specifically dominant categories of flow instabilities involved in the process remain subject to question. This uncertainty is due to the fact that the frequency-response of the voltage signals agreed with the characteristics of a generally-turbulent flow, but it did not agree with the known frequency-response of the vortex-shedding phenomenon in particular. It was possible to locate voltage peaks at the vortex-shedding frequencies calculated from the literature; however, these peaks were not the strongest in the flow.

The reason behind that could be that vortex shedding was not the main contributor to energy generation in the measurements, contrary to other piezoelectric VIV harvesters that operate on vortex shedding using a cylindrical extension—a non-piezoelectric one. This contradiction may be justified by the fact that the transducer in these harvesters is placed at a certain distance behind the cylindrical extension. This distance allows for the vortices to develop before interacting with the transducer. Therefore, the transducer will have a dominant peak at the shedding frequency.

In the case of the understudy cylinders, the transducer—the cylinder—transduces the vortices effect before the vortices go through their formation length and develop. Moreover, the transducer signal output will be affected by its wake region, contrary to other standard harvesters. Hence, the transducer is mainly affected by the wake-induced vibration of its cylindrical profile rather than vortex shedding.

In addition to the absence of a formation length, another significant observation of these results is the appearance of the system frequencies in the obtained responses. These frequencies are manifested due to the vibration of the relatively-elastic support. Therefore, it can be expected that the process under study has involved some flutter effect. Nevertheless, these peaks have obtained their energy totally from the flow since there was not any external excitation. In other words, the appearance of these peaks does not criticise the cylinders as an energy harvester. It would definitely criticise it—with its current elastic support—as a VIV sensor, which is outside the scope of this work. Careful designing of the support may allow the use of the cylinders as sensors, though.

5.5 Closed-circuit Measurements:

5.5.1 Methods:

Closed-circuit measurements were performed on Cylinders (A) and (C) of diameters 40 and 10 mm, respectively. Each cylinder was tested at several windspeeds in the range of 1–7 m/s in steps of 1 m/s. The electrical circuit was composed of the cylinder, as an energy source, connected to a load resistor. At each windspeed, four different resistors were considered of values: 200, 400, 600, and 800 kΩ. The voltage generated over the load was measured using oscilloscope MSO-X 3054 A, the same device used before. The measured signal spanned for ten seconds with a temporal resolution of 0.00016 seconds. It is worth mentioning that in this set of measurements, the load was directly connected to the cylinder without using the rectification bridge used in the AEH measurements. Therefore, the root-mean-square V_{rms} of the voltage signal was more convenient for calculating the harvested power. The root-mean-square value was calculated for each measured signal, and was used to calculate the power, P, dissipated across the resistance, R, using equation (5.8) .

$$P = \frac{V_{rms}^2}{R} \tag{5.8}$$

5.5.2 Results:

Figure 5.28 and Figure 5.29 show 3D bar diagrams describing the variation of the root-mean-squared voltage from the 40 and the 10 mm cylinders, respectively, across both the load resistance and the windspeed. By comparing the two figures, it can be noticed that the 40 mm cylinder has generally generated a higher voltage than the 10 mm cylinder. Figure 5.28 shows that the 40 mm cylinder has generated a maximum voltage of 13.6 mV at a speed of 7 m/s and a load resistance of 600 kΩ, while the 10 mm cylinder has generated a maximum voltage of 9.24 mV at a speed of 1 m/s and a load resistance of 800 kΩ as shown in Figure 5.29.

By studying Figure 5.28, it can be noticed that the windspeed had different effects on the voltage at different load resistance. Its effect was the strongest at load resistance of 600 kΩ, while it was the weakest at load resistance of 200 kΩ. Moreover, the trend of voltage across windspeed changed from one load resistance to another. At load resistance of 800 kΩ, the voltage had a growing trend across windspeed—This was the expected trend as it corresponds to the increase in kinetic energy with the increase in windspeed—However, the trend was much different at other load resistances. At load resistance of 600 kΩ, the voltage had two peaks at windspeed of 1 and 7 m/s. At resistance 400 kΩ and 200 kΩ, the voltage trend was more random across the windspeed.

In Figure 5.29, there was no clear trend from the 10 mm cylinder voltage across windspeed at any of the load resistances. Moreover, it can be noticed that the 400 and 600 kΩ load resistances gave remarkably less voltage than the 200 and 800 kΩ loads.

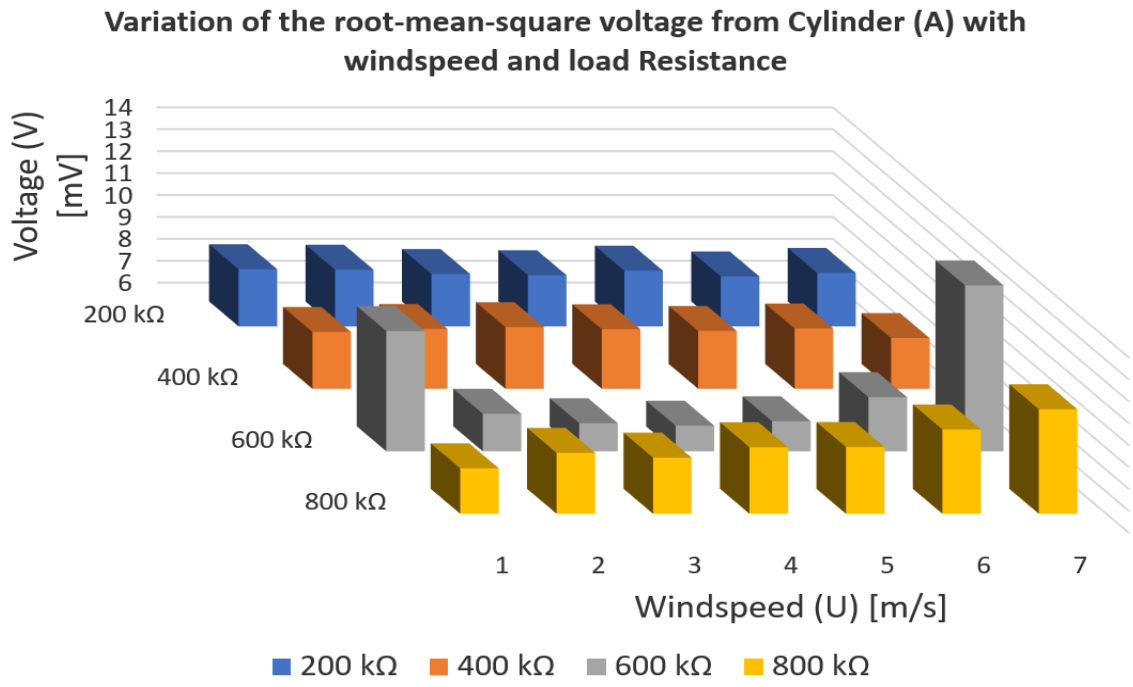

Figure 5.28 Root-mean-squared voltage generated by Cylinder (A), diameter 40 mm, versus windspeed U and load resistance R.

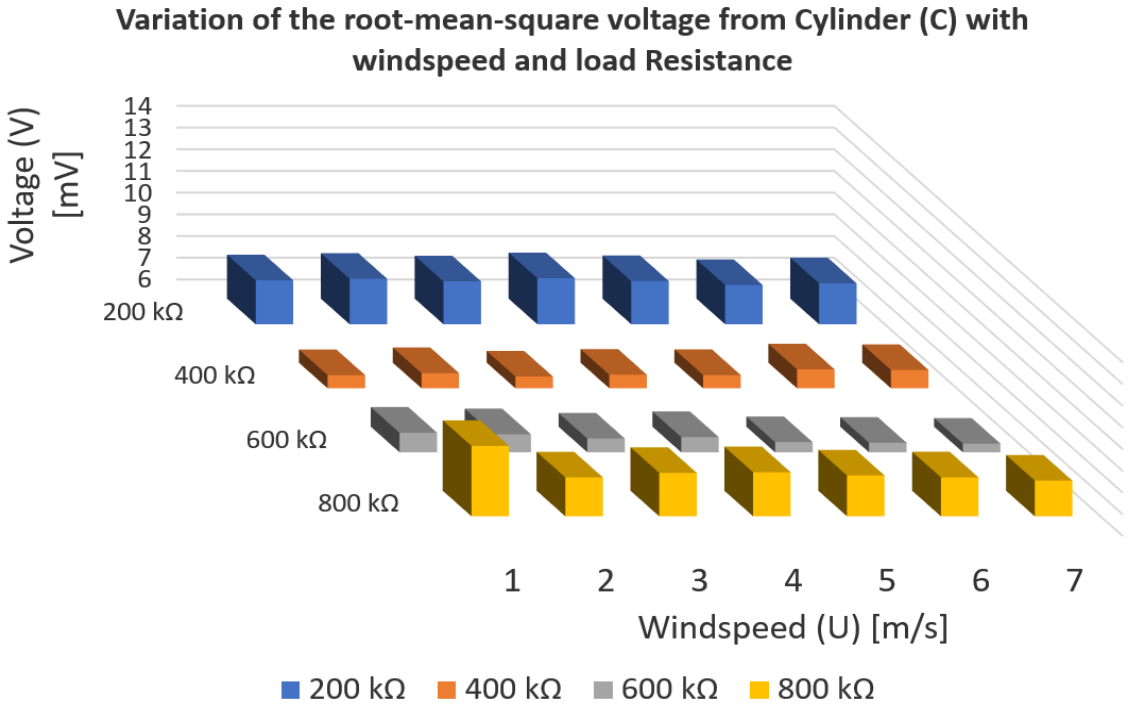

Figure 5.29 Root-mean-squared voltage generated by Cylinder (C), diameter 10 mm, versus windspeed U and load resistance R

Figure 5.30 and Figure 5.31 show 3D bar diagrams describing the variation of the power from the 40 and the 10 mm cylinders respectively across both the load resistance and the wind speed. From the two figures, it can be noticed that the 40 mm cylinder has generated more power—370.6 pW—than the 10 mm cylinder—329.7 pW. The maximum power from the 40 mm cylinder was generated at a windspeed of 1 m/s and load resistance of 200 kΩ, while the maximum power from the 10 mm cylinder was generated at windspeed of 4 m/s and a load of 200 kΩ. Finally, it can be noticed from the two figures that both the cylinders have generated remarkably higher power at a load of 200 kΩ regardless of the windspeed.

It can be seen in Figure 5.30 that the windspeed effect on the generated power from the 40 mm cylinder is similar to that of the voltage presented in Figure 5.28. The power tended to increase with the increase in the windspeed at a load resistance of 800 kΩ, which agrees with the trend of kinetic energy. At load resistance of 600 kΩ, however, the power had two peaks at speeds of 1 and 7 m/s, while it was more random at loads 400 and 200 kΩ.

In Figure 5.31, the 10 mm cylinder generated power, also similar to the voltage trend, did not have a clear trend at any of the load resistances. However,—contrary to voltage— the power was remarkably higher at load resistance of 200 kΩ only.

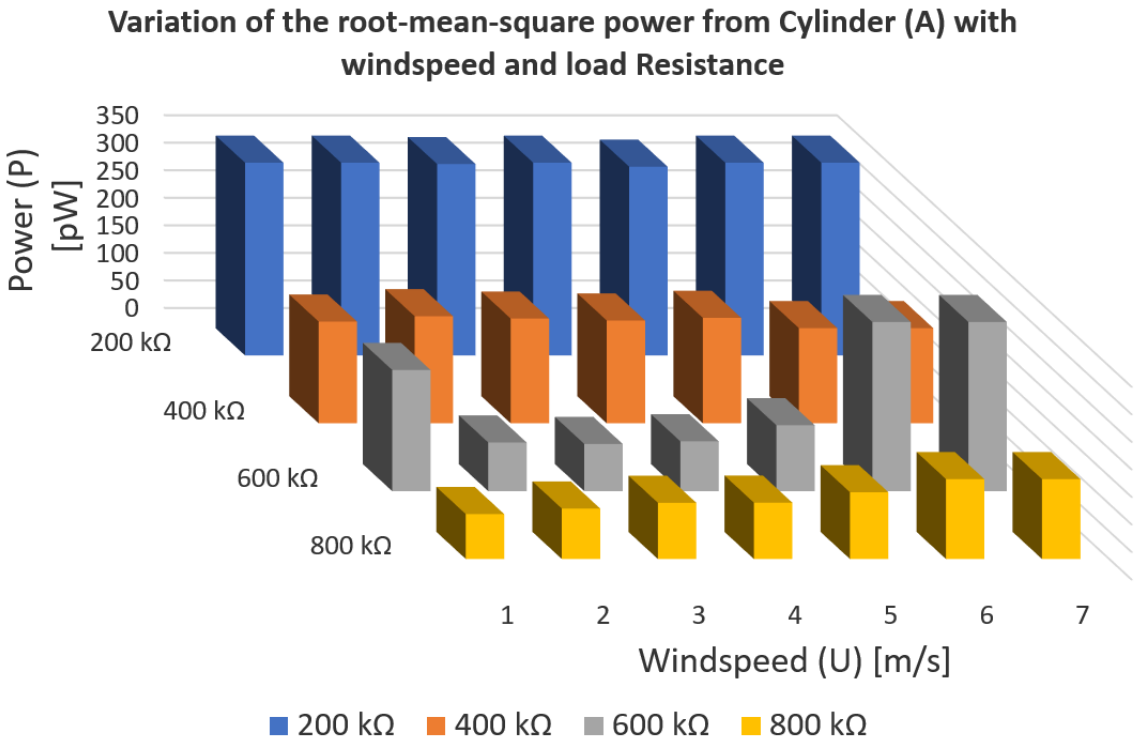

Figure 5.30 Root-mean-squared power generated by Cylinder (A), diameter 40 mm, versus windspeed U and load resistance R

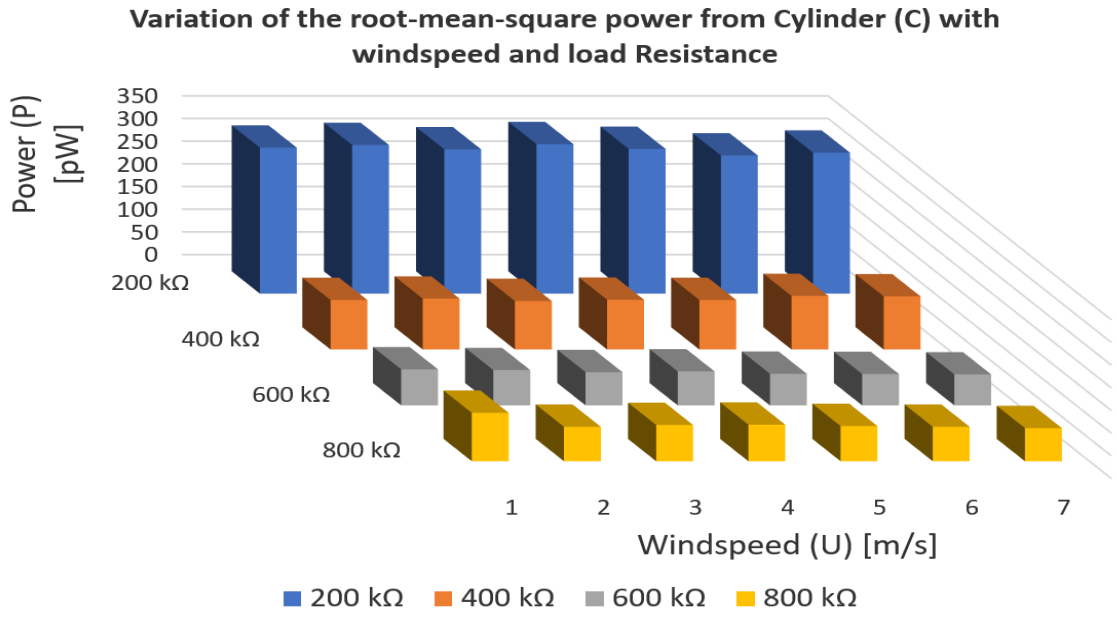

Figure 5.31 Root-mean-squared power generated by Cylinder (C), diameter 10 mm, versus windspeed U and load resistance R

5.5.3 Discussion

For better visualization of the effect of the windspeed on energy harvesting, the power data from Figure 5.30 and Figure 5.31 are plotted in Figure 5.32, where the bigger marker refers to the bigger cylinder. As was previously mentioned, it can be noticed that there is no proportionality between the amount of the harvested power and the windspeed. The absence of such proportionality disagrees with the relation between the kinetic power of a flow and its windspeed, where the kinetic power is proportional to the third power of the windspeed.

The absence of proportionality can be justified by the effect of the ratio between the load impedance and the impedance of the transducer itself on the transfer of power from the cylinder to the load. For an optimized power transfer, the ratio should equal one. However, the impedance of the cylinder depends on the frequency of the acting loads. Since the frequency of vortex shedding in the flow, i.e. the acting loads, depends on the windspeed, therefore the measurements performed at different windspeeds involved energy harvesting with different values of impedance ratio, even though it was at the same load resistance.

Moreover, it can be noticed from Figure 5.32 that the 40 mm cylinder has generated more power than the 10 mm cylinder at all the resistances. However, it is important to consider that the bigger size of the 40 mm cylinder shall give it the advantage for more power generation. Therefore, the harvesting density, ρ, has been defined as the amount of electric

power generated per unit surface area, A_{cyl}, of the transducer as was previously defined in (4.9) for the AEH.

Figure 5.33 shows the variation of the harvesting density of the two cylinders over windspeed at different resistances. By studying Figure 5.33, it can be noticed that the 10 mm cylinder has harvested energy with a higher harvesting density than the 40 mm cylinder, even though it harvested less total power. The 10 mm cylinder has achieved a remarkably high harvesting density of 35 pW/cm^2 at a windspeed of 4 m/s and a load of 200 kΩ, while the 40 mm cylinder has achieved harvesting density of 7.4 pW/cm^2 at a windspeed of 1 m/s and a load of 200 kΩ.

Finally, it was evident from Figure 5.32 that the two cylinders have given their maximum power at the smallest resistance, 200 kΩ. Such a fact may indicate that resistances smaller than 200 kΩ may give better performance. In fact, the difference between the 200 kΩ and the 400 kΩ in the case of the 10 mm cylinder is much larger than that in the case of the 40 mm cylinder. This may indicate that the 10 mm cylinder is more off-tune than the 40 mm cylinder. This means that there is a wide space for improvement for the 10 mm cylinder in a way that allows for significant improvement in its already high harvesting density, ρ. Therefore, it would be quite beneficial to expand the measurements to smaller electric loads for the two cylinders in order to harvest more power.

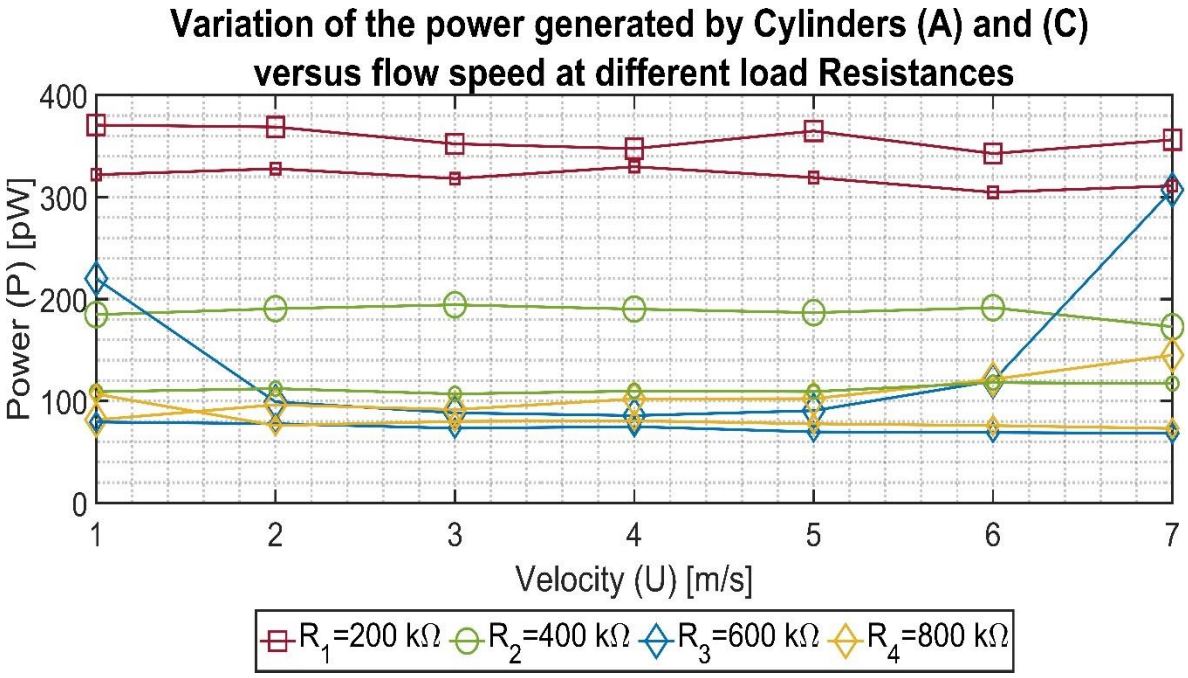

Figure 5.32 A comparison of the power, P, harvested by Cylinders (A) and (C). Lines plotted with a bigger marker refer to the bigger cylinder, Cylinder (A) of a diameter of 40 mm.

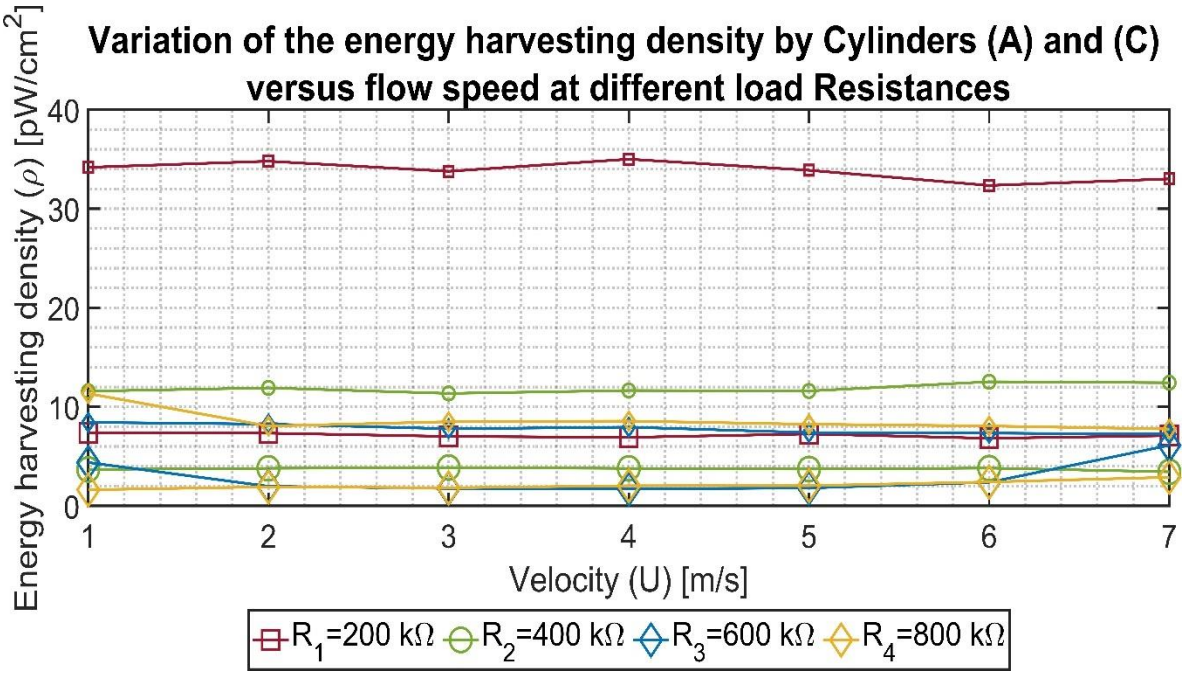

Figure 5.33 A comparison of the harvesting density, ρ, by Cylinders (A) and (C). Lines plotted with a bigger marker refer to the bigger cylinder, Cylinder (A) of a diameter of 40 mm.

6 Conclusion

Piezoelectric materials have been extensively used in the literature as transducers inside energy harvesters. However, cylindrical piezoelectric transducers have seldom been studied. The goals of this research have been successfully met as it has managed to study the potential of cylindrical piezoelectric transducers for energy harvesting. The research has considered both acoustic energy harvesting and flow-induced vibration harvesting, where it was possible to meet the goals specified in each topic.

Regarding acoustic energy harvesting, it was possible to meet the three specified goals, where a piezoelectric cylinder was used to construct an energy harvester. The impedance of the transducer was studied, which facilitated optimization of the harvester by performing the necessary impedance matching. Thanks to the impedance-matched circuit, it was possible to harvest 67.6 μW from sound waves of 20 kHz frequency. The efficiency of the harvesting process was 86.1%, which was comparable to other values reported in the literature. The proposed harvester had an energy harvesting density of 1.3455 $\mu W/cm^2$. Moreover, referencing the produced power to the volume of the harvester and the sound pressure, the proposed harvester outperformed other acoustic energy harvesters reported in the literature.

Finally, it was believed that there was a relation between the wavelength of sound waves and the size of the harvester. This relation was established based on measurements performed on the largest available cylinder; however, larger cylinders would be necessary to confirm the established relation.

The results found in this research may lay the road for more sophisticated designs of energy harvesters that exploit the cylindrical geometry to capture, amplify, and harvest the sound in a volume-efficient manner. Thanks to their volume efficiency, such harvesters will be of great use in the Micro-Electro-Mechanical-Sytems, which operate in inaccessible environments with space limitations.

In addition to acoustic energy harvesting, the cylinders were studied for harvesting flow-induced vibration. The response of the cylinders to the flow-induced vibrations was studied at a Reynolds number range of 403–17931 using open–circuit measurements. It was possible to relate the electric response of the cylinders to the fluid behaviour through two observations. First, it was found that the generated voltage significantly drops at Reynolds number above 5000, while independent research has also measured that the vortex-shedding quality significantly drops at Reynolds number above 5000. Second, it was observed that the frequency spectrum of the generated voltage is distributed across its frequency according to a power law of order of negative five-thirds. Such distribution agrees with the distribution of the energy spectrum of the turbulence energy of a turbulent flow across its wave number. The agreement in the frequency distribution, as well as the drop in voltage at Reynolds number above 5000, confirm that the measured response of the

cylinders is indeed related to the dynamics involved in the fluid flow. Though, the specifically dominant categories of flow instabilities involved in the process remain subject to question. This uncertainty is due to the fact that the frequency-response of the voltage signals agreed with the characteristics of a generally-turbulent flow, but it did not agree with the known frequency-response of the vortex-shedding phenomenon in particular. It was possible to locate voltage peaks at the vortex-shedding frequencies calculated from the literature; however, these peaks were not the strongest in the flow. This is believed to be due to the absence of a vortex-formation length over which the vortices can well develop before they are harvested. Moreover, it is believed to be due to a flutter effect from the elastic support, as the natural frequencies of the cylinder mounting structure were manifested in the cylinders' response. Such limitations would be critical if the cylinders—with their current support structure—are to be used as sensors; however, these limitations would not be problematic for energy harvesting.

From the point of view of energy harvesting, energy harvesting was carried out using closed-circuit measurements on two of the four sizes inside a wind tunnel at wind speeds of 1–7 m/s and load resistances of 200–800 kΩ. It was found that the highest power was generated at the smallest load resistance in the case of both cylinders. Better-designed load circuits could enhance the quality of energy harvesting.

The obtained results from the open-circuit measurement may lay the road toward using cylindrical piezoelectric transducers in the design of pressure sensors devoted to the study of flows across circular cylinders. Moreover, the closed-circuit measurements may provide guidelines for designers of flow-induced vibration harvesters. Finally, this research, with its two parts, acoustic energy harvesting and flow-induced vibration harvesting, confirms the possibility of employing smart materials for energy harvesting. Such a promising technology can significantly reduce energy consumption and raise the autonomy of machines.

7 Future Work

The thesis has tackled two forms of energy harvesting using piezoelectric transducers: Acoustic energy harvesting and FIV harvesting.

In acoustic energy harvesting:

Since it was found that the quality of energy harvesting was improved with the increase in sound frequency, it is believed that the proposed transducers shall be a suitable candidate for ultrasonic energy harvesting. Therefore, it is recommended to expand this work beyond the limit of acoustic frequencies and to use ultrasonic waves.

Moreover, the cylindrical transducer could be used in different configurations rather than radial subjection to sound waves. It might be interesting to apply sound waves in an axial direction to the cylinder. In such a case, sound waves may be trapped inside the cylinder, magnifying the harvesting effect.

In Flow-Induced Vibration harvesting:

This thesis has discussed the harvesting of energy from Flow-induced vibrations using open-circuit and closed-circuit experiments performed inside a wind tunnel. The open-circuit experiments have shown how the piezoelectric cylinder interacts with the instabilities in the flow. It would be interesting if other teams performed this study using flow imaging techniques such as Particle Image Velocimetry—PIV—in order to visualize the flow dynamics during the process. By using such a coupled study, it would be possible to correlate each electric behaviour of the cylinder to its causing flow instability. However, such work may lie outside of the specific scope of this research which is energy harvesting.

In addition to open-circuit measurements, closed-circuit measurements were carried out using different load resistances in the range of 200–800 kΩ. It was found that power harvesting was maximized at the smallest load resistance among the four. Therefore, It would be quite interesting to extend this measurement to lower load resistances and find the optimum operating load resistance. Moreover, with more information on the frequencies available in the flow thanks to the flow-imaging techniques, it would be beneficial to give more attention to establishing broadband-frequency impedance matching. Such an improvement is expected to significantly increase the harvested power.

In addition to the previous points, it would be interesting to push the study towards flows of a lower Reynolds number. The minimum Reynolds number involved in these measurements was 403, which is not low enough to establish a clear vortex-shedding regime—vortex shedding starts from a Reynolds number of 40—vortex shedding starts from a Reynolds number of 40. Therefore, using a wind tunnel of a lower minimum wind speed would be quite beneficial as it lowers the minimum Reynolds number in the study as well as allows a wider range of Reynolds number to be obtained from the same cylinder.

It might be recommended to use a wind tunnel with special design considerations regarding its power electronics in order to reduce the amount of the ambient electric field. It might be interesting to consider a different solution where the cylinder is moved linearly in ambient air using a pneumatic cylinder. In such a configuration, the cylinder would be moving instead of air to avoid the need for high-power equipment that may generate an undesired electric field. Such a mechanism may help achieve a lower Reynolds number since the lower limit in these measurements was determined by the wind tunnel specifications.

Finally, it would be interesting to perform this study on multiple cylinders in tandem. Such a study would look at the maximum number of cylinders to be fitted in a unit space in order to magnify the harvested power in a trend proportional to the number of cylinders.

References

[1] ROBERTS, Owain T. P. Wind-power and the boats from the Cyclades. *International Journal of Nautical Archaeology* [online]. 1987, **16**(4), 309–311. ISSN 10572414, 10959270. available at: doi:10.1111/j.1095-9270.1987.tb00605.x

[2] GASCH, Robert a Jochen TWELE. Historical development of windmills. In: Robert GASCH a Jochen TWELE, ed. *Wind Power Plants* [online]. Berlin, Heidelberg: Springer Berlin Heidelberg, 2012 [vid. 2022-07-20], s. 15–45. ISBN 978-3-642-22937-4. available at: doi:10.1007/978-3-642-22938-1_2

[3] PASSCHIER, Cees W., Marcel BOURGEOIS, Pierre-Louis VIOLLET, Gül SÜRMELIHINDI, Vincent BERNARD, Philippe LEVEAU a Christoph SPÖTL. Reconstructing the hydraulics of the world's first industrial complex, the second century CE Barbegal watermills, France. *Scientific Reports* [online]. 2020, **10**(1), 17917. ISSN 2045-2322. available at: doi:10.1038/s41598-020-74900-5

[4] TRAN, Le-Giang, Hyouk-Kyu CHA a Woo-Tae PARK. RF power harvesting: a review on designing methodologies and applications. *Micro and Nano Systems Letters* [online]. 2017, **5**(1), 14. ISSN 2213-9621. available at: doi:10.1186/s40486-017-0051-0

[5] SALEM, Shehab, Karel FRANA, Iva NOVA a Jiri ERHART. Acoustic Energy Harvesting Using Piezo-Electric Materials. In: *2020 International Youth Conference on Radio Electronics, Electrical and Power Engineering (REEPE)* [online]. Moscow, Russia: IEEE, 2020, s. 1–6 [vid. 2022-01-07]. ISBN 978-1-72815-655-2. available at: doi:10.1109/REEPE49198.2020.9059190

[6] HASSAN, Haris Fazilah, Syed Idris Syed HASSAN a Rosemizi ABD RAHIM. Acoustic Energy Harvesting Using Piezoelectric Generator for Low Frequency Sound Waves Energy Conversion. *International Journal of Engineering and Technology (IJET)*. 2013, **5**(6), 4702–4707. ISSN 0975-4024.

[7] MONROE, Nathan M a Jeffrey H LANG. Broadband, Large Scale Acoustic Energy Harvesting via Synthesized Electrical Load: Part I. Harvester Design and Model. *Smart Materials and Structures* [online]. 2019, **28**(5) [vid. 2022-07-06]. ISSN 1361-665X. available at: doi:10.1088/1361-665X/ab114a

[8] DROSSEL, W, H KUNZE, A BUCHTE, l WEISHEIT a K PAGEL. CIRP 25th Design Conference Innovative Product Creation. In: *Smart Materials for Smart Applications* [online]. 2015, s. 211–216. available at: doi:10.1016/j.procir.2015.01.055

[9] D. MICHELLE ADDINGTON a DANIEL L. SCHODEK. *Smart Materials and Technologies For the Architecture and Design Professions*. Oxford: Architectural Press, 2004. ISBN 0-7506-6225-5.

[10] HAKAMI, Abdullatif, Sesha S. SRINIVASAN, Prasanta K. BISWAS, Ashwini KRISHNEGOWDA, Scott L. WALLEN a Elias K. STEFANAKOS. Review on thermochromic materials: development, characterization, and applications. *Journal of Coatings Technology and Research* [online]. 2022, **19**(2), 377–402. ISSN 1547-0091, 1935-3804. available at: doi:10.1007/s11998-021-00558-x

[11] RAI, Varun, Ram Sevak SINGH, Daniel John BLACKWOOD a Dong ZHILI. A Review on Recent Advances in Electrochromic Devices: A Material Approach. *Advanced Engineering Materials* [online]. 2020, **22**(8), 2000082. ISSN 1438-1656, 1527-2648. available at: doi:10.1002/adem.202000082

[12] DE SOUSA, Frederico B., Frank ALEXIS a Silvia GIORDANI. Editorial: Photochromic Materials: Design and Applications. *Frontiers in Materials* [online]. 2021, **8**, 720172. ISSN 2296-8016. available at: doi:10.3389/fmats.2021.720172

[13] KIM, Heung Soo, Joo-hyong KIM a Jaehwan KIM. A Review of Piezoelectric Energy Harvesting Based on Vibration [online]. 2011, (November 2014). available at: doi:10.1007/s12541-011-0151-3

[14] DINEVA, P.S, D GROSS, MULLERR a T RANGELOV. *Dynamic Fracture of Piezoelectric Materials* [online]. 1. vyd. B.m.: Springer International Publishing, 2014. ISBN 9783319039619. available at: doi:10.1007/978-3-319-03961-9

[15] M., Ramar a S. BALASUBRAMANIAN. Development of Piezoelectric property materials for the Nanogenerator production. *Research Journal of Chemical and Environmental Sciences*. 2018, **6**(1), 114–123. ISSN 2321-1040.

[16] SALEM, Shehab, Karel FRAŇA a Iva NOVÁ. The Potential of Cylindrical Piezoelectric Transducers for High-Frequency Acoustic Energy Harvesting. *Energies* [online]. 2021, **14**(18), 5845. ISSN 1996-1073. available at: doi:10.3390/en14185845

[17] DAHIYA, Ravinder S. a Maurizio VALLE. *Robotic Tactile Sensing* [online]. 1. vyd. B.m.: Springer Netherlands, 2013. ISBN 978-94-007-9963-9. available at: doi:10.1007/978-94-007-0579-1

[18] Introduction. In: *Ceramic Materials* [online]. New York, NY: Springer New York, 2007 [vid. 2022-07-17], s. 3–14. ISBN 978-0-387-46270-7. available at: doi:10.1007/978-0-387-46271-4_1

[19] HAN, Baoguo, Xun YU a Jinping OU. *Self-sensing concrete in smart structures*. Amsterdam ; Boston: Butterworth-Heinemann is an imprint of Elsevier, 2014. ISBN 978-0-12-800517-0.

[20] ZHU, Xinhua. *Piezoelectric ceramic materials: Processing, properties, characterization, and applications*. B.m.: Nova Science Publishers, 2010. ISBN 1-61668-418-6.

[21] MISHRA, Suvrajyoti, Lakshmi UNNIKRISHNAN, Sanjay Kumar NAYAK a Smita MOHANTY. Advances in Piezoelectric Polymer Composites for Energy Harvesting Applications: A Systematic Review. *Macromolecular Materials and Engineering* [online]. 2019, **304**(1), 1800463. ISSN 14387492. available at: doi:10.1002/mame.201800463

[22] SAFARI, A, G SA-GONG, J GINIEWICZ a R E NEWNHAM. COMPOSITE PIEZOELECTRIC SENSORS. In: *Tailoring Multiphase and Composite Ceramics.* Boston, MA.: Springer, 1986, s. 2. ISBN 978-1-4612-9309-5.

[23] WATTHAGE, SUNETH C., SONG, ZHAONING, PHILLIPS, ADAM B., a HEBEN, MICHAEL J. Evolution of Perovskite Solar Cells. In: *Perovskite Photovoltaics. Basic to Advanced Concepts and Implementation*. B.m.: Academic Press, 2018, s. 43–88. ISBN 978-0-12-812915-9.

[24] FLEMING, Andrew J. a S. O. Reza MOHEIMANI. Fundamentals of Piezoelectricity. In: *Piezoelectric Transducers for Vibration Control and Damping* [online]. London: Springer, 2006, s. Springer, London. ISBN 978-1-84628-332-1. available at: doi:DOI https://doi.org/10.1007/1-84628-332-9

[25] TICHÝ, Jan, Jiří ERHART, Erwin KITTINGER a Jana PŘÍVRATSKÁ. *Fundamentals of Piezoelectric Sensorics* [online]. Berlin, Heidelberg: Springer Berlin Heidelberg, 2010 [vid. 2022-07-23]. ISBN 978-3-540-43966-0. available at: doi:10.1007/978-3-540-68427-5

[26] HONG, Chang-hyo, Hwang-pill KIM, Byung-yul CHOI, Hyoung-su HAN, Jae SUNG, Chang WON a Wook JO. Lead-free piezoceramics e Where to move on ? *J Materiomics* [online]. 2016, **2**(1), 1–24. ISSN 2352-8478. available at: doi:10.1016/j.jmat.2015.12.002

[27] HALES, Alastair a Xi JIANG. A review of piezoelectric fans for low energy cooling of power electronics. *Applied Energy* [online]. 2018, **215**(December 2017), 321–337. ISSN 0306-2619. available at: doi:10.1016/j.apenergy.2018.02.014

[28] QING, Xinlin, Wenzhuo LI, Yishou WANG a Hu SUN. Piezoelectric Transducer-Based Structural Health. *Sensors* [online]. 2019, **19**, 1–27. available at: doi:10.3390/s19030545

[29] JI, Qing, Zhi DING, Ning WANG a Miao PAN. A Novel Waveform Optimization Scheme for Piezoelectric Sensors Wire-Free Charging in the Tightly Insulated Environment. *IEEE Internet of Things*. 2018, **5**(3), 1936–1946.

[30] HARRISON, J S a Z OUNAIES. *PIEZOELECTRIC POLYMERS*. Hampton, Virginia: NASA Langley Research Center. 2001.

[31] JING-FENG, Li. Fundamentals of Piezoelectricity. In: *Lead-Free Piezoelectric Materials*. B.m.: Wiley-VCH, nedatováno, s. 18. ISBN 978-3-527-34512-0.

[32] FAN, Yu, Manuel COLLET, Mohamed ICHCHOU a Olivier BAREILLE. Wave Electromechanical Coupling Factor for the Guided Waves in Piezoelectric Composites. *Materials* [online]. 2018, 1–21. available at: doi:10.3390/ma11081406

[33] SAADON, Salem a Othman SIDEK. A review of vibration-based MEMS piezoelectric energy harvesters. *Energy Conversion and Management* [online]. 2011, **52**(1), 500–504. ISSN 0196-8904. available at: doi:10.1016/j.enconman.2010.07.024

[34] RÖSLER, Joachim, Harald HARDERS a Martin BÄKER. *Mechanical Behaviour of Engineering Materials Metals, Ceramics, Polymers, and Composites*. 2. vyd. Berlin: Springer, 2006. Lehrbuch Maschinenbau. ISBN 978-3-8351-0008-4.

[35] MANDAL, Subrata Kr a A MAITY. Smart materials - scopes and prospects. *Elixir Mech. Engg*. 2013, **65**(2013), 20154–20163.

[36] SHERRIT, Stewart a Binu K. MUKHERJEE. Characterization of Piezoelectric Materials for Transducers. *Dielectric and Ferroelectric Reviews* [online]. nedatováno, **2012**, 175–244. available at: doi:10.48550/ARXIV.0711.2657

[37] JABBAR, Hamid, Hyun Jun JUNG, Nan CHEN, Dae Heung CHO a Tae Hyun SUNG. Piezoelectric energy harvester impedance matching using a piezoelectric transformer. *Sensors and Actuators A: Physical* [online]. 2017, **264**, 141–150. ISSN 09244247. available at: doi:10.1016/j.sna.2017.07.036

[38] KIM, Hyeoungwoo, Shashank PRIYA a Kenji UCHINO. Modeling of Piezoelectric Energy Harvesting Using Cymbal Transducers. *Japanese Journal of Applied Physics* [online]. 2006, **45**(7), 5836–5840. ISSN 0021-4922, 1347-4065. available at: doi:10.1143/JJAP.45.5836

[39] HAN, Peng, Qiaogao HUANG, Guang PAN, Wei WANG, Tianqi ZHANG a Denghui QIN. Energy harvesting from flow-induced vibration of a low-mass square cylinder with different incidence angles. *AIP Advances* [online]. 2021, **11**(2), 025126. ISSN 2158-3226. available at: doi:10.1063/5.0037071

[40] SALEM, Shehab a Karel FRAŇA. A Wind Tunnel Study of the Flow-Induced Vibrations of a Cylindrical Piezoelectric Transducer. *Sensors* [online]. 2022, **22**(9), 3463. ISSN 1424-8220. available at: doi:10.3390/s22093463***)***

[41] CHEN, Yu, Xiaojing MU, Tao WANG, Weiwei REN, Ya YANG, Zhong Lin WANG, Chengliang SUN a Alex Yuandong GU. Flutter Phenomenon in Flow Driven Energy

Harvester–A Unified Theoretical Model for “Stiff” and “Flexible” Materials. *Scientific Reports* [online]. 2016, **6**(1), 35180. ISSN 2045-2322. available at: doi:10.1038/srep35180

[42] WEN, Quan, Xianming HE, Zhuang LU, Reinhard STREITER a Thomas OTTO. A comprehensive review of miniatured wind energy harvesters. *Nano Materials Science* [online]. 2021, **3**(2), 170–185. ISSN 25899651. available at: doi:10.1016/j.nanoms.2021.04.001

[43] WILLIAMSON, C H K. Vortex Dynamics in the Cylinder Wake. *Annual Reviews of Fluid Mechanics*. 1996, **28**, 477–539.

[44] SALEM, Shehab, Karel FRANA a Sylvio SIMON. Experimental and Numerical Study of the Aero-Acoustics of Flow over Structured Sheet Metals. In: *2021 25th International Conference on Circuits, Systems, Communications and Computers (CSCC)* [online]. Crete Island, Greece: IEEE, 2021, s. 26–36 [vid. 2022-01-31]. ISBN 978-1-66542-749-4. available at: doi:10.1109/CSCC53858.2021.00013

[45] AHLBORN, Boye, Mae L SETO a Bernd R NOACK. On drag, Strouhal number and vortex-street structure. *Fluid Dynamics Research* [online]. 2002, **30**(6), 379–399. available at: doi:10.1016/S0169-5983(02)00062-X

[46] SALEM, Shehab, Karel FRAŇA a Iva NOVÁ. Design of Acoustic Energy Harvesting Unit Using Piezo-Electric Diaphragm. *Materials Science Forum* [online]. 2020, **986**, 109–115. ISSN 1662-9752. available at: doi:10.4028/www.scientific.net/MSF.986.109

[47] ZUO, Lei a Xiudong TANG. Large-scale vibration energy harvesting. *Journal of Intelligent Material Systems and Structures* [online]. 2013, **24**(11), 1405–1430. ISSN 1045-389X, 1530-8138. available at: doi:10.1177/1045389X13486707

[48] WANG, Hao a Abbas JASIM. Piezoelectric energy harvesting from pavement. In: *Eco-Efficient Pavement Construction Materials* [online]. B.m.: Elsevier, 2020 [vid. 2022-07-22], s. 367–382. ISBN 978-0-12-818981-8. available at: doi:10.1016/B978-0-12-818981-8.00014-X

[49] NOH, Hee-min. Acoustic energy harvesting using piezoelectric generator for railway environmental noise. *Advances in Mechanical Engineering* [online]. 2018, **10**(7), 1–9. available at: doi:10.1177/1687814018785058

[50] MONROE, Nathan M. Broadband Acoustic Energy Harvesting Via Synthesized Electrical Loading by. 2017, (2013), 1–149.

[51] YUAN, Ming, Xiaohui WANG a Zhenjun DING. Low frequency acoustic energy harvesting adopting slit Helmholtz resonator. *Vibroengineering PROCEDIA* [online].

2018, **20**, 151–155. ISSN 2345-0533, 2538-8479. available at: doi:10.21595/vp.2018.20245

[52] CHEN, Khin Fai, Jee-hou HO a Eng Hwa YAP. Piezoelectric Approach on Harvesting Acoustic Energy. *International Journal of Energy and Power Engineering*. 2015, **9**(8), 774–780.

[53] KHAN, Farid a IZHAR. Piezoelectric type acoustic energy harvester with a tapered Helmholtz cavity for improved performance. *Journal of Renewable and Sustainable Energy* [online]. 2016, **8**(5), 054701. ISSN 1941-7012. available at: doi:10.1063/1.4962027

[54] YANG, Zhengbao a Jean ZU. On the efficiency of piezoelectric energy harvesters. *Extreme Mechanics Letters* [online]. 2017, **15**. available at: doi:10.1016/j.eml.2017.05.002

[55] RICHARDS, Cecilia, Michael ANDERSON, David BAHR a Robert RICHARDS. Efficiency of Energy Conversion for Devices Containing a Piezoelectric Component. *Journal of Micromechanics and Microengineering* [online]. 2004, **14**, 717. available at: doi:10.1088/0960-1317/14/5/009

[56] SHU, Yi-Chung a I LIEN. Analysis of power output for piezoelectric energy harvesting systems. *Smart Materials and Structures* [online]. 2006, **15**, 1499. available at: doi:10.1088/0964-1726/15/6/001

[57] LIAO, Yabin a Henry SODANO. Structural Effects and Energy Conversion Efficiency of Power Harvesting. *Journal of Intelligent Material Systems and Structures - J INTEL MAT SYST STRUCT* [online]. 2009, **20**, 505–514. available at: doi:10.1177/1045389X08099468

[58] YUAN, Ming, Ziping CAO, Jun LUO a Xiujian CHOU. Recent Developments of Acoustic Energy Harvesting: A Review. *Micromachines* [online]. 2019, **10**(1), 48. ISSN 2072-666X. available at: doi:10.3390/mi10010048

[59] KISHORE, Ravi Anant a Shashank PRIYA. Piezoelectric wind turbine. In: Kevin M. FARINHOLT a Steven F. GRIFFIN, ed. [online]. 2013, s. 869009 [vid. 2021-11-21]. available at: doi:10.1117/12.2009551

[60] PRIYA, Shashank, Chih-Ta CHEN, Darren FYE a Jeff ZAHND. Piezoelectric Windmill: A Novel Solution to Remote Sensing. *Japanese Journal of Applied Physics* [online]. 2005, **44**(3), L104–L107. ISSN 0021-4922, 1347-4065. available at: doi:10.1143/JJAP.44.L104

[61] CHIH-TA CHEN, R.A. ISLAM a S. PRIYA. Electric energy generator. *IEEE Transactions on Ultrasonics, Ferroelectrics and Frequency Control* [online]. 2006, **53**(3), 656–661. ISSN 0885-3010. available at: doi:10.1109/TUFFC.2006.1610576

[62] KARAMI, M. Amin, Justin R. FARMER a Daniel J. INMAN. Parametrically excited nonlinear piezoelectric compact wind turbine. *Renewable Energy* [online]. 2013, **50**, 977–987. ISSN 09601481. available at: doi:10.1016/j.renene.2012.07.037

[63] ZHAO, Liya a Yaowen YANG. Toward Small-Scale Wind Energy Harvesting: Design, Enhancement, Performance Comparison, and Applicability. *Shock and Vibration* [online]. 2017, **2017**, 1–31. ISSN 1070-9622, 1875-9203. available at: doi:10.1155/2017/3585972

[64] TAYLOR, G.W., J.R. BURNS, S.A. KAMMANN, W.B. POWERS a T.R. WELSH. The Energy Harvesting Eel: a small subsurface ocean/river power generator. *IEEE Journal of Oceanic Engineering* [online]. 2001, **26**(4), 539–547. ISSN 03649059. available at: doi:10.1109/48.972090

[65] ALLEN, J.J. a A.J. SMITS. ENERGY HARVESTING EEL. *Journal of Fluids and Structures* [online]. 2001, **15**(3–4), 629–640. ISSN 08899746. available at: doi:10.1006/jfls.2000.0355

[66] POBERING, Sebastian a Norbert SCHWESINGER. Power supply for wireless sensor systems. In: *2008 IEEE Sensors* [online]. Lecce, Italy: IEEE, 2008, s. 685–688 [vid. 2021-11-29]. ISBN 978-1-4244-2580-8. available at: doi:10.1109/ICSENS.2008.4716534

[67] GAO, Xiaotong, Wei-Heng SHIH a Wan Y. SHIH. Flow Energy Harvesting Using Piezoelectric Cantilevers With Cylindrical Extension. *IEEE Transactions on Industrial Electronics* [online]. 2013, **60**(3), 1116–1118. ISSN 0278-0046, 1557-9948. available at: doi:10.1109/TIE.2012.2187413

[68] LEE, Yin Jen, Yi QI, Guangya ZHOU a Kim Boon LUA. Vortex-induced vibration wind energy harvesting by piezoelectric MEMS device in formation. *Scientific Reports* [online]. 2019, **9**(1), 20404. ISSN 2045-2322. available at: doi:10.1038/s41598-019-56786-0

[69] AKAYDIN, Huseyin Dogus, Niell ELVIN a Yiannis ANDREOPOULOS. Energy Harvesting from Highly Unsteady Fluid Flows using Piezoelectric Materials. *Journal of Intelligent Material Systems and Structures* [online]. 2010, **21**(13), 1263–1278. ISSN 1045-389X, 1530-8138. available at: doi:10.1177/1045389X10366317

[70] XIE, Jiemin, Jiashi YANG, Hongping HU, Yuantai HU a Xuedong CHEN. A piezoelectric energy harvester based on flow-induced flexural vibration of a circular cylinder. *Journal of Intelligent Material Systems and Structures* [online]. 2012, **23**(2), 135–139. ISSN 1045-389X, 1530-8138. available at: doi:10.1177/1045389X11431744

[71] NAKAMURA, Hajime. Vortex Shedding Suppression for a Circular Cylinder by Attaching Cylindrical Rings (A Consideration of the Mechanism) AJK2011-16008 [online]. 2017, (January). available at: doi:10.1115/AJK2011-16008

[72] JABBAR, Hamid, Hyun JUN, Nan CHEN, Dae HEUNG a Tae HYUN. Piezoelectric energy harvester impedance matching using a piezoelectric transformer. *Sensors & Actuators: A. Physical* [online]. 2017, **264**, 141–150. ISSN 0924-4247. available at: doi:10.1016/j.sna.2017.07.036

[73] KHAN, Farid a IZHAR. Electromagnetic energy harvester for harvesting acoustic energy. *Sadhana* [online]. 2016, **41**(4), 397–405. available at: doi:10.1007/s12046-016-0476-9

[74] HOROWITZ, Stephen, Mark SHEPLAK, Louis CATTAFESTA a Toshikazu NISHIDA. A MEMS acoustic energy harvester. *Journal of Micromechanics and Microengineering* [online]. 2006, **16**(9), 13–16. available at: doi:10.1088/0960-1317/16/9/S02

[75] KIM, YONG JOE LI, BIN YOU, Jeong Ho. Low frequency acoustic energy harvesting using PZT piezoelectric plates in a straight tube resonator. *Smart Materials and Structures*. 2013, **22**.

[76] ROSHKO, Anatol. *ON THE DEVELOPMENT OF TURBULENT WAKES FROM VORTEX STREETS* [online]. Technical. 1191. Washington DC: National Advisory Committee for Aeronautics. 1954. available at: https://authors.library.caltech.edu/428/1/ROSnacarpt1191.pdf

[77] NORBERG, Christoffer. LDV-measurements in the near wake of a circular cylinder. In: *1998 ASME Fluids Engineering Division (Annual Summer Meeting)*. Washington DC: American Society of Mechanical Engineers, 1998.

[78] ORTIZ-SUSLOW, David G., Qing WANG, John KALOGIROS a Ryan YAMAGUCHI. A Method for Identifying Kolmogorov's Inertial Subrange in the Velocity Variance Spectrum. *Journal of Atmospheric and Oceanic Technology* [online]. 2020, **37**(1), 85–102. ISSN 0739-0572, 1520-0426. available at: doi:10.1175/JTECH-D-19-0028.1

Appendices

Appendix I: Time-response plots

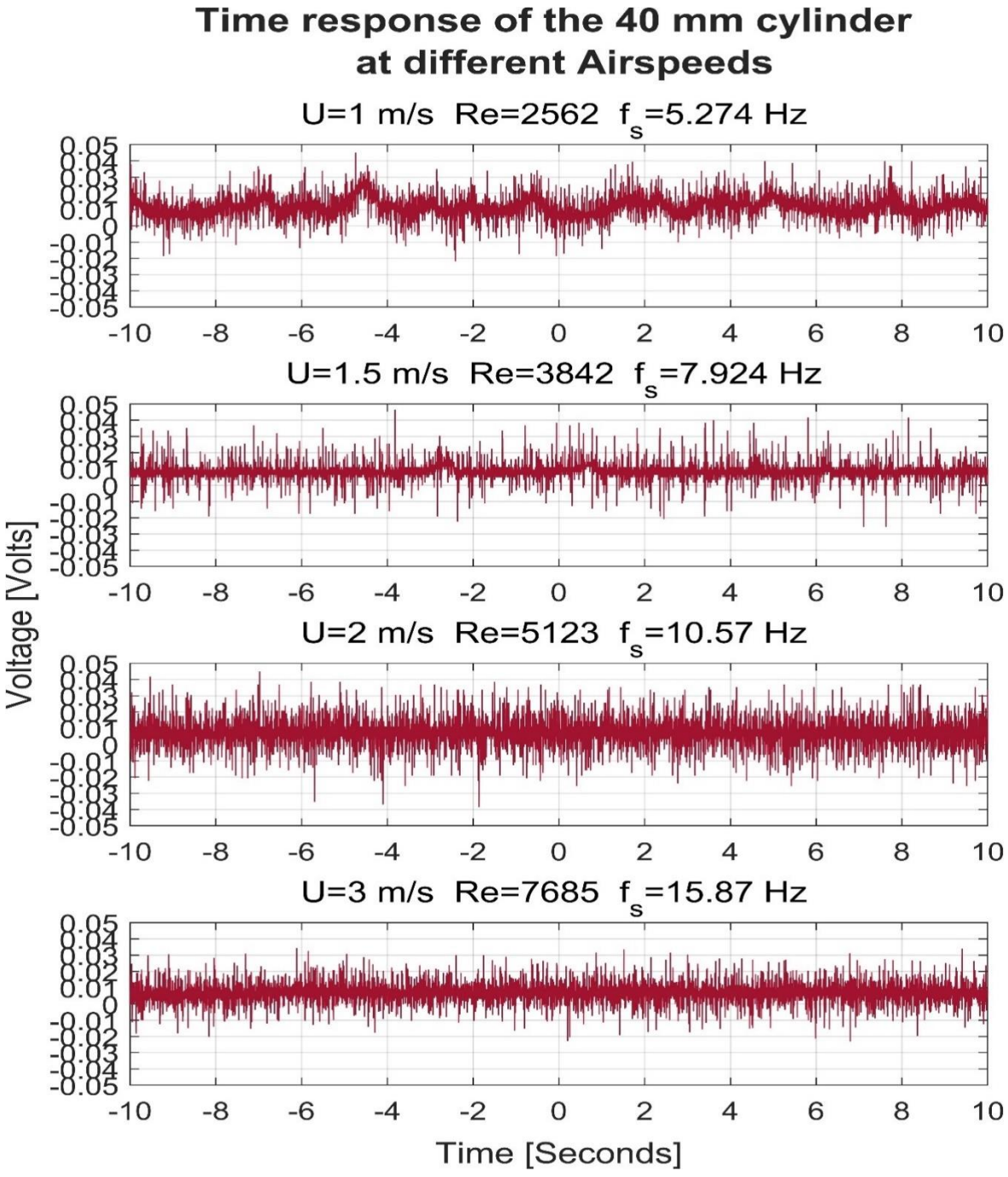

Figure (A – 1) Time-response by Cylinder (A), diameter 40 mm, at windspeeds of 1 – 3 m/s during vortex-induced vibrarions.

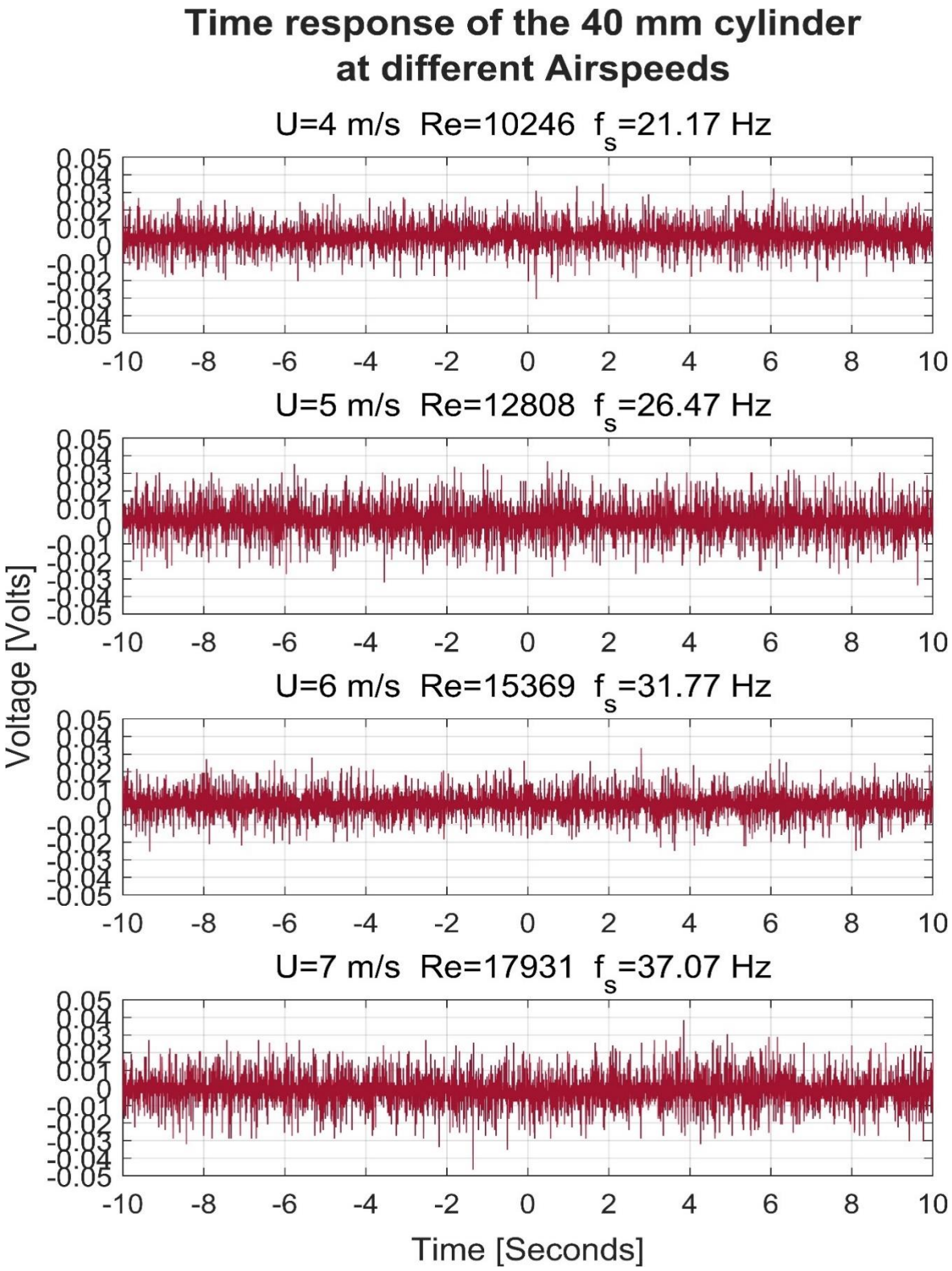

Figure (A – 2) Time-response by Cylinder (A), diameter 40 mm, at windspeeds of 4 – 7 m/s during vortex-induced vibrarions.

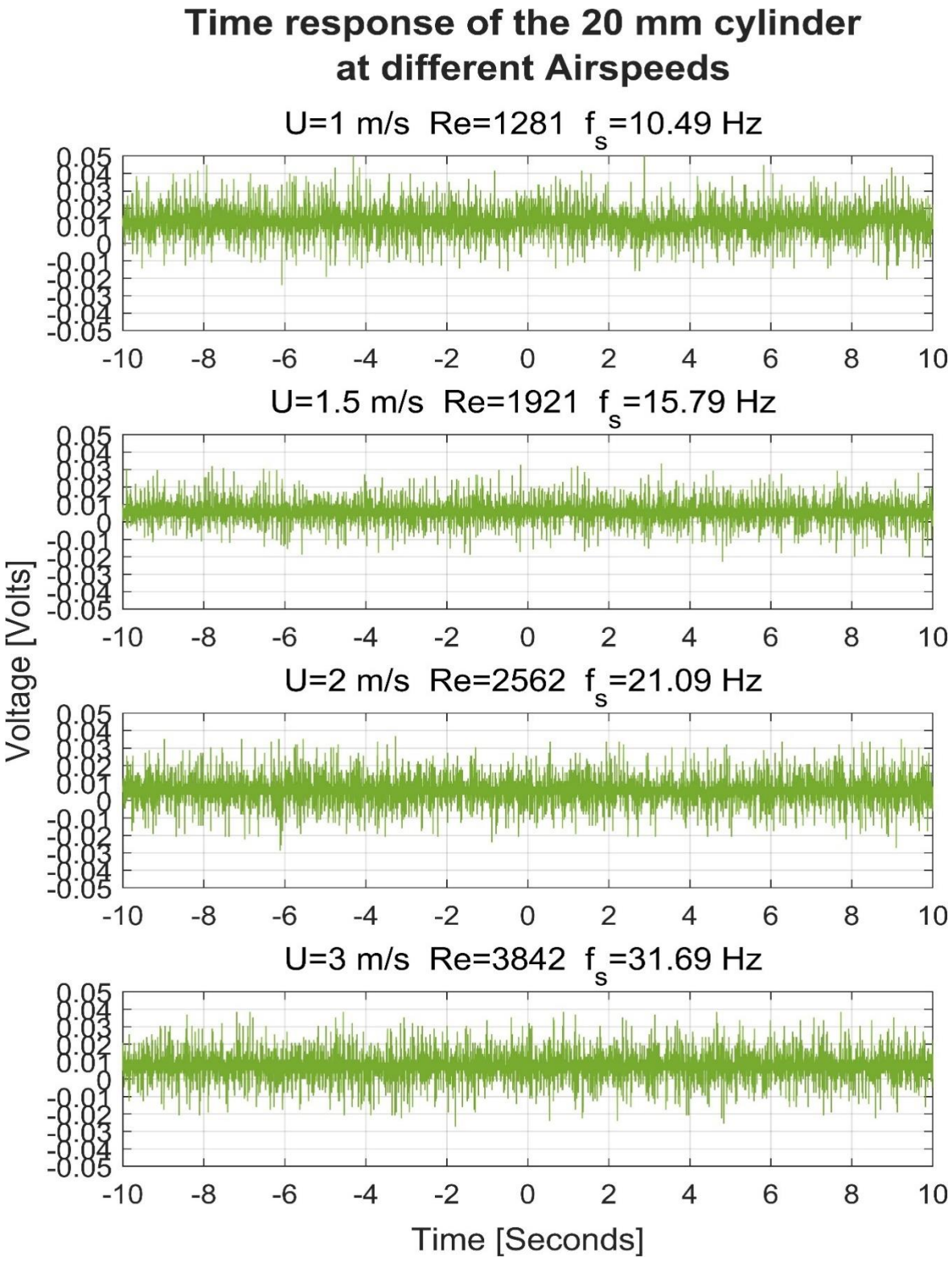

Figure (A – 3) Time-response by Cylinder (A), diameter 40 mm, at windspeeds of 1 – 3 m/s during vortex-induced vibrarions.

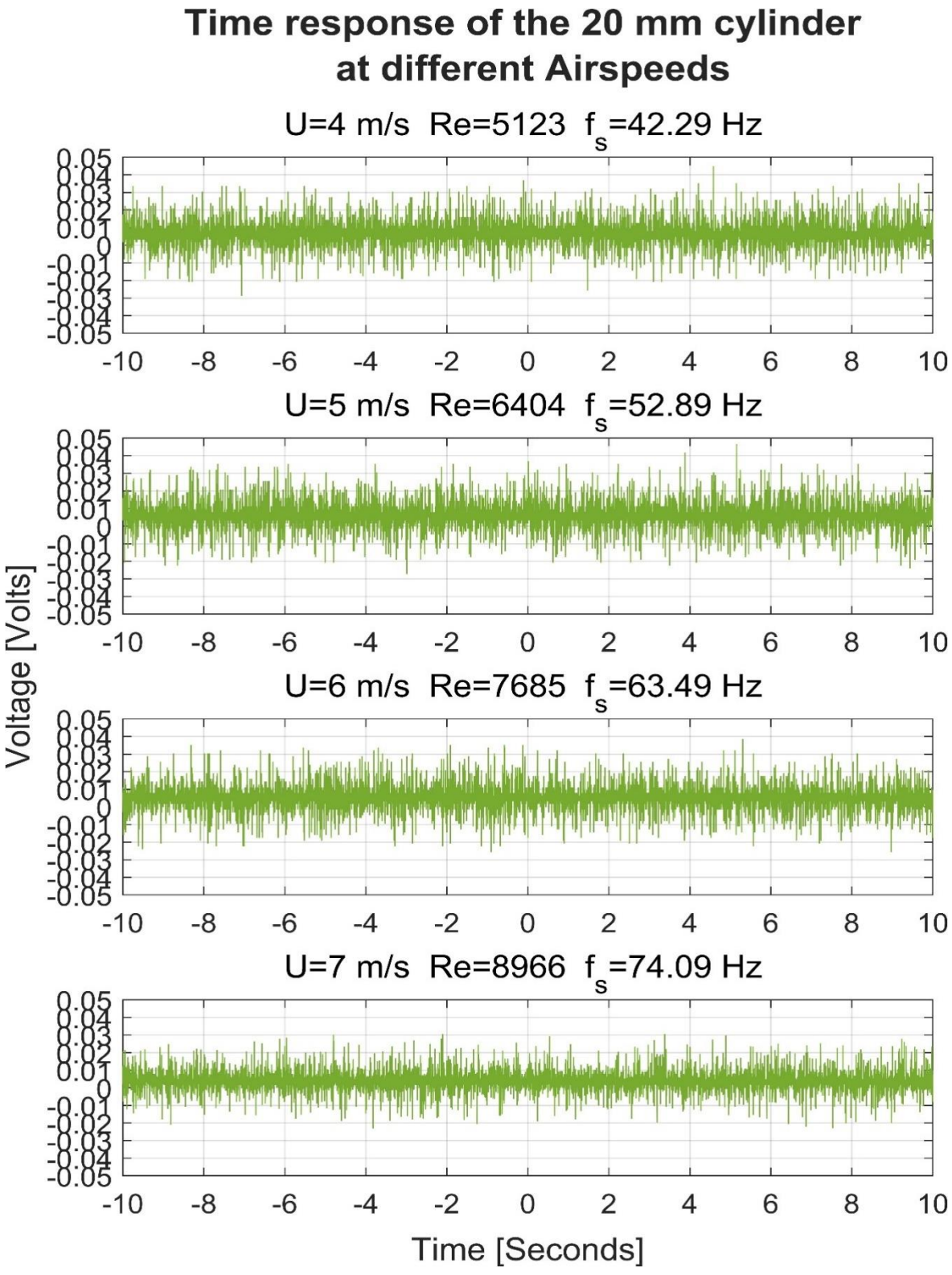

Figure (A – 4) Time-response by Cylinder (B), diameter 20 mm, at windspeeds of 4 – 7 m/s during vortex-induced vibrarions.

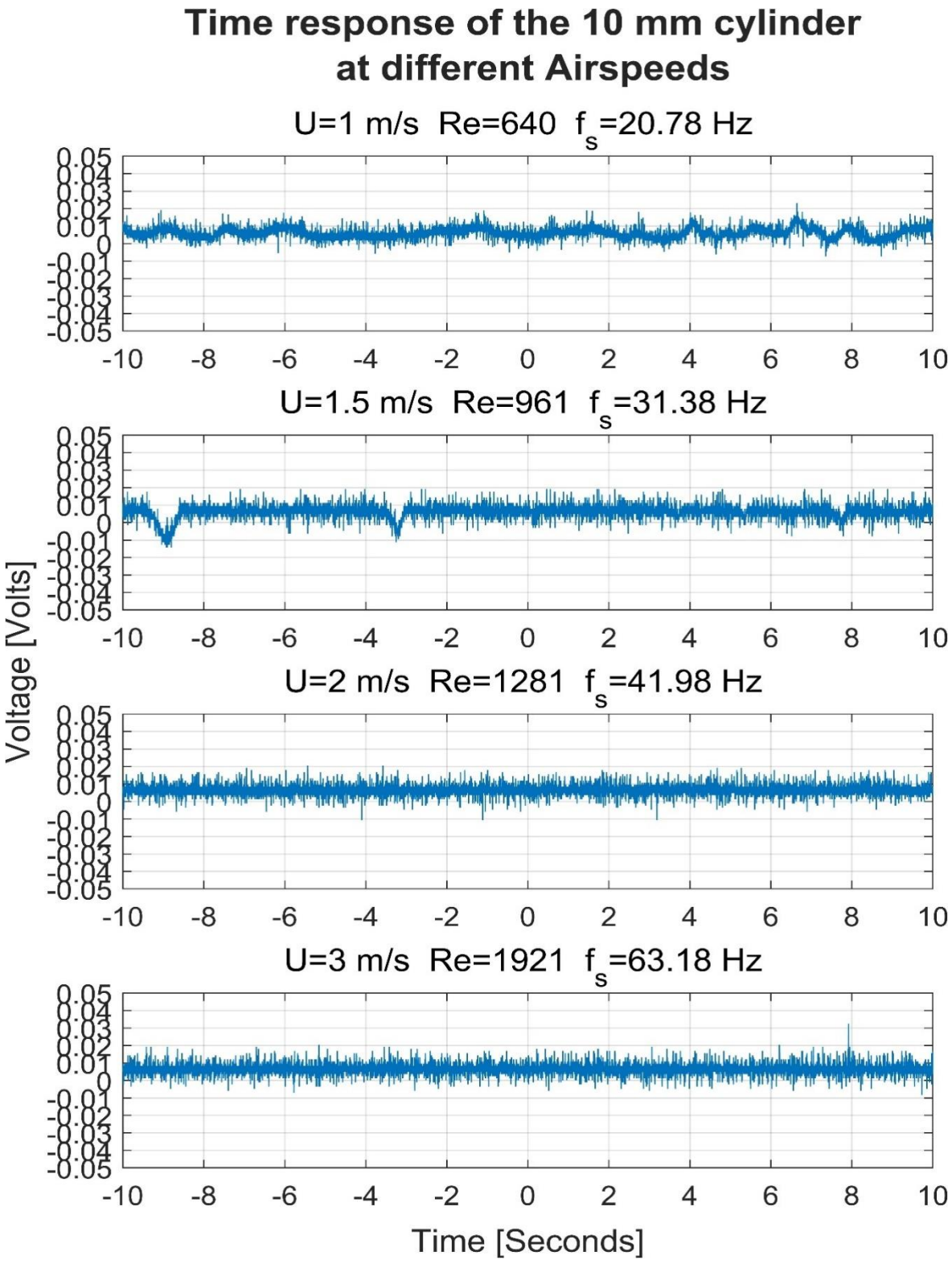

Figure (A – 5) Time-response by Cylinder (C), diameter 10 mm, at windspeeds of 1 – 3 m/s during vortex-induced vibrarions.

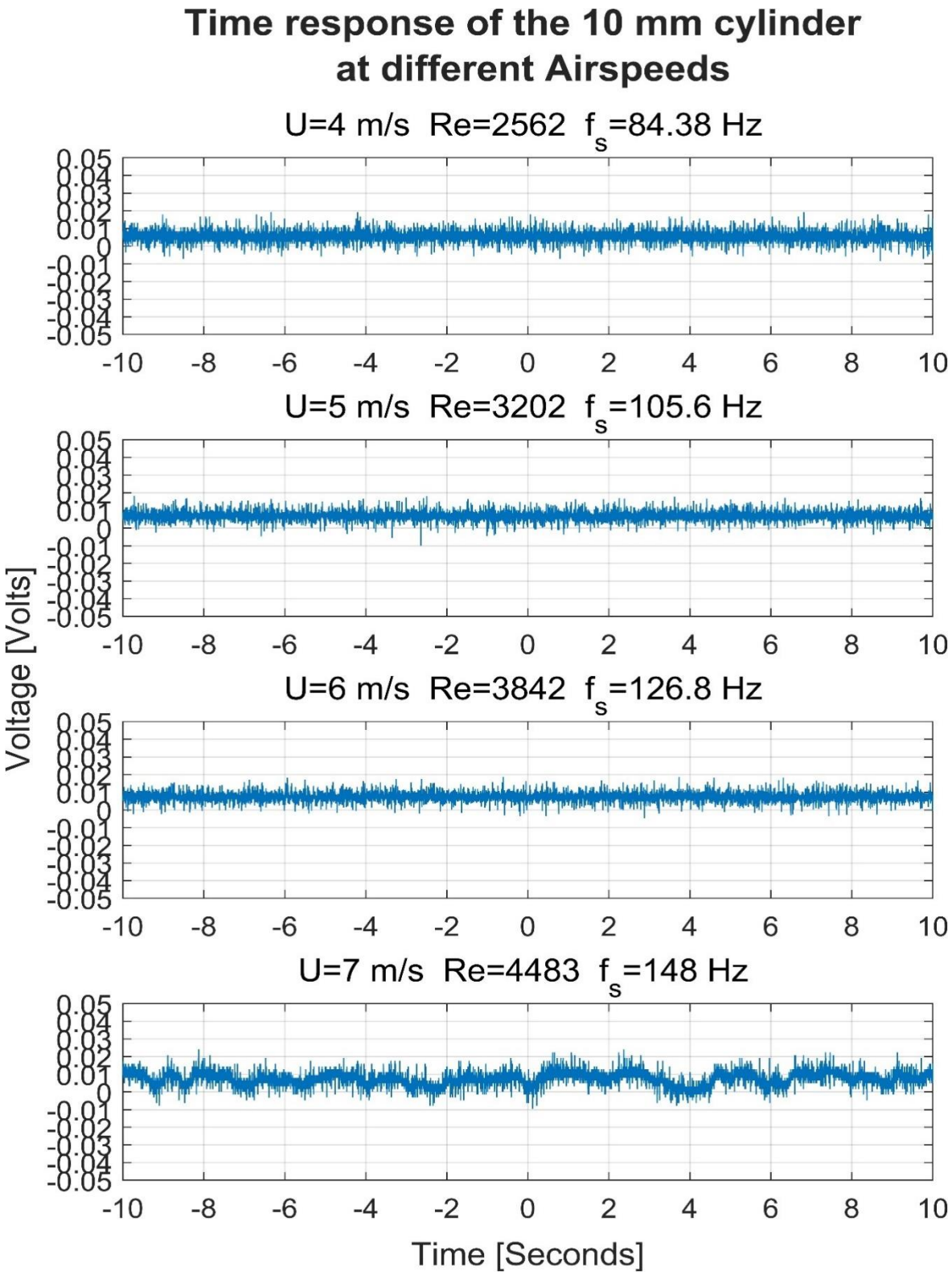

Figure (A – 6) Time-response by Cylinder (C), diameter 10 mm, at windspeeds of 4 – 7 m/s during vortex-induced vibrarions.

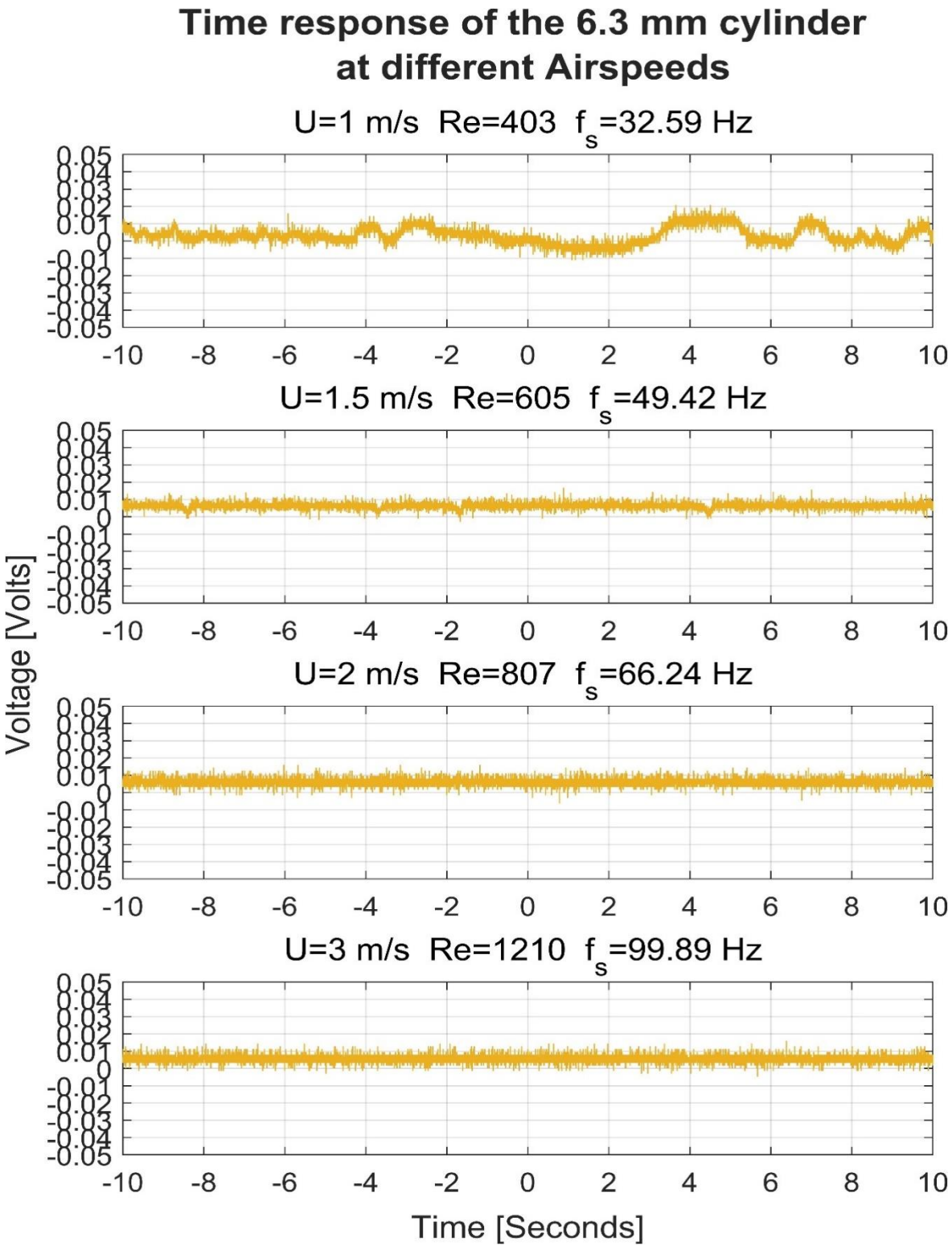

Figure (A – 7) Time-response by Cylinder (D), diameter 6.3 mm, at windspeeds of 1 – 3 m/s during vortex-induced vibrarions.

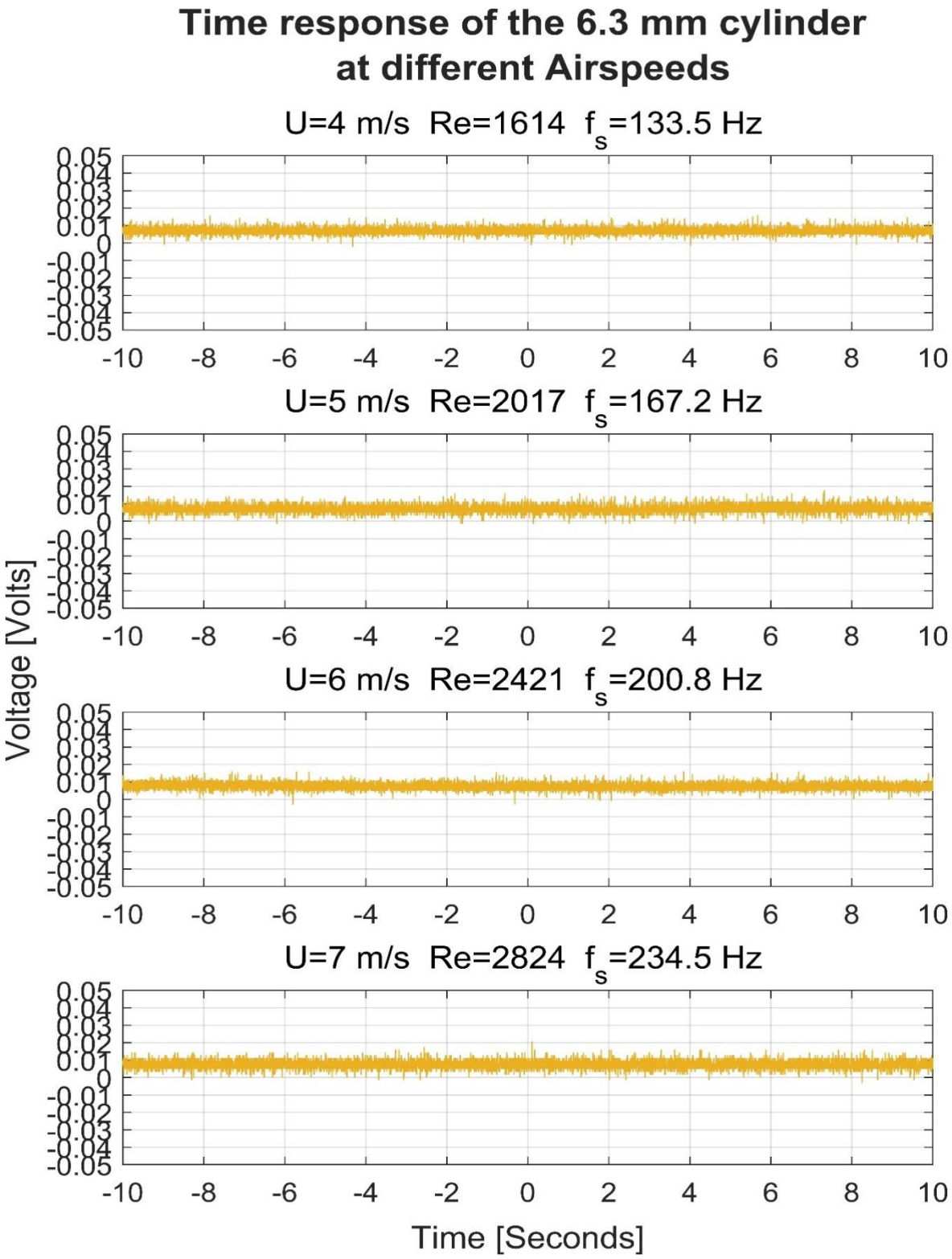

Figure (A – 8) Time-response by Cylinder (D), diameter 6.3 mm, at windspeeds of 4 – 7 m/s during vortex-induced vibrarions.

Appendix II: List of the Used Equations

$$d_{ij} = \left(\frac{\partial D_i}{\partial T_j}\right)_E = \left(\frac{\partial s_j}{\partial E_i}\right)_T \tag{1.1}$$

$$g_{ij} = -\left(\frac{\partial E_i}{\partial T_j}\right)_E = \left(\frac{\partial s_j}{\partial D_i}\right)_T \tag{1.2}$$

$$\kappa_{ij} = \sqrt{\frac{W_E}{W_M}} \tag{1.3}$$

$$\kappa_{ij} = g_{ij} d_{ij}\, E_p \tag{1.4}$$

$$\frac{K_{oc}}{K_{SC}} = \frac{1}{1-\kappa^2} \tag{1.5}$$

$$Q_m = 2\pi \frac{stored\ mechanical\ energy\ at\ resonance}{mechanical\ dissipated\ energy\ per\ resonant\ cycle} \tag{1.6}$$

$$\zeta = \frac{\varepsilon_{material}}{\varepsilon_{vaccum}} \tag{1.7}$$

$$s_j = S_{ij}\, T_j \tag{1.8}$$

$$[D] = [d]\{T\} + [\varepsilon^T]\{E\} \tag{1.9}$$

$$[s] = [S^E]\,\{T\} + [d^t]\,\{E\} \tag{1.10}$$

$$\begin{bmatrix} D_1 \\ D_2 \\ D_3 \\ s_1 \\ s_2 \\ s_3 \\ s_4 \\ s_5 \\ s_6 \end{bmatrix} = \begin{bmatrix} d_{11} & d_{12} & d_{13} & d_{14} & d_{15} & d_{16} & \varepsilon_{11}^T & \varepsilon_{12}^T & \varepsilon_{13}^T \\ d_{21} & d_{22} & d_{23} & d_{24} & d_{25} & d_{26} & \varepsilon_{21}^T & \varepsilon_{22}^T & \varepsilon_{23}^T \\ d_{31} & d_{32} & d_{33} & d_{34} & d_{36} & d_{36} & \varepsilon_{31}^T & \varepsilon_{32}^T & \varepsilon_{33}^T \\ S_{11}^E & S_{12}^E & S_{13}^E & S_{14}^E & S_{15}^E & S_{16}^E & d_{11} & d_{21} & d_{31} \\ S_{21}^E & S_{22}^E & S_{23}^E & S_{24}^E & S_{25}^E & S_{26}^E & d_{12} & d_{22} & d_{31} \\ S_{31}^E & S_{32}^E & S_{33}^E & S_{34}^E & S_{35}^E & S_{36}^E & d_{13} & d_{23} & d_{32} \\ S_{41}^E & S_{42}^E & S_{43}^E & S_{44}^E & S_{45}^E & S_{46}^E & d_{14} & d_{24} & d_{33} \\ S_{51}^E & S_{52}^E & S_{53}^E & S_{54}^E & S_{55}^E & S_{56}^E & d_{15} & d_{25} & d_{34} \\ S_{61}^E & S_{62}^E & S_{63}^E & S_{64}^E & S_{65}^E & S_{66}^E & d_{16} & d_{26} & d_{36} \end{bmatrix} \begin{bmatrix} T_1 \\ T_2 \\ T_3 \\ T_4 \\ T_5 \\ T_6 \\ E_1 \\ E_2 \\ E_3 \end{bmatrix} \quad (1.11)$$

$$Metric = \frac{P}{Vol \times \Pi^2} \quad (1.12)$$

$$I = \frac{\Pi^2}{Z_{acoustic}} \quad (1.13)$$

$$F_{r_t} = N_t/t \quad (2.1)$$

$$F_{r_p} = N_p/D_{cyl} \quad (2.2)$$

$$R = Z\ cos(\Phi) \quad (3.1)$$

$$X = Z\ sin(\Phi) \quad (3.2)$$

$$f^o = \frac{D_{cyl}}{\lambda} = \frac{D_{cyl}}{\frac{a}{f}} = \frac{D_{cyl}\ f}{a} \quad (4.1)$$

$$Z_t = R + (Z_L - Z_c)\ j \quad (4.2)$$

$$Z_L = 2\,\Pi\,f\,L \tag{4.3}$$

$$Z_c = \frac{1}{2\,\Pi\,f\,C} \tag{4.4}$$

$$P = \frac{V^2}{|Z_t|} = \frac{V^2}{\sqrt{R^2 + (Z_L - Z_c)^2}} \tag{4.5}$$

$$I = 10^{(L_i/10)} \times I_{ref} \quad [\frac{W}{m^2}] \tag{4.6}$$

$$P_{acoustic} = I \times \pi\, D_{cyl} L_{cyl} \tag{4.7}$$

$$\eta = \frac{P}{P_{acoustic}} \tag{4.8}$$

$$\rho = \frac{P}{A_{cyl}} = \frac{P}{\Pi D_{cyl} L_{cyl}} \tag{4.9}$$

$$\eta_v = \frac{V}{V + V_{loss}} \tag{4.10}$$

$$Re = \frac{U\,D_{cyl}}{\nu} \tag{5.1}$$

$$St = 0.212(1 - \frac{12.7}{Re}) \tag{5.2}$$

$$f_s = \frac{St\,U}{D_{cyl}} \tag{5.3}$$

$$Q_{mean} = CV_m \tag{5.4}$$

$$q = \frac{Q_m}{\pi\, D_{cyl} L_{cyl}} \tag{5.5}$$

$$E(k) = \alpha . \varepsilon_k^{\frac{-2}{3}} \times (k)^{\frac{-5}{3}} \tag{5.6}$$

$$V(f) = ß \times (f)^{\frac{-5}{3}} \tag{5.7}$$

$$P = \frac{V_{rms}^2}{R} \tag{5.8}$$

Appendix III: Codes

The code used for the calculation of the signals' FFT:

```
%Cylinder Data
cyl=["40" "20" "10" "06"];  %for reading the excel files
cyl_name=["40" "20" "10" "6.3"];  %For writing diameter in titles
D = [0.04;0.02;0.01;0.0063];

%Defining Velocities
X=["01" "15" "02" "03" "04" "05" "06" "07"];
U=[1,1.5,2,3,4,5,6,7];
usd=[1:8];    %Indices of velocities that we want to plot.

%Flow Characteristics
Re = 1.17/(1.827e-5)*D*U;
St = 0.212*(1-12.7./Re);    %Roshko's model for Re above 300

%Reading open circuit voltage
G_t_x=zeros(65536,4*numel(X));
G_t_y=zeros(65536,4*numel(X));
my_G_f_x=zeros(65536,4*numel(X));
my_G_f_y=zeros(65536,4*numel(X));
for i=1:numel(cyl)  % 4 cylinders
    for j=1:numel(X)  % velocities
       NAME=append(cyl(i),"_",X(j),"_0.csv");
        G=readmatrix(NAME);
       dt(i,j) = G(4,1)-G(3,1);         Fs(i,j)=1./dt(i,j);

       [row, col] = find(isnan(G));
       end_t(i,j)=row(3)-1;% location of last row of time data.
       lngth_T(i,j)=end_t(i,j)-2; %number of time data points by
        excluding the two elements at the begining
       v_mean(i,j)=mean(G_t_y(1:lngth_T(i,j),(i-1)*12+j));

       %Performing pure FFT without windowing at each velocity
       my_G_f_x(1:floor(lngth_T(i,j)/2),(i-1)*12+j) =
       (Fs(i,j)*(0:(floor(lngth_T(i,j)/2)-1))/lngth_T(i,j))';

       FFT(1:lngth_T(i,j),(i-1)*12+j) =
       fft(G_t_y(1:lngth_T(i,j),(i-1)*12+j)-v_mean(i,j),lngth_T(i,j));

       %Calculating scaled amplitude of the FFT
       AMP(1:lngth_T(i,j),(i-1)*12+j) =
       abs(FFT(1:lngth_T(i,j),(i-1)*12+j))/lngth_T(i,j);

        %converting from double sided fft to one sided.
        my_G_f_y(1,(i-1)*12+j) = AMP(1,(i-1)*12+j);
        my_G_f_y(2:floor(lngth_T(i,j)/2),(i-1)*12+j) =
       2*AMP(2:floor(lngth_T(i,j)/2),(i-1)*12+j);
    end
end
```

Author's Publications

[1] SALEM, Shehab a Karel FRAŇA. A Wind Tunnel Study of the Flow-Induced Vibrations of a Cylindrical Piezoelectric Transducer. *Sensors* [online]. 2022, **22**(9), 3463. ISSN 1424-8220. Available at: doi:10.3390/s22093463
(Q1, IF = 3.847)

[2] SALEM, Shehab, Karel FRAŇA a Iva NOVÁ. The Potential of Cylindrical Piezoelectric Transducers for High-Frequency Acoustic Energy Harvesting. *Energies* [online]. 2021, **14**(18), 5845. ISSN 1996-1073. Available at: doi:10.3390/en14185845
(Q3, IF = 3.54)

[3] SALEM, Shehab, Karel FRANA a Sylvio SIMON. Experimental and Numerical Study of the Aero-Acoustics of Flow over Structured Sheet Metals. In: *2021 25th International Conference on Circuits, Systems, Communications and Computers (CSCC)* [online]. Crete Island, Greece: IEEE, 2021, s. 26–36 [vid. 2022-01-31]. ISBN 978-1-66542-749-4. Available at: doi:10.1109/CSCC53858.2021.00013

[4] SALEM, Shehab, Karel FRANA, Iva NOVA a Jiri ERHART. Acoustic Energy Harvesting Using Piezo-Electric Materials. In: *2020 International Youth Conference on Radio Electronics, Electrical and Power Engineering (REEPE)* [online]. Moscow, Russia: IEEE, 2020, s. 1–6 [vid. 2022-01-07]. ISBN 978-1-72815-655-2. Available at: doi:10.1109/REEPE49198.2020.9059190

[5] SALEM, Shehab, Karel FRAŇA a Iva NOVÁ. Design of Acoustic Energy Harvesting Unit Using Piezo-Electric Diaphragm. *Materials Science Forum* [online]. 2020, **986**, 109–115. ISSN 1662-9752. Available at: doi:10.4028/www.scientific.net/MSF.986.109
(Q4, IF = 0.48)